

Searching Beyond the Standard Model: Bridging the Gap Between Theory and Data

by

Dylan Linthorne

A thesis submitted to the
Faculty of Graduate and Postdoctoral Affairs
in partial fulfillment of the requirements
for the degree of

Doctor of Philosophy in Physics

Department of Physics
Carleton University
Ottawa-Carleton Institute of Physics
Ottawa, Canada
January 18, 2022

Copyright © 2022 Dylan Linthorne

Abstract

The current standard model (SM) of particle physics is known to be an incomplete model of the Universe. Experiments have given strong evidence for the existence of dark matter. Other alterations to the SM could include the presence of extra forces and/or non-standard cosmologies. In our current era, we have many experimental methods that can probe the boundaries of the SM using particle colliders, astrophysical observatories, or gravitational wave interferometers. In the latter case, we explore the possibility of detecting gravitational waves generated by first-order phase transitions in multiple hidden sectors. These hidden sectors are completely decoupled from the SM, hosting exotic particles with unique forces. Each thermally decoupled sector evolves and undergoes phase transitions at completely different times. We take N naturalness as a sample model that features multiple additional sectors, many of which undergo phase transitions that produce gravitational waves. We examine the cosmological history of this framework and then calculate novel gravitational wave signatures characteristic to only models with multiple decoupled sectors. These unique profiles, when compared to the sensitivity of future gravitational wave interferometers, could be a smoking gun for non-standard cosmologies. In the case where one of these hidden sectors instead contains a dark matter candidate which couples weakly with the SM, we propose novel searching methods to be employed at particle colliders. These confining hidden sectors at the GeV scale can lead to novel collider signatures including those termed emerging jets with large numbers of displaced vertices. The triggers at the LHC experiments were not designed with this type of new physics in mind, and triggering can be challenging. We show that the efficiency and the total event rate at current triggers can be significantly improved by considering additional sources of radiation. We also explore possible new triggers that employ hit counts

in different tracker layers as input into a machine learning algorithm. We show that these new triggers can have reasonably low background rates and sensitive to a wide range of new physics parameters even when trained on a single model.

Acknowledgments

First, I'd like to thank my supervisor Daniel Stolarski. I came to Carleton adamant on only pursuing a masters. Instead, I was given the rare opportunity of working with both a mentor and someone who viewed me as an equal collaborator. I stayed for a PhD because of Daniel and I'm extremely grateful for it. Daniel gives his students just the right amount of autonomy, challenges, and guidance to fail fast and succeed even faster. I always felt like I was a colleague first and student second. I wouldn't have gained the skills I have today if it weren't for the patience and trust he has for his students. I know that whenever our paths cross that I can look forward to sharing new ideas over a pint, or two.

I am grateful for the entire Carleton Physics department, which hosted a creative and collaborative environment for both students and faculty. Most notably; Paul Smith, an office mate, coauthor, and overall fantastic soul to be around; Tae Hyoun Park (Matt), who has been my partner in crime during my early years and still challenges me to this day; Rouzbeh Yazdi, a wise academic, brilliant philosopher, and most importantly a cherished friend. Last but not least, I'd like to thank Jerome Claude, Benjamin Davis-Purcell, and Nathan Murtha. They are like family to me. Learning, growing, and drinking with them has been one of the highlights of my academic journey.

I would like to thank my boxing coach Chris Essiambre and the N1 Boxing crew. Chris and the team have taken something already special to me and lifted it to new heights. Throughout the last four years the team has created the perfect counterpoint to my PhD work. Academia can sometimes be riddled with hidden biases, elitism, and egos. Chris and the team instead provided a unique and supportive community, with people stemming from all backgrounds. Here, egos are unable to flourish as the

ring keeps us humble. They will always be my brothers, in and out of the ring, and I am very grateful that they've left me with enough braincells to finish this thesis.

I would like to thank my partner, Brittany Scowen. Not only has she supported me through some of my darkest and uncertain times, but she would have killed me if I didn't include her here. She has been a beacon of light in, what seemed like, a very long and dark tunnel throughout the pandemic. Now that we're getting closer to its end, we're excited in knowing we have the entire world to explore together.

I am forever thankful for my biggest role model, my mother Charmaine Linthorne. A single mother who single-handedly raised her two kids in spite of socio-economic barriers, and didn't take any shit from anyone. She worked day and night in a broken system so my brother and I could continue to stay blind to it— all the while coming home with a smile. My mother's lessons were never about working hard until you break, but instead she showed us that our surroundings, hurdles, and lifestyle shouldn't dictate who we are. As a first generation academic, I never grew up with expectations, only the question of whether I was happy. This is a special type of privilege that can't be generated by wealth, education, or glory, but only through love.

My successes are not my own but shared with my younger brother, and best friend, Olivier Leduc. My brother and I were inseparable in our early years, and raised each other in trying times. I remind myself everyday that this PhD thesis means absolutely nothing. It's an archaic process of pomp and vanity which will rot in the Carleton archives. What is important is the journey, discoveries, and people I've met along the way—my brother exemplifies this. He doesn't meet people with judgement or assumptions, instead he takes the opportunity to find a shared common ground where learning and laughter can foster—something I idolize to this day. Carl

Sagan taught us how insignificant we are when compared to the sheer beauty and awe of the world. When I see my brother, it's the opposite. The world slowly seeps away with every word we share.

Statement of Originality

The background chapters 1, 2, & 3 are reviews of the Standard Model, cosmology, and relevant analysis methods, respectively. Majority of the material for these chapters is well established and is covered in various textbooks. In the first chapter the main sources being: Peskin and Schroeder’s “An Introduction to Quantum Field Theory” [1] and Matthew Schwartz’s “Quantum Field Theory and the Standard Model” [2]. In Chapter 2 the main sources are: Kolb and Turner’s “The Early Universe” [3] and James Hartle’s “Gravity” [4]. In Chapter 3 the main sources are: Maxim Perelstein’s TASI lectures “Introduction to Collider Physics” [5], John Campbell et al’s “The Black Book of Quantum Chromodynamics: A Primer for the LHC Era” [6], and Glen Cowan’s “Statistical Data Analysis” [7]. The following chapters 4 & 6 and appendix B contain original research. Each of these projects were done in collaboration with other physicists with contributions as follows:

Ch. 4 Gravitational Wave Signals from Multiple Hidden Sectors [8]: This project was done in collaboration with Paul Archer-Smith and Daniel Stolarski. D.L proposed the idea of using multiple hidden sectors as a generator of unique gravitational wave signals. Both P.A.S and D.L found the appropriate toy model of N naturalness and reheating schemes. The particle physics calculations were carried out by P.A.S including hidden sector particle spectra, Neff constraints, reheating scenarios, and energy density calculations. D.L calculated the thermal dynamic variables of the phase transitions, gravitational wave (MHD, Sound, and Scalar field) contributions at production and today, (non)runaway regimes, power law sensitivities curves for each proposed interferometer, and resulting plots. All work was closely checked and discussed by all collaborators.

Ch. 5 **Triggering on Emerging Jets** [10]: This work was done in collaboration with D.S using one of his original models. The work was proposed and supervised by D.S. The bulk of the work was conducted by D.L with constant checks and discussion with D.S.

Ap. B **Searching for long-lived particles beyond the Standard Model at the Large Hadron Collider** [9]: This work was done with one of the white paper’s sub-collaborations, focused on the topic of dark showers. The collaboration highlighted the current theoretical landscape containing dark showers and limitations of Monte-Carlo modelling. D.L and D.S both contributed a review of emerging jets and semi-visible jets. D.L assisted in showing the quantifiable constraints of current Monte Carlo methods using visual distributions of extreme case scenarios. It has been placed in Appendix b for the purpose of generically defining two different dark showering implementations; simivisible jets and emerging jets. Chapters 1 and 5 build off of the generic emerging jets model for different hidden valley mediators, hidden sector spectra, and quantum numbers.

Contents

1	The Standard Model and Beyond	1
1.1	Introduction	1
1.2	The Standard Model	2
1.2.1	Quantum Field Theory	2
1.2.2	Field Content of the Standard Model	5
1.2.3	Higgs Mechanism	8
1.2.3.1	The Hierarchy Problem	13
1.2.4	Quantum Chromodynamics	15
1.3	Dark Matter and Hidden Sectors	17
1.3.1	Observations	17
1.3.2	The Hidden Valley	18
1.3.3	Dark QCD	19
1.3.4	Asymmetric Dark Matter	21
2	Cosmology	22
2.1	The Standard Cosmology	22
2.1.1	FLRW Universe & Thermal Histories	22
2.1.1.1	Neutrino decoupling	29
2.1.1.2	Recombination	30

2.1.2	Phase Transitions	30
2.2	Non-Standard Cosmologies	34
2.2.1	Exotic Phase Transitions	34
2.2.2	N-Naturalness	36
2.3	Gravitational Waves	41
2.3.1	Linearized Einstein Equation	41
2.3.2	Stochastic Gravitational Waves	45
3	Data, Simulations, and Reconstructions	48
3.1	Collider Physics	48
3.2	Monte Carlo Showering Simulations	53
3.2.1	Sudakov Probability and Parton splitting	53
3.2.2	Hadronization and Tuning	55
3.2.3	Dark Showering Uncertainties	57
3.3	Jet Reconstructions	58
3.4	Statistical Tests & Machine Learning	61
3.4.1	Neural Networks	66
4	Gravitational Waves from Multiple Hidden Sectors	70
4.1	Introduction	70
4.2	Particle Setup	72
4.3	QCD Phase Transition	74
4.3.1	Standard Sectors	77
4.3.2	Exotic Sectors	78
4.4	Reheating N Sectors	79
4.5	Constraints	82

4.5.1	Exotic Sector Contributions	84
4.5.2	Standard Sector Contributions	85
4.5.3	Generalized Reheating Scenarios	86
4.6	Gravitational Wave Signals	87
4.6.1	Production of Gravitational Waves	90
4.6.2	Detection of Stochastic Gravitational Waves	98
4.7	Conclusion	101
5	Triggering on Emerging Jets	103
5.1	Introduction	103
5.2	Models for emerging jets	108
5.3	Event generation	113
5.4	Current triggers	116
5.4.1	Description of triggers	117
5.4.2	Results with current triggers	122
5.5	Machine learning triggers	126
5.6	Summary and conclusions	138
6	Conclusion	140
A	Runaway Phase Transitions	142
B	Dark Showering Models	146
B.1	Semi-visible Jets	148
B.2	Emerging Jets	148

List of Tables

1.1	Field content of the Standard Model. a runs from 1 to 3, and b from 1 to 8. The L and R next to a spin 1/2 field represents its chirality. f is the generational index which runs from 1 to 3.	8
1.2	Field content of the hidden valley charged under dark QCD. The fundamental representation of dark qcd is that of the dark quark Q_d . Vector Z_d and bifundamental X_d mediators are taken as example portals between the two sectors.	19
4.1	Outline of parameters used for the various multi-hidden sector scenarios. The higgs vev is the vev for the given additional sector, Λ_{QCD}^{AS} is the QCD phase transition in the additional sector, and T_γ is the temperature of the SM photon bath when the SFOPT occurs in the additional sector. The index indicates the equivalent sector from the N naturalness model (Eq. (4.4)). It should be noted that although the various sectors undergo phase transitions at different temperatures, they are all assumed to be reheated to the same initial temperature. .	96

5.1 Dark sector parameters for our benchmark models. Λ_d is the dark confinement scale, m_V is the mass of the dark vector mesons, and m_{π_d} is the pseudo-scalar mass. $c\tau_{\pi_d}$ is the rest frame decay length of the pseudo-scalars. We take $N_c = 3$ and $n_f = 7$ in both benchmarks. Models **A** and **B** are considered in Section 5.4, while Models **A**, **C**, **D**, **E** and **F** are considered in Section 5.5. 113

5.2 The 2017 ATLAS triggers [202] used in Section 5.4 analysis. Triggers are separated by lower level (L1) thresholds, Higher level (HLT) thresholds and offline selection criteria. Reconstructed jets used in the Single Jet, MET and H_T trigger have $R = 0.4$. Thresholds with (*) must additionally satisfy the isolation cone criteria in Eq. (5.8). A lower level threshold isn't given for the H_T as we seed it from the lower level Single Jet trigger instead. 117

5.3 ATLAS inner tracker specifications taken from [210, 211]. The barrel layers of each tracker section are shown with their radial distance from the beam pipe/interaction point. Since the TRT is a more complex tracking package, we only consider the hits on the initial layer of the TRT. Endcaps also accompany most of the trackers but aren't considered in this analysis. 130

5.4 Signal efficiencies for expected allowable background rates for new ATLAS triggers for $M_{Z'} = 500$ GeV. The lifetimes represent Models **A**, **C**, **D**, and **E**. Each value in the last two columns are extracted from Fig. 5.8 for a bkg efficiency calculated using Eq. (5.11) assuming the events are fully saturated by background. 136

List of Figures

1.1	One-loop quantum corrections on the mass of a scalar field from scalar, gauge, and fermion fields [19].	13
1.2	A diagram from [29] illustrating a hidden valley charged under dark QCD around the GeV scale. The communicating portal is a TeV scale mediator X_d , charged under both groups. The dark sector will contain a spectrum of hadrons analogous to QCD, where the non-stable mesons decay back into the SM through X	20
2.1	The cosmological timeline, ca. 2018 [31]. The timeline shows the various epochs in the standard cosmology, including; quantum gravity (QG), inflation, Peccei Quinn (PQ) phase transition, leptogenesis, dark matter (DM) freezeout, electroweak phase transition (EWPT), baryogenesis, quantum chromodynamic phase transition (QCD PT), and big bang nucleosynthesis (BBN).	23
2.2	The thermal history of effective relativistic degrees of freedom g_* as a function of temperature. Also included are effective degrees of freedom for number density g_n , pressure g_p , and entropy g_s taken from [33]. . .	27

2.3	A illustration of the Columbia plot [38] from [39], which encompasses the phase diagram of $N_f = 3$ QCD. The mass of the up-type and down-type quarks are assumed to be approximately degenerate. The SM exists in the weak cross-over regime. Two regimes of SFOPT exist corresponding to the restoration of chiral symmetry (bottom left) and pure Yang-Mills symmetries (top right).	35
2.4	A visual representation of the many sectors of N -naturalness.	37
2.5	The various decay channels of the reheaton with the EW sector particles. The left (right) column is for $v \neq 0$ ($v = 0$). The top (bottom) row is for m_ϕ greater (lighter) than the m_H	39
2.6	The ratio of energy densities deposited in the i^{th} sector as a function of sector number and the energy density in our sector from [41]. The scalar reheaton is taken to have mass of $m_\phi = 100$ GeV. Dotted lines represent the expected scaling of the sectors. The solid lines our numerical results using Eq. (2.23).	41
3.1	The boost invariant quantities η and ϕ mapped onto the ATLAS experiments coordinate system. The pseudorapidity η is a function of the polar angle θ . The ATLAS detector comprises of a cylindrical geometry to take advantage of this coordinate frame [44].	52
3.2	An educational sketch of the receiver operating characteristic (ROC) curve. The true positive rate (α) is plotted against the false positive rate (β). The dotted red line shows the completely random classifier, which has 0.5 discriminating power. The perfect classifier is shown in purple where, for a certain boundary value, the true positive rate is 100% and the false positive rate is 0%. [59]	64

3.3	A schematic of a general NN architecture. The NN is organized in input layer, hidden layers, and output layer. The weights of each layer are represented by each connection. All connections are shown but can be removed by setting its corresponding weight to zero.	67
4.1	Gravitational wave spectral energy density (solid curves) for standard N naturalness using the scalar reheaton model of section 4.4. The curve corresponding to the sum of the sectors is approximately equal to the $i = 1$ curve. All contributions are assumed to be purely from bubble collisions Ω_ϕ . The colored solid lines use $\beta/H = 10$ where as the dashed gray line is the total contribution of all sectors for $\beta/H = 10^4$ (the sum of all sectors is roughly equal to the $i = 1$ curve and sectors beyond the first are below the range of this plot). The shaded dashed curves are the power law noise curves [129] calculated from expected sensitivity as described in Section 4.6.2. The ones on the right are space-based interferometers: Lisa [72] (blue), DECIGO [75] (light blue), BBO [69] (red). The ones on the left are for the pulsar timing array SKA [71] for exposure time of 5-years (purple), 10-years (orange), and 20-years (green).	94
4.2	Gravitational wave spectral energy density for the various scenarios found in Tab. (4.1). All contributions are assumed to be purely from runaway bubble collisions Ω_ϕ . The colored solid lines use $\beta/H = 10$ where as the dashed gray line is the total contribution of all sectors for $\beta/H = 10^4$. The inset is a closer look at the region around the peaks for the $\beta/H = 10$ case. The shaded curves are the same as Fig. 4.1.	99

5.1 Cross section of $pp \rightarrow Z' \rightarrow Q\bar{Q}$ for a leptophobic Z' as a function of its mass $M_{Z'}$. Generated by convolving the partonic cross sections of u, d -quarks with their respective parton distribution functions at a centre of mass energy of $\sqrt{s} = 13$ TeV. η is a function of the Z' Lagrangian parameters defined in Eq. (5.6). 112

5.2 Higher order QCD initial state radiation diagrams of $q\bar{q}$ induced Z' resonant production. Gluons are radiated from the quark lines in the form of detectable hard QCD jets. EW splittings are also possible with diagrams scaling with the EW couplings. 113

5.3 The Mercedes topology of three jets recoiling off of each other within the p_T plane. In this case, two emerging jets carrying missing transverse energy recoil off of a visible hard QCD jet. This configuration produces more missing transverse energy as the jet momentums are balanced in opposite directions. 118

5.4 ATLAS trigger efficiencies, at truth level, for various processes outlined in Section 5.3. The first (second) row corresponds to Model **A** (**B**) from Table 5.1. In the first column, we have the MET triggers; in the second column, the H_T triggers; and, in the third column, the lepton and photon triggers. Both the electron and muon trigger efficiencies considered W/Z ISR while the photon trigger considered photon ISR only. All processes were generated under LHC conditions of a centre of mass energy of 13 TeV. The trigger thresholds were taken from the ATLAS trigger menu summarized in Table 5.2. 119

5.5 ATLAS trigger efficiencies as a function of the dark pion lifetime $c\tau$.
The LO process is shown in the solid lines, the LO + j process is shown
in the dashed lines. An inverse relationship is exhibited between MET
and H_T efficiencies. 123

5.6 Cross section times efficiency of various processes (leading order, 1-jet
ISR, 2-jet ISR, electro weak ISR) scaled by their respective leading
order process. The left plot uses the MET trigger and Model **A**, while
the right uses H_T and Model **B**. The dotted line is the leading order
process, which when normalized to itself, is just unit as a reference for
the rate boost obtained from additional processes. On the right plot,
the blue region on the left has zero events that we simulated pass the
trigger, $\epsilon \lesssim \epsilon_{\min} = 1/400\ 000$ 124

5.7 The fraction of dark pions that decay into visible sector particles within
the primary ATLAS detectors. The green line represents the decay
fraction within the electromagnetic calorimeter, the orange for the
hadronic calorimeter, and the blue for the inner trackers. The blue line
is the fiducial boundary of the muon spectrometer which we take to be
the boundary of the ATLAS detector. We do not show that fraction
that decay before the first tracker layer, and this fraction is significant
at short lifetime. These fractions are computed from simulation with
 $M_{Z'} = 500$ GeV. 129

5.8 On the left, Model E (blue) discrimination from $b\bar{b}$ background (green) using a support vector machine. The SVM was trained using four layers IBL, Pixel₂, SCT₂, TRT₁. An average pileup of $\mu = 50$ was added to both signal and background. The flat bars (points) correspond to the training (test) set. On the right, Receiver Operation Characteristic ROC for Models **A**, **C,D**, and **E** using the TMVA support vector machine. The SVM was trained and tested using four layers: IBL, Pixel₂, SCT₂, TRT₁, with the input variable defined in Eq. (5.10). At a given background efficiency the expected signal efficiencies increase as the dark pion lifetimes lower. The required background rejection is estimated to lie between the horizontal dotted lines. 134

5.9 Area Under the Curve (AUC) of the ROC curves. The SVM was trained on specific models (vertical axis) and tested/applied on a unknown data set (horizontal axis) of the same/alternative model. The diagonals are the AUC values corresponding for training and testing on the same models i.e. the ROC curves of Fig. 5.8. Trained models show little separation in classification power when applied to a range of lifetimes and hidden sector parameters. 137

A.1 Gravitational wave spectral energy density for the various scenarios found in Tab. (4.1). All contributions are assumed to be from a non-runaway phase transition with terminal velocity $v = 0.95$. The coloured solid lines use $\beta/H = 10$ where as the dashed grey line is the total contribution of all sectors for $\beta/H = 10^4$. The top left figure shows the individual sound wave and MHD contributions. The shaded curves are the same as Fig. 4.1. In contrast to the runaway case, most scenarios evade the projected sensitivities. 143

Chapter 1

The Standard Model and Beyond

“Standards are always out of date. That’s what makes them standards.”

— Alan Bennett

1.1 Introduction

The Standard Model of particle physics, unlike its modest name, is one of the most celebrated achievements in the field of particle physics and cosmology. It unites the strong, weak, and electromagnetic forces under a single complete theory, incorporating all of the known visible particles in the Universe. A full quantum theory of the Standard Model was first formalized in the second half of the 20th century [11–14]. It predicted the existence of the W , Z , bosons and top quark before they were ever measured in the lab.

Even when knowing the numerous triumphs of the Standard Model, theorists have become frustrated over the past few decades. The reason being that the theory is *too* good. In the past half a century we have inferred that the Standard Model is incomplete. Extensions beyond the Standard Model include, but not limited to, dark

matter, dark energy, and quantum gravity. In an attempt to solve these discrepancies, the theoretical landscape has blossomed, incorporating novel ideas that endow the Standard Model with new particles, unique sectors, and/or novel forces. The following sections will introduce the Standard Model and its framework—quantum field theory. The last few sections will discuss some of the frameworks that extend the Standard Model.

1.2 The Standard Model

1.2.1 Quantum Field Theory

Quantum Field theory (QFT) is the framework in which the dynamics of particle physics is built on. The field theoretic formulation of quantum mechanics focuses on quantum fields instead of particles. Each known particle in nature becomes an excitation of this all pervasive quantum field. To properly understand the mechanisms of a QFT requires the understanding how classical field theories are constructed and subsequently quantized. This section will build up the necessary ingredients in formulating a complete QFT, following [2] and [6].

Classical field theory has been used historically as a Lorentz Invariant reformulation of classical physics [15]. It encodes all of the dynamics within the systems' action,

$$S[\mathcal{L}] = \int dx^4 \mathcal{L}, \tag{1.1}$$

where \mathcal{L} is the Lorentz Invariant Lagrangian density of the theory. The remainder of the thesis will refer to the Lagrangian density as the Lagrangian, as all theories considered will be cast in 4-dimensional spacetime. The action will be some functional of the theory's degrees-of-freedom or fields. Consider the example of a free scalar field

theory containing a single massive scalar field $\phi(x)$ with mass m ,

$$\mathcal{L} = \partial_\mu \phi(x) \partial^\mu \phi(x) - m^2 |\phi(x)|^2. \quad (1.2)$$

The Lagrangian is the composition of the kinetic (derivative) and potential (mass) terms. The classical solutions are realized at the extremum of the action $\delta S = 0$. The classical equations of motions (EOM) are manifest through the Euler-Lagrangian equations, which are natural consequences of the variational principle of the action.

A monumental insight is gained once a field theoretic formulation of classical physics is used—the relationship between symmetries and conserved quantities. Emmy Noether proved that if the action has a continuous symmetry then there exists a corresponding conservation law [16]. The Lagrangian of Eq. (1.2) has with it translational and time symmetry under, $x'_\mu \rightarrow x_\mu + \alpha \cdot \epsilon_\mu$, where α is some continuous parameter of the symmetry. These symmetries, by Noether's theorem, are the generators of both conservation of momentum and energy. Generally, for a set of n -fields that share a continuous symmetry parametrized by α , a conserved current can be constructed,

$$J_\mu = \sum_n \frac{\partial \mathcal{L}}{\partial(\partial_\mu \phi_n)} \frac{\delta \phi_n}{\delta \alpha}. \quad (1.3)$$

This is known as a Noether current and when conserved $\partial_\mu J^\mu = 0$ the time-like component will correspond to a conserved charge density. Physically conserved charges are generated by global symmetries where α is not a function of the spacetime coordinates. When $\alpha = \alpha(x)$ the symmetry becomes local, commonly referred to as a gauge symmetry. Gauge symmetries aren't physical, they merely highlight redundancies in the physical theory. This can be seen as to why the gauge choices of the photon field in electromagnetism aren't manifest in its physical observables. Therefore they do

not generate physical charges. Although gauge symmetries do imply the existence of a global symmetry. If the Lagrangian is invariant under a symmetry parametrized by $\alpha(x)$ than it must also be invariant under the same symmetry with global α . In the case of electromagnetism, the gauge symmetry of the photon field's Lagrangian implies a global symmetry which generates the conserved electric charge Q_e . This intimate relationship between gauge symmetries and global conserved charges is a consequence of both classical and quantum field theories and will be the prime motivator for the QFT of the Standard Model. Gauge symmetries will also assist in casting an intuitive form of the gravitational wave solutions of Einstein's field equations in Chapter 2.

There are two formulations of quantizing a classical field theory; the canonical approach and the path integral method. The canonical approach takes, for example, the action of Eq. (1.2) and promotes the fields to operators (second quantization). These field operators then act on Fock states representing momentum particle states embedded in Hilbert space. Quantum mechanical observables such as correlation functions and matrix elements can be constructed using these field operators. In the path integral formulation the quantum mechanical nature of the theory is not manifest through the quantization of the operators, but instead through the addition of non-classical field configurations. Matrix elements are calculated using the path integral of the action $S[\mathcal{L}]$ integrated through all field configurations; classical and non-classical paths. These two drastically different methods of constructing a QFT from a Lagrangian are theoretically equivalent and related by the Schwinger-Dyson equations.

Particle physics, specifically at colliding experiments, is focused on the local transformation of some initial state to a final state (i.e. from the particle beam to

the resulting particles measured). The transition matrix that embodies the scattering/transformation of particle states is called the S-matrix,

$$S = \langle p_1, p_2, \dots, p_n | \hat{S} | k_1, k_2, \dots, k_m \rangle. \quad (1.4)$$

It acts on asymptotic momentum Fock states of the incoming and outgoing particles and constructed using a perturbative expansion of the quantized Lagrangian. Each order of the expansion can be represented diagrammatically using Feynman diagrams.

1.2.2 Field Content of the Standard Model

The Standard Model of particle physics describes the visible matter content of the Universe and their interactions. It is formulated using the QFT framework discussed in the previous section. One of the beautiful outcomes of using a classical field theory was Noether's theorem; the intimate relationship between symmetries and conservation laws. Even when the theory is quantized these symmetries remain, along with their associated conserved currents¹. The Standard Model is formulated taking full advantage of this fact, where each of its fundamental particles become irreducible representations of a continuous gauge symmetry group. A top down approach is taken, where the Lagrangian is designed such that only terms that obey these symmetries are present.

The gauge groups underlining the Standard Model (SM) Lagrangian are: $SU(3) \times SU(2) \times U(1)$. The $SU(3)$ group governs the interactions of the strong force through quantum chromodynamics (QCD). $SU(2) \times U(1)$ governs the interactions of the electroweak sector. We expect $N^2 - 1$ generators for each $SU(N)$ and 1 generator for

¹This isn't exactly true. The quantization of a classical Lagrangian can break many classical symmetries, such as scale invariance. These broken symmetries result in anomalies in the quantized theory.

$U(1)$. These generators are represented by strength tensors with two Lorentz indices (μ, ν) . Meaning, there exists 8 gauge bosons in the QCD sector with field strength tensor $G_{\mu\nu}^b$ and 3+1 in the electroweak sector with $W_{\mu\nu}^a + B_{\mu\nu}$. These fields transform under the adjoint representation of their gauge groups. The portion of the Lagrangian that involves only the free gauge field strengths is,

$$\mathcal{L} \supset -\frac{1}{4}B_{\mu\nu}B^{\mu\nu} - \frac{1}{4}W_{\mu\nu}^aW^{a\mu\nu} - \frac{1}{4}G_{\mu\nu}^bG^{b\mu\nu}, \quad (1.5)$$

where the indices a, b run over all the gauge field generators of the respective sector. Similar to the photon in classical electromagnetism, a mass term is disallowed by gauge invariance.

The fermions of the Standard Model transform as fundamental representations of the gauge groups. Each generation of fermions couples uniquely to the gauge fields. We promote the derivatives in the kinetic terms of each fermion field to covariant derivatives $\partial_\mu \rightarrow D_\mu$. In doing so, the kinetic terms become invariant under the full gauge transformations of the SM. The covariant derivative of the SM is defined as,

$$D_\mu = \partial_\mu - ig' B_\mu Y - ig W_\mu^a T^a - ig_s G_\mu^a t^a. \quad (1.6)$$

where g', g are the coupling constants of the EW sector, and g_s for the QCD sector; Y is the hypercharge. T^a is related to the Pauli matrices $T^a = \sigma^a/2$, given by,

$$\sigma^1 = \begin{pmatrix} 0 & 1 \\ 1 & 0 \end{pmatrix}, \quad \sigma^2 = \begin{pmatrix} 0 & -i \\ i & 0 \end{pmatrix}, \quad \sigma^3 = \begin{pmatrix} 1 & 0 \\ 0 & -1 \end{pmatrix}. \quad (1.7)$$

Similar to T^a the generators t^a are related to the Gell-Mann matrices $t^a = \lambda^a/2$, given

by,

$$\begin{aligned}
\lambda^1 &= \begin{pmatrix} 0 & 1 \\ 1 & 0 \\ & & 0 \end{pmatrix}, & \lambda^2 &= \begin{pmatrix} 0 & -i \\ i & 0 \\ & & 0 \end{pmatrix}, & \lambda^3 &= \begin{pmatrix} 1 & & \\ & -1 & \\ & & 0 \end{pmatrix}, \\
\lambda^4 &= \begin{pmatrix} 0 & 1 \\ & 0 \\ 1 & 0 \end{pmatrix}, & \lambda^5 &= \begin{pmatrix} 0 & -i \\ & 0 \\ i & 0 \end{pmatrix}, & \lambda^6 &= \begin{pmatrix} 0 & & \\ & 0 & 1 \\ & 1 & 0 \end{pmatrix}, & (1.8) \\
\lambda^7 &= \begin{pmatrix} 0 & & \\ & 0 & -i \\ & i & 0 \end{pmatrix}, & \lambda^8 &= \frac{1}{\sqrt{3}} \begin{pmatrix} 1 & & \\ & 1 & \\ & & -2 \end{pmatrix}.
\end{aligned}$$

Here, only the diagonal and non-zero elements are shown. Unlike the gauge fields that are Lorentz vectors, the fermions are represented as Lorentz spinors ψ , further subdivided into left and right-handed chiral spinors $\psi_{R/L}$. Experiments show that the left and right handed fermions couple differently to the SM, implying that the chiral states are the fundamental relativistic states of the Universe. This is counter to non-relativistic quantum mechanics of the everyday, where the Dirac spinors are the considered states. Also, gauge invariance forbids any mass terms for the chiral fermions, disallowing terms like,

$$\mathcal{L} \subset -m(\bar{\psi}_R\psi_L + \bar{\psi}_L\psi_R), \tag{1.9}$$

whereas we know by measurements that they are massive. These stark differences in theory and measurements are remedied by the Higgs mechanism, which breaks the EW gauge group into the low energy symmetries of Electromagnetism.

Table 1.1 highlights how each fundamental particle of the SM transforms under each gauge group. Adjoint representations of $SU(3)$ and $SU(2)$ are denoted by $\mathbf{8}$ and $\mathbf{3}$ respectively. Fundamental representations of the of $SU(3)$ and $SU(2)$ are denoted by $\mathbf{3}$ and $\mathbf{2}$ respectively. The fundamental representations of $SU(2)$ are commonly refer to as EW doublets. They contain EW pairs like the electron and its associated electron neutrino, or the up an down quarks. Keeping in mind that only the left handed fermions are charged under this group.

	$SU(3)_C$	$SU(2)_L$	$U(1)_Y$	Spin
H	$\mathbf{1}$	$\mathbf{2}$	$1/2$	0
Q_L^f	$\mathbf{3}$	$\mathbf{2}$	$1/6$	$1/2$
U_R^f	$\mathbf{3}$	$\mathbf{1}$	$2/3$	$1/2$
D_R^f	$\mathbf{3}$	$\mathbf{1}$	$-1/3$	$1/2$
L_L^f	$\mathbf{1}$	$\mathbf{2}$	$-1/2$	$1/2$
E_R^f	$\mathbf{1}$	$\mathbf{1}$	-1	$1/2$
B_μ	$\mathbf{1}$	$\mathbf{1}$	0	1
W_μ^a	$\mathbf{1}$	$\mathbf{3}$	0	1
G_μ^b	$\mathbf{8}$	$\mathbf{1}$	0	1

Table 1.1: Field content of the Standard Model. a runs from 1 to 3, and b from 1 to 8. The L and R next to a spin $1/2$ field represents its chirality. f is the generational index which runs from 1 to 3.

1.2.3 Higgs Mechanism

The Higgs boson was discovered and verified by the CMS and ATLAS experiments hosted at the Large Hadron Collider in 2012 [17,18]. Not only did these measurements verify the existence of a fundamental scalar field in the SM, they also proved the process which generates the measured masses of the SM fields—spontaneous symmetry breaking. The false vacuum of the higgs scalar will generate terms that break the EW gauge symmetries. When the dust settles, the low energy symmetries of electro-

magnetism $U(1)_{\text{EM}}$ are recovered. This almost magical process of breaking abstract symmetries of the theory by the introduction of scalar fields will lead to the concepts of phase transitions in Chapter 2.

Focusing on the EW sector and referencing Table 1.1, the Higgs boson of the SM transforms as a complex scalar doublet with hypercharge $Y = 1/2$. Therefore the higgs doublet can be represented by 2×2 degrees of freedom as,

$$H = \frac{1}{\sqrt{2}} \begin{pmatrix} \phi_1 + i\phi_2 \\ \phi_3 + i\phi_4 \end{pmatrix}, \quad (1.10)$$

where ϕ_i are real scalars. Since it's a complex scalar it transforms similarly to the Lagrangian of Eq. (1.2), replaced with the gauge invariant covariant derivative,

$$\mathcal{L} \subset (D_\mu H)^\dagger (D^\mu H) - V(H). \quad (1.11)$$

In this case, the potential term $V(H)$ includes only terms that are powers of $H^\dagger H$ to preserve hypercharge. The higgs potential of the SM is given by,

$$V(H) = -\mu^2 H^\dagger H + \lambda (H^\dagger H)^2, \quad (1.12)$$

where $-\mu$ and λ are real parameters. Knowing that these parameters can be free, the form of the potential can lead to concerning outcomes. Independent of what $-\mu$ is, if λ were to be negative, the potential would be boundless from below. Meaning, the universe would have no stable vacuum configuration. We know from observations of our Universe, and from the fact that you can read this, that our universe is currently in, and has been in, a stable configuration. Assuming $\lambda > 0$, the sign of $-\mu$ will dictate whether the vacuum state is stable or metastable. If $-\mu > 0$, the vacuum

state is at the global minimum. If $-\mu < 0$, the vacuum state is not at the origin and the field will spontaneously transition accordingly. This transition into the new vacuum state will break the $SU(2) \times U(1)$ symmetry into $U(1)_{\text{EM}}$.

Taking the derivative of the potential and finding its minimum leads to

$$v \equiv H^\dagger H = \frac{\mu^2}{2\lambda}. \quad (1.13)$$

Here, v is referred to as the vacuum expectation value (vev). This reduces to a 3-dimensional surface in the 4-dimensional ϕ_i space. We then expand the higgs field around this vev, where we take the direction of ϕ_3 to be the radial mode such that $\phi_3 = h + v$, leading to,

$$H = \frac{1}{\sqrt{2}} \begin{pmatrix} \phi_1 + i\phi_2 \\ h + v + i\phi_4 \end{pmatrix}. \quad (1.14)$$

Plugging this back into the Lagrangian results in h receiving a mass of $m_h = \sqrt{2\lambda v^2}$ and the remaining ϕ_i become massless. These massless scalar degrees of freedom are known as Goldstone bosons and don't contribute to the physical theory. Therefore with the right choice of gauge these Goldstone modes disappear. In essence, when gauged away, these modes become intimately related to the physical polarizations of the gauge bosons.

In Unitary gauge, the higgs doublet reduces to,

$$H = \frac{1}{\sqrt{2}} \begin{pmatrix} 0 \\ h + v \end{pmatrix}. \quad (1.15)$$

The higgs gauge interactions are a result of the kinetic term in the Lagrangian. Ex-

panding the covariant derivative in terms of h and v we find,

$$D_\mu H = (\partial_\mu - ig'B_\mu Y - igW_\mu^a T^a) \frac{1}{\sqrt{2}} \begin{pmatrix} 0 \\ h + v \end{pmatrix}. \quad (1.16)$$

Keeping in mind that the higgs doublet is invariant under QCD the $SU(3)$ generators t^a are dropped. Expanding the full kinetic term and completing the squares results in,

$$(D_\mu H)^\dagger (D^\mu H) = \frac{1}{2} \partial_\mu h \partial^\mu h + \frac{1}{8} (h + v)^2 [g^2 |W_\mu^1 - iW_\mu^2|^2 + (gW_\mu^3 - g'B_\mu)^2]. \quad (1.17)$$

All terms with respect to h are the higgs interactions with the various gauge bosons. Whereas, the terms only in v^2 will generate mass and self interaction terms for the gauge fields. This can be easily seen by rotating the basis of the gauge fields by,

$$\begin{aligned} W_\mu^\pm &= \frac{1}{\sqrt{2}} (W_\mu^1 \mp iW_\mu^2) \\ Z_\mu &= \frac{1}{\sqrt{g + g'}} (gW_\mu^3 - g'B_\mu), \\ A_\mu &= \frac{1}{\sqrt{g - g'}} (g'W_\mu^3 + gB_\mu) \end{aligned} \quad (1.18)$$

Where A_μ is defined as the field orthogonal to Z_μ , and W^\pm represent the complex conjugate pairing of (W^1, W^2) . Expanding Eq. (1.17) in the new basis, and picking out the terms quadratic in the fields gives,

$$\mathcal{L} \subset \frac{g^2 v^2}{4} W_\mu^- W^{+\mu} + \frac{(g^2 + g'^2)}{8} v^2 Z_\mu Z^\mu. \quad (1.19)$$

These represent the mass terms of the gauge fields. Knowing that the mass terms for

a complex field is $m_W^2 W_\mu^+ W^{-\mu}$ and $(m_Z^2/2) Z_\mu Z^\mu$ and for a real field, we can pick off the masses as,

$$M_W = \frac{g}{2}v, \quad M_Z = \frac{\sqrt{g^2 + g'^2}}{2}v, \quad M_A = 0. \quad (1.20)$$

It's apparent that A_μ naturally becomes massless and represents the photon field of $U(1)_{\text{EM}}$ electromagnetism.

Now that the EW symmetry has broken down to EM we can ask how the resulting EM conserved charge relates to the unbroken charges T^a, Y . To see this Eq. (1.6) is inverted in terms of the new field basis of the broken sector,

$$\begin{aligned} D_\mu = & \partial_\mu - ig_s G_\mu^a t^a - i\frac{g}{\sqrt{2}}(W_\mu^+ T^+ + W_\mu^- T^-) \\ & - \frac{Z_\mu}{\sqrt{g^2 + g'^2}}(g^2 T^3 - g'^2 Y) - iA_\mu e(T^3 + Y), \end{aligned} \quad (1.21)$$

Focusing on the photon field, the fundamental electric charge unit e and the conserved charge Q are defined as,

$$e = \frac{gg'}{\sqrt{g^2 + g'^2}}, \quad Q = T^3 + Y \quad (1.22)$$

With the gauge field masses being naturally generated from the SSB of the EW sector, the question of how fermion masses are generated can be answered. As previously mentioned the fermion sector is complicated, because of its multiple generations and left-right handed chiral nature. Instead of proving the mass generation of all fermionic matter only the electron case will be explored as a proof of concept. Following the mandate that only terms obeying the group structure of the SM exist

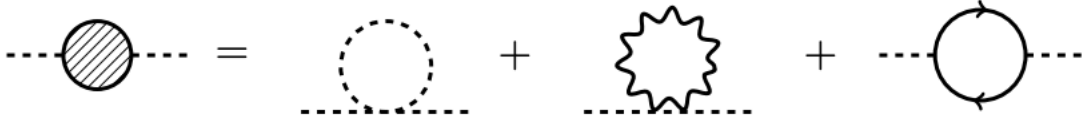


Figure 1.1: One-loop quantum corrections on the mass of a scalar field from scalar, gauge, and fermion fields [19].

leads to the so called Yukawa terms between the higgs doublet and electron fields,

$$\mathcal{L} \subset -y\bar{L}He_R + h.c. \quad (1.23)$$

Here, y is the Yukawa coupling and L is the left handed electron-neutrino doublet. Once these terms are expanded after SSB, electron mass terms are generated as a by-product in the form of

$$\mathcal{L} \subset \frac{yv}{\sqrt{2}}(\bar{e}_Le_R + \bar{e}_Re_L). \quad (1.24)$$

Leading to masses for the electron equal to $m_e = yv/\sqrt{2}$. This is the scheme in which masses are generated for the entire fermion sector.

1.2.3.1 The Hierarchy Problem

Calculations of physical quantities in a QFT are followed through by taking advantage of perturbative expansions of the fields. Each term in the expansion expressing a different order in the calculation, corresponding to unique Feynman diagrams. We can now investigate how these higher order quantum corrections affect the masses generated by SSB.

One-loop Feynman diagrams represent the first order corrections to the particle masses. If allowed, these loops involve fermions, gauge fields, and scalars as seen in Fig. 1.1. Loop diagrams exhibit divergent behaviour due to integrating over all possible modes of the internal looping particles. These divergent terms are a consequence

of the scale dependence of the calculation. Knowing that the SM is some low scale effective theory, calculations within it become sensitive to some unknown theory at a higher scale Λ . When calculating physical quantities in the SM, Λ is taken to be the cutoff scale used to regulate the theory.

Fermion and gauge field masses are protected from these large quantum corrections by symmetry. In the case of fermions, the quantum corrections must be proportional to the particles masses m_f , not the cutoff scale Λ . The reason being that each fundamental fermion is subject to a chiral symmetry in the massless limit. Meaning, the theory preserves the massless left and right handed states in the unbroken theory. Similarly, radiative corrections to the gauge field masses must tend to zero in the massless limit, this time due to gauge symmetry. The heart of the hierarchy problem lies in the quantum corrections of scalar masses. Unlike fermions and gauge fields, fundamental scalars are not protected by the same symmetries. By dimensional analysis alone, their quantum corrections must be proportional to the cut off scale of the theory. In the case of the SM higgs,

$$\delta m_h^2 \propto \frac{\Lambda^2}{32\pi^2}. \tag{1.25}$$

The Higgs mass is quadratically sensitive to any mass scale of new physics. If $\Lambda \gg 10$ TeV, then $\delta m_h^2 \gg m_h^2$. This makes the current higgs mass measurement of $m_h = 125$ GeV [17, 18] a disturbing outcome, forcing theorists to unnaturally tune the theory. Even worse, the only known scale that supersedes the SM is the quantum gravity scale $\Lambda \sim M_{\text{Pl}}$. In Chapter 2, the theory of N naturalness will be introduced as a natural solution to the hierarchy problem by greatly reducing the impact M_{Pl} has on the cutoff scale by the addition of multiple hidden sectors. For example, within the standard N naturalness framework the number of hidden sectors plays a role in suppressing the

quadratic cutoff. If the values of m_h^2 are randomly selected between each sector, then some sectors should be accidentally tuned to the $1/N$ level. Meaning, as the number of sectors increases, so does the possible suppression power of the cut off: $m_h^2 \sim \Lambda/N$

1.2.4 Quantum Chromodynamics

Similar to the masses of particles, the couplings of the SM are effected by radiative quantum corrections. Without loop corrections (tree level) the couplings are constant. Meaning, the couplings inferred² by measurements are equal to the couplings in the Lagrangian. When loop corrections are considered the couplings vary with (energy) scale μ , not to be confused with the cutoff scale of the previous section. The perturbative expansion used for calculations relies on small couplings. If the couplings run too large, perturbation theory fails. The consequences of a scale dependent couplings becomes apparent when comparing the QCD coupling α_s with that of Quantum Electrodynamics (QED) α . In QED the coupling increases with the scale, leading to small couplings at low scales. This is not the case for QCD.

QCD is the QFT of the strong force with symmetry gauge group $SU(3)$. Its quantum numbers are referred to as colours, with $N = 3$ distinct states. The gluon gauge fields and quarks are the only matter content of the SM charged under $SU(3)$. The unique structure of the gauge group in tandem with its particle content causes the theory to become non-perturbative at low energy scales. This can be seen through the β -function, the differential equation that describes the evolutionary flow of the couplings with scale μ , given by,

$$-\mu^2 \frac{\partial \alpha_s(\mu^2)}{\partial \mu^2} = -\beta(\alpha) = \frac{\beta_0}{4\pi} \alpha_s^2 + \frac{\beta_1}{(4\pi)^2} \alpha_s^3 + \dots + \mathcal{O}(\alpha_s^n), \quad (1.26)$$

²The couplings are not directly measurement, instead they are inferred by cross section and decay rate measurements.

where β_i are the i^{th} loop contributions to the β -function. In a general $SU(N)$ theory with n_f flavours of fundamental representations (i.e. quarks), the first coefficient of β_i is,

$$\beta_0 = \left(\frac{11}{3}N - \frac{4}{6}n_f \right). \quad (1.27)$$

Notice that the sign of β_0 , and therefore the running of Eq. (1.26), is dependent on both N and n_f . If a theory runs positive $\beta(\alpha) > 0$, the theory will be perturbative at low energy scales. If instead $\beta(\alpha) < 0$, the theory becomes non-perturbative at the low energies. In the case of QCD, Eq. (1.26) can be solved with respect to an arbitrary reference scale. The coupling α_s at one-loop is then,

$$\alpha_s(\mu^2) = \frac{1}{\frac{\beta_0}{4\pi} \log \left(\frac{\mu^2}{\Lambda_{QCD}^2} \right)}, \quad (1.28)$$

where $\Lambda_{QCD} \approx 250$ MeV is the scale in which the coupling becomes non-perturbative. It can be seen that the coupling becomes large with small μ , in the negative direction of the QED coupling. Around Λ_{QCD} the theory confines, where the quarks join into colour singlet (neutral) configurations, hadrons. Hadrons are the only states observed experimentally. Baryons are hadrons that contain three quarks with examples like the proton and neutron. Mesons are hadrons with two quarks with the most notable being the pions. In the direction where the scales become high, the coupling becomes small. In this regime, the quarks become asymptotically free and easily produced at particle colliders. These free quarks shower into high multiplicities producing parton showers, which will be discussed in Chapter 3

1.3 Dark Matter and Hidden Sectors

1.3.1 Observations

We know through extensive astrophysical observations over the past half a century that the SM is incomplete [20]. Specifically, these observations show that the Universe contains a source of invisible matter that either interacts extremely weakly to the SM or not at all. This invisible matter is commonly known as dark matter. Its initial evidence were based on observations of Coma cluster in the 1930s. These observations [21], conducted by Fritz Zwicky, measured galaxy velocities dispersions $\mathcal{O}(100)$ larger than predicted for a virialized system of galaxies (i.e. galactic clusters). Although, dark matter was not seriously investigated until the measurements of galactic rotation curves, within our local group, [22] showed worrying inconsistencies. It was shown that the galaxy's light output, generated by baryonic mass, did not account for the total gravitational mass inferred by their rotation rates. Further galactic studies of velocity dispersions and luminosity functions reaffirmed these measurements. In the current era, we have numerous independent measurements corroborating the existence of dark matter. These include, gravitational lensing of foreground objects [23], Bullet Cluster observations [24], and anisotropies of the cosmic microwave background [25]. These observations lead to the current Λ CDM cosmological model of the Universe. Λ CDM refers to the various components of the Universe, which are measured to be $\sim 4\%$ baryons; $\sim 23\%$ dark matter; and $\sim 71\%$ dark energy. Λ CDM stands for cold dark matter, where the dark matter had thermally decoupled from the Universe's radiation bath at an early time such that today's dark matter abundance is left non-relativistic.

1.3.2 The Hidden Valley

The hidden valley (HV) was first proposed in [26,27] as an extension to the SM. Each particle in the SM is charged under the SM gauge group, whereas the HV contains only particles charged under different group G_v . These valley particles, charged under G_v , have masses at similar scales to the SM. By these conditions alone, the HV would be completely decoupled from the SM and no interactions would occur. Instead, the valley particles are made to be weakly coupled to the SM by the addition of heavy mediating particles charged under both gauge groups. This concept of a heavy mediator communicating between two similarly light sectors can be illustrated as a potential barrier between two valleys, hence the name.

Depending on how heavy the mediator is, and therefore how weakly the HV couples, past particle colliders may have been too low energy to cross the energetic barrier. With the deployment of more and more energetic colliders, such as the LHC, the valley particles have a higher chance of being produced. Once produced at colliding experiments, the valley particles may decay back into lighter SM states. This decay process can be mediated by the same production mediator or a completely separate decay portal. What becomes phenomenologically more interesting is when the decay portal is heavy. In this case, the decaying valley particles lifetime is considerably enhanced. Independent of the gauge group of the HV, the decay width of a valley particle scales as,

$$\Gamma \propto \frac{g_v^4}{M_X^4} m_D^5, \tag{1.29}$$

where g_v is the coupling of the mediator X to the HV, M_X is the mass of the decay mediator, and m_D is the mass of the decaying valley particle. When $M_X \sim 1$ TeV the decays lengths become macroscopic relative to modern particle detector pack-

ages. Keeping in mind that these valley particles are not charged under EM, they will traverse macroscopic distances invisibly before they decay. Therefore leading to novel invisible particle track signatures. The remaining chapters will refer to invisible particles and valley particles interchangeably.

1.3.3 Dark QCD

In the previous section the gauge group G_v was not specified, but the decay rates could still be estimated. Instead, we can take the hidden valley group to be a copy of QCD referred to as dark QCD, $G_v = SU(3)_D$. Similar to Section 1.2.4 the matter content of the theory will experience confinement, depending on the number of dark flavours N_f . The sector will have a corresponding dark QCD scale Λ_D .

	$SU(3)_C$	$SU(2)_L$	$U(1)_Y$	$SU(3)_D$	Spin
Q_d	1	1	0	3	1/2
X_d	3	1	1/3	3	0
Z_d	1	1	0	1	1

Table 1.2: Field content of the hidden valley charged under dark QCD. The fundamental representation of dark qcd is that of the dark quark Q_d . Vector Z_d and bifundamental X_d mediators are taken as example portals between the two sectors.

Confining hidden sectors around the GeV scale could contain stable invisible hadrons as a possible dark matter candidate [28]. This is why many theoretical models are motivated by hidden sectors with QCD-like dynamics. The rest of this section will discuss the implications of the HV sector charged under dark QCD.

Hidden sectors charged under dark QCD will contain a similar spectrum of particles to that of the SM QCD sector. Like in QCD, the dark quark will transform under the fundamental representation of $SU(N)_D$. Depending on the number of flavours of dark quarks, the confined sector will contain analogues to the mesons

and baryons, built up from various flavour combinations. The HV allows the communication between QCD and the SM through production and decay mediators. We will assume the decay portal is the same as the production mediator. In Chapter 5 the focus will be on two types of mediators; a scalar bi-fundamental X and vector Z_D . We take both fields to couple exclusively to the QCD sector of the SM. The additional fields and how they are charged under the gauge groups is shown in Table 1.2.

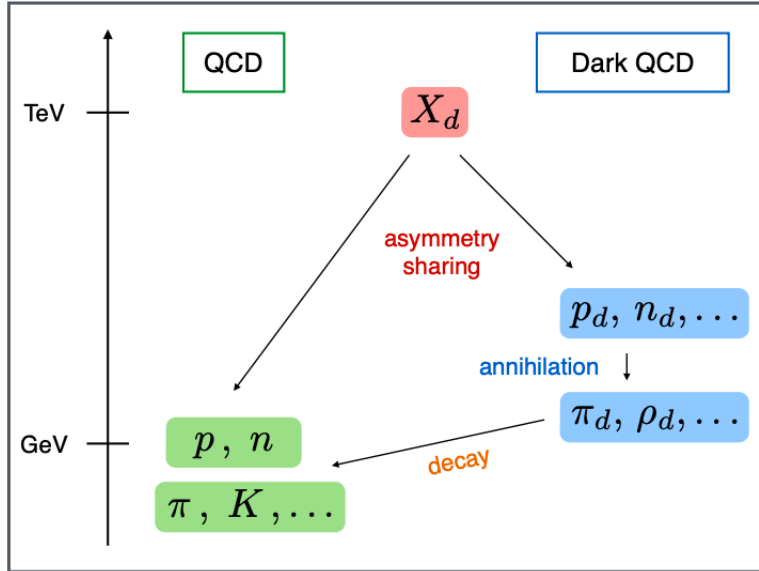


Figure 1.2: A diagram from [29] illustrating a hidden valley charged under dark QCD around the GeV scale. The communicating portal is a TeV scale mediator X_d , charged under both groups. The dark sector will contain a spectrum of hadrons analogous to QCD, where the non-stable mesons decay back into the SM through X .

Fig. 1.2 is an illustrative representation of how the two sectors interact with each other. The heavy mediator X can be produced through p-p collisions at energies around the TeV scale. Once produced, it'll decay some fraction of the time to dark quarks. These quarks will form dark mesons and stable baryons. The baryons are considered stable on the time scale of the Universe. The mesons can decay back to the SM by the X according to Eq. (1.29). The hierarchy between M_X and the

Λ_D producing novel macroscopic lifetimes for the dark mesons. This will be the foundation for how emerging jets are produced at particle colliders in Chapter 5.

1.3.4 Asymmetric Dark Matter

The scale of dark QCD sector was taken to be around the GeV in the previous section. This choice is motivated by the theory of asymmetric dark matter (ADM). In ADM the dark matter abundance measured today and baryonic matter abundances were generated similarly. The motivation comes from noticing that the dark matter abundance is five times larger than that of baryonic matter.

By symmetry alone, we expect that the early universe would have an equal number of particles and antiparticles. If that were true the particles and their antiparticles would have completely annihilated in the early Universe. Instead some time during the early universe, a tiny excess of baryons B over antibaryons \bar{B} must have developed, parametrized by [30]

$$\eta \equiv \frac{n_B - n_{\bar{B}}}{s} \sim 10^{-10}, \quad (1.30)$$

where s is the entropy density which will be discussed in Chapter 2. η represents the excess fraction of baryons that make up the observable Universe today. The models that attempt to explain this asymmetry are under the guise of baryogenesis and outside the scope of this thesis. Instead we assume that the dark sector containing similarly stable hadronic states (dark protons) had undergone the same asymmetry generating process. Therefore, the two sectors should share a similar η . The only way to retrieve the correct abundances today is for the hidden sector to have stable masses five times heavier than the SM.

Chapter 2

Cosmology

*“If you want to make an apple pie from
scratch, you must first create the universe.”*
— Carl Sagan

2.1 The Standard Cosmology

2.1.1 FLRW Universe & Thermal Histories

The Universe is nearly 14 billions years old, a time scale incomprehensible when compared to humanity’s small blip of existence. Every few years our understanding of the Universe advances. Our understanding of the Universe’s time-line fifty years ago was substantially different to that of today’s, as shown in Fig. 2.1. But how can we justify such grandiose statements about the Universe when we look at it through a limited lens? The answer to this question leads to one of the most profound assumptions in cosmology. Known as the cosmological principle, this assumption states that our observable universe is isotropic (no preferred direction) and homogeneous (no preferred position). The cosmological principle immediately goes against the grain of our own

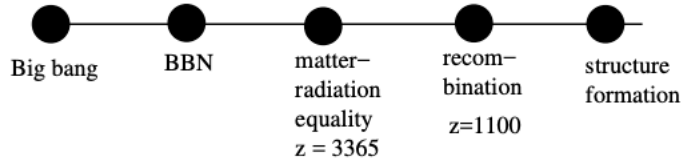


FIG. 1. The cosmological timeline, *ca.* 1970.

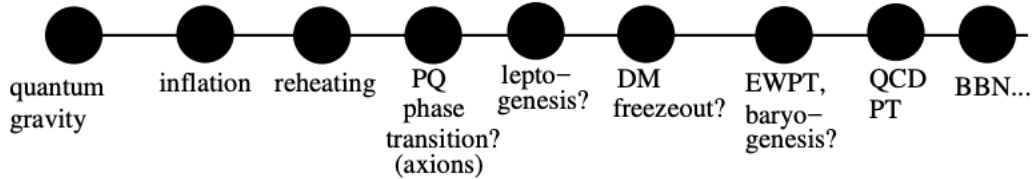


FIG. 2. The cosmological timeline, *ca.* 2018.

Figure 2.1: The cosmological timeline, *ca.* 2018 [31]. The timeline shows the various epochs in the standard cosmology, including; quantum gravity (QG), inflation, Peccei Quinn (PQ) phase transition, leptogenesis, dark matter (DM) freezeout, electroweak phase transition (EWPT), baryogenesis, quantum chromodynamic phase transition (QCD PT), and big bang nucleosynthesis (BBN).

intuition as we see the Universe as bleak, sparsely populated, and adorned with complex galactic structures. Measurements of the observable universe’s global structure continue to affirm an isotropic and homogeneous Universe. Random samples of galaxies do not have their axes of symmetry aligned. Deep field measurements of different patches in the night sky correlate in global densities. These observations, and many more, show that the cosmological principle must be the foundational groundwork onto which all cosmological models are built from. This section will follow [3].

The Friedmann-Lemaître-Robertson-Walker (FLRW) metric describes the local geometries of the Universe stemming from a big bang. It can be derived using only geometric arguments while assuming an isotropic and homogeneous evolving Universe. The general (FLRW) metric is defined in comoving coordinates (t, r, θ, ϕ) as,

$$ds^2 = dt^2 - a^2(t) \left(\frac{dr^2}{1 - kr^2} + r^2 d\theta^2 + r^2 \sin^2(\theta) d\phi^2 \right), \quad (2.1)$$

where $a(t)$ is the scale factor which dictates how the geometry evolves, and k the curvature factor. The curvature factor can be classified into negative curvature $k = -1$, positive curvature $k = 1$, and a flat space-time $k = 0$. The dynamics of the FLRW Universe is fully dictated by the scale factor.

Simple kinematic arguments can be made using just the FLRW metric without having to solve for the explicit time dependence of the scale factor. These arguments generate expressions on how various cosmological scales change with $a(t)$. Comparing two separate scales λ and λ_0 represented by the wavelengths of propagating light during epochs t and t_0 , respectively, reveals the commonly used expression for the cosmological red shift z ,

$$\frac{a(t_0)}{a(t)} = \frac{\lambda_0}{\lambda} \equiv 1 + z. \quad (2.2)$$

The proper interpretation of Eq. (2.2) is to think of the wavelengths/scales red shifting due to the stretching of space as the scale factor evolves. Knowing that the cosmological red shift z or scale factor $a(t)$ are global manifestations of the space-time geometry, astronomers use them as measures of distance (and time) to different epochs in the cosmological timeline.

Making sense of the thermal history of the Universe and its dynamics requires knowing the explicit form of the scale factor. Otherwise, we can only make broad kinematical statements for a given epoch t_0 . The Einstein field equations explain how the geometry of space-time is affected by the embedded matter/energy content. A deeper discussion of the Einstein field equations will be presented in Section 2.3 in the context of gravitational waves. Given the matter content of the Universe with energy density ρ and assuming a FLRW metric the solution to the field equations

take the form of the Friedmann equation,

$$\left(\frac{\dot{a}}{a}\right)^2 = \frac{8\pi}{3}\rho - \frac{k}{a(t)^2}. \quad (2.3)$$

The left hand side of the Friedmann equation is commonly defined as $H \equiv (\dot{a}/a)$. The choice in notation to that of the Hubble constant H_0 is not done by accident. At our local time $t = t_0$ we can retrieve the Hubble constant measured today $H = H_0$. This should not come as a surprise as the Hubble constant was first measured using cosmological red shifts z . Once a curvature k and energy density ρ are known, the explicit evolution of $a(t)$ can be solved. Energy densities are described in terms of components of the energy-mass content of the Universe. These three components are pressure-less matter, radiation, and vacuum energy. Each with their own distinct equations of states $P = f(\rho)$. More importantly, we can see how the energy densities scale with the scale factor,

$$\rho \sim \begin{cases} a(t)^{-3}, & \text{Matter} \\ a(t)^{-4}, & \text{Radiation} \\ \text{constant}, & \text{Vacuum} \end{cases} \quad (2.4)$$

There is a qualitative explanation for the differences in scaling laws between matter and radiation. The density of matter will scale with the volume of 3 dimensional space. Radiation, on the other hand, not only scales with the 3-volume but also by another factor of $a(t)^{-1}$ due to red shifting in Eq. (2.2). The additional factor of $a(t)^{-1}$ has large implications on the evolution between an epoch which is radiation dominated $\rho \approx \rho_r$ and one that is matter dominated $\rho \approx \rho_m$, which plays an important role in the Universe's thermal history. The odd form of the vacuum energy density plays

a crucial role in the Universe's initial rapid expansion during inflation [32]. Taking another look at Eq. (2.3) and considering the case of zero curvature $k = 0$ leads to a characteristic energy density referred to as the critical energy density $\rho_c = 3H^2/8\pi$. By convention, we define dimensionless energy density parameters using the critical density,

$$\Omega_r = \frac{\rho_r}{\rho_c}, \quad \Omega_m = \frac{\rho_m}{\rho_c}, \quad \Omega_v = \frac{\rho_v}{\rho_c}. \quad (2.5)$$

The particles in the early Universe, to a good approximation, were in (local) thermodynamic equilibrium. This assumption allows us to trace back the history of the Universe in the context of thermal dynamics. Focusing again on the energy density, we can segment the matter and radiation contributions using statistical mechanics. Fermionic matter is described by Fermi-Dirac statistics while Bosonic radiation is described by Bose-Einstein statistics. The energy density is therefore given by its respective statistical distribution $f(\hat{p})$ over the entire phase space,

$$\rho = \frac{g}{(2\pi)^3} \int E(\hat{p}) f(\hat{p}) d^3\hat{p}, \quad (2.6)$$

here g is the internal degrees of freedom of the ensemble. In the non-relativistic regime $m \gg T$, Eq. (2.6) reduces to the Maxwell-Boltzmann distribution and imparts very little to the overall energy density of the early Universe. In the relativistic limit $m \ll T$ the energy density has a much stronger temperature dependence,

$$\rho \sim \begin{cases} (\pi^2/30)gT^4, & \text{Bose-Einstein} \\ (7/8)(\pi^2/30)gT^4, & \text{Fermi-Dirac.} \end{cases} \quad (2.7)$$

After summing over only the relativistic species we come to the overall en-

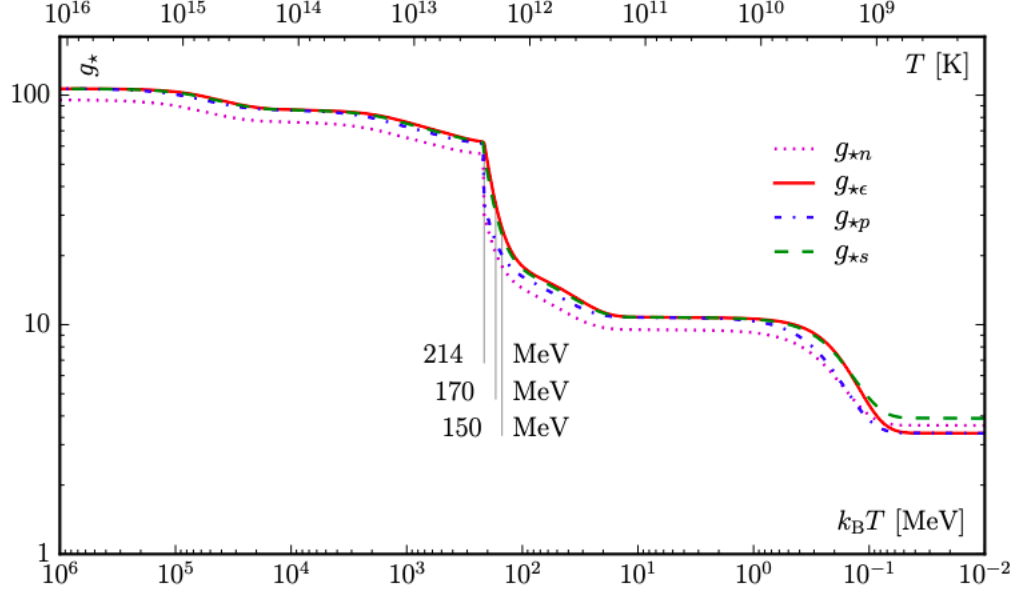


Figure 2.2: The thermal history of effective relativistic degrees of freedom g_* as a function of temperature. Also included are effective degrees of freedom for number density g_n , pressure g_p , and entropy g_s taken from [33].

energy density of the Universe's combined matter and radiation components at a given temperature T as,

$$\rho_R = \frac{\pi^2}{30} g_* T^4 \quad (2.8)$$

Where g_* is the relativistic degrees of freedom at temperature T , such that species with mass lower than the temperature scale T are considered relativistic. As the temperature drops, larger mass particles begin to decouple from the thermal bath. The relativistic degrees of freedom can be broken up into its fermionic and bosonic contributions,

$$g_* = \sum_{i=\text{bosons}} g_i \left(\frac{T_i}{T} \right)^4 + \frac{7}{8} \sum_{i=\text{fermions}} g_i \left(\frac{T_i}{T} \right)^4. \quad (2.9)$$

Fig. 2.2 shows the evolution of the relativistic degrees of freedom. Another useful concept is that of the total entropy of the Universe's thermal bath S . The

second law of thermodynamics states that the entropy must be constant for reversible processes of the thermal bath. Therefore it can be stated that,

$$S = g_{*s} T^3 \cdot R^3 = \text{const.} , \quad (2.10)$$

where g_{*s} has the same form as in Eq. (2.9) but with the temperature dependence changed to T^3 ,

$$g_{*s} = \sum_{i=\text{bosons}} g_i \left(\frac{T_i}{T} \right)^3 + \frac{7}{8} \sum_{i=\text{fermions}} g_i \left(\frac{T_i}{T} \right)^3 . \quad (2.11)$$

Note that this is not true for irreversible process such as spontaneous phase transitions. In such cases, discontinuities must be considered. This implies that the temperature of the thermal bath scales with the comoving volume of space,

$$T \propto R^{-1}, \quad (2.12)$$

ignoring the small effects from g_{*s} as species enter in and out of equilibrium. The above expression also holds true for radiation decoupled from the thermal bath¹. Eq. (2.12) provides us with a way to map the evolution of the universe through the temperature of it's component species. It solidifies the intuitive notation that as the Universe evolves and expands it subsequently gets colder. For the remainder of the thesis the temperature will be used to dictate different moments in the Universe, assuming local thermodynamic equilibrium. Temperatures will be reported in units of energy by making use of the Boltzmann constant $k_B T$.

¹The scaling is R^{-2} for massive particles that are thermally decoupled.

2.1.1.1 Neutrino decoupling

We start our consideration of the Universe at a temperature around $T = 10^{12}$ K, which in energy units is $T \sim 100$ MeV. In this epoch the temperature is well below the rest masses of protons and neutrons, therefore halting their production mechanisms. Meaning, the abundances of the heavier particles were set in at an earlier time. The mechanism of the baryonic abundances was briefly discussed in Chapter 1. Primordial neutrinos have a combined mass of less than 1 MeV [34]. Therefore the scattering between electrons and neutrinos is still efficient. For as long as the scattering process is efficient the neutrinos will remain coupled to the thermal bath of radiation. Eventually the expansion rate of the Universe will overtake the overall rate of the scattering processes. This occurs at $T \sim 10^{10}$ K at which the neutrinos start to decouple. The process of thermal decoupling from the other particles is called *freeze-out*. Once frozen out these neutrinos become a relic of this era and free stream throughout the Universe. However, this neutrino background is too low energy today to be seen with current detectors.

Right after neutrino decoupling, electron-positron pairs begin to pair annihilate to photons. Pair annihilation injects additional energy to the radiation bath of photons. This changes the energy distribution of photons. Since the neutrinos have decoupled at this time, they do not benefit from this injection of energy. This temperature difference between the neutrino and photon baths is preserved to this day as $T_\nu/T_r = (11/4)^{1/3}$ [3]. We can relate this to the overall energy density of radiation ρ_r to the energy density of relic photons ρ_γ as,

$$\rho_\nu = \rho_\gamma \left(1 + N_{\text{eff}} \frac{7}{8} \left(\frac{4}{11} \right)^{4/3} \right), \quad (2.13)$$

where N_{eff} is the number of effective neutrino species. It accounts for any radiation

energy density not accounted for by photons. The current Standard Model prediction is $N_{\text{eff}} = 3.046$ [35] compared to the bounds from studies of the Cosmic Microwave Background (CMB) by Planck combined with baryon acoustic oscillations (BAO) measurements [36],

$$N_{\text{eff}} = 2.99_{-0.33}^{+0.34}. \quad (2.14)$$

2.1.1.2 Recombination

Further down the line of cosmic history, at $T \sim 0.3$ eV, the electrons begin to recombine into the primordial atoms. Beforehand, photons were contained in a hot dense plasma of electrons. As the Universe cools and electrons recombine into atoms, the photons are no longer limited to a small mean free path. The radiation bath of photons is now free to stream throughout the Universe. The moment at which photons are free streaming is called the *last-scattering surface*. As the photons traverse the Universe their energy red shift to lower energies. Today the temperature of the photon bath is $T \sim 10^{-4}$ eV. We refer to the free streaming background photons today as the Cosmic Microwave Background (CMB). Experiments such as the Planck experiment [37] use the CMB to map out the Universe at the time of last-scattering. This is earliest time at which we can measure the early Universe through electromagnetic radiation.

2.1.2 Phase Transitions

Well before the thermal decoupling of neutrinos and the recombination of primordial atoms, the Universe had gone through many phases. Phase transitions, the transitory mechanisms between one substance's phase to another, are commonly seen throughout nature. Taking another look at our updated cosmological timeline in Fig. 2.1 we can notice the emergence of epochs that host various phase transitions (PT).

Just from the labels of each of these epochs we can get a sense that these processes occur throughout many different sectors of the Standard Model. The electroweak phase transition (EWPT) is the EW sector's transition from its fundamental massless fermions to the massive particles that we commonly see today. We know from Chapter 1 that the Higgs mechanism is what generates fermion mass through spontaneous symmetry breaking. Early Universe PT and spontaneous symmetry breaking go hand-in-hand. This leads to sectors of particles with symmetry properties that are affected by the temperature T of its surrounding thermal medium. Therefore, for particles in thermal equilibrium the symmetry breaking mechanism becomes a function of the bath's temperature T .

The symmetries of the EW sector $SU(2) \times U(1)$ brake down to the symmetry of EM $U(1)$ through spontaneous symmetry breaking of the Higgs potential. This process occurs once the Higgs potential acquires a new global minimum. We can generalize this by assuming a general scalar field ϕ with some potential $V(\phi)$ as part of the full Lagrangian,

$$\mathcal{L} = \mathcal{L}_{\text{kin}} - V(\phi). \quad (2.15)$$

This scalar field, at zero temperatures, has a scalar potential with global minimum giving a non-zero vacuum expectation value $\phi = v$. Since the scalar field is thermally coupled to the other particles in the sector, its potential will gain a temperature dependent contribution from each species i ,

$$V_T^i(\phi) = \frac{T^4}{2\pi} \int_0^\infty dx \cdot x^2 \cdot \text{Log}(1 \pm e^{-\sqrt{x^2 + \left(\frac{m_i(\phi)}{T}\right)^2}}), \quad (2.16)$$

where $m_i(\phi)$ is the modified mass from 1-loop corrections of species i , and \pm whether it's a boson or fermion. Eq. (2.16) can be expanded as a power series in temperature

where the first order correction is of order $\mathcal{O}(T^2)$. As the temperature increases, the scalar potential starts to regain its zero valued expectation value $\phi = 0$. Past some critical temperature T_c the symmetry is then said to have been restored.

The overall shape of the potential dictates the strength of the PT. If the potential happens to have a smooth monotonically decreasing path from the metastable to stable vacua, then statistical fluctuations in the field value are enough to initiate the transition. On the other hand, if it possesses a large potential barrier between the two vacua, the process has to occur by quantum tunnelling through the barrier. The two types of PT's are defined as,

- 1st order phase transition: quantum tunnelling through barrier.
- 2st order phase transition: continuous cross over to minimum.

From our current measurements of the Higgs boson mass and the known particles that it interacts with, it's shown that the EWPT occurs through the smooth cross over of a 2nd order around the scale $v \approx 250$ GeV. The particles of the strong force also undergo a PT due to the scalar quark condensate. Once the condensate picks up a vacuum expectation value at temperatures near the hadronization scale Λ_{QCD} the chiral symmetry is broken, initiating the confinement of quarks and gluons into hadrons. In Section 2.2, sectors of exotic particles which have 1st order PT will be explored. The remainder of this section will focus on the details of the 1st order PT process.

There is no sound more consistent in a grad student's life than the sound of a percolating coffee machine, or the whistle of a tea kettle. Underneath the exterior is a repository of water reaching it's boiling point initiating the transition between the liquid and gas phase. If the grad student were to inspect it they would see tiny bubbles of the new gas phase boiling to the top. These bubbles travelling with the

characteristic speed of the medium, in this case, the sound speed of liquid. As long as the boiling temperature remains constant the liquid will evaporate off completely and the new phase, seeded by these bubbles, remains. Now swap out both the liquid and gas for the metastable and stable phases of some scalar field ϕ , respectively. The bubbles of the new phase now moving at fraction of the speed of light. This simple example is a qualitative representation of what occurs during a cosmological strongly 1st order PT (SFOPT). A scalar field will tunnel through the potential barrier by the process of bubble nucleation. The energy released drives the expansion of the bubbles, which collide and merge, eventually enveloping the whole Universe. The bubble nucleation rate per unit volume at some some temperature is given by,

$$\Gamma(T) = A(T) \exp[-S_E(T)], \quad (2.17)$$

where $A(T)$ is a calculable prefactor. $S_E(T)$ is the Euclidean action of the scalar field

$$S_E(T) = \frac{1}{T} \int d^3x \left[\frac{1}{2} (\nabla\phi)^2 + V(\phi, T) \right]. \quad (2.18)$$

Complete bubble nucleation isn't always realized in the early Universe. The rate of bubble nucleation has to compete with the Hubble expansion of space. On top of that, if an insufficient amount of energy is imparted onto the bubbles, the bubbles can collapse from the imbalance of their surface tension. If any of these conditions is met, the phase transition is unable to percolate the whole Universe. Artefacts of a failed PT can exist in the form of domain walls, monopoles, and cosmic strings.

2.2 Non-Standard Cosmologies

2.2.1 Exotic Phase Transitions

The narrative so far has been of the standard cosmological model. The standard cosmology does account for the observed contribution of gravitational dark matter but still fails to encompass all of the possible influences that non-Standard Model particles may have on the Universe. Many unknowns still exist throughout the history of the Cosmos. We will focus on one of the prime culprits for many of the non-standard influences in the cosmos: SFOPT.

The concept of a PT was explored in the previous section. In the standard cosmology the PTs are all smooth crossovers into their stable configurations. This isn't generally true if the Universe includes additional degrees of freedom in the form of new particles. Consider the EWPT, if an additional scalar similar to the Higgs boson were coupled to the theory the overall scalar potential will change $V(\phi)$. If the new scalar is sufficiently massive a potential barrier will form, changing the PT from a crossover to SFOPT. Therefore modifications of the EWPT can be accomplished by adding additional exotic scalar particles that couple to the EW theory. Things are a bit different in the case of the QCD PT. The addition of exotic scalar particles alone can not change the theory from a crossover to a SFOPT. This is because the scalar field that undergoes the symmetry breaking in QCD is not an independent scalar particle but itself is a condensate of the known quark fields. To change the scalar potential would require changing either the quark masses or the underlying symmetries.

Although the QCD PT is well established a PT from QCD-like theories can have drastically different outcomes. In Chapter 1 a model of Dark QCD was established

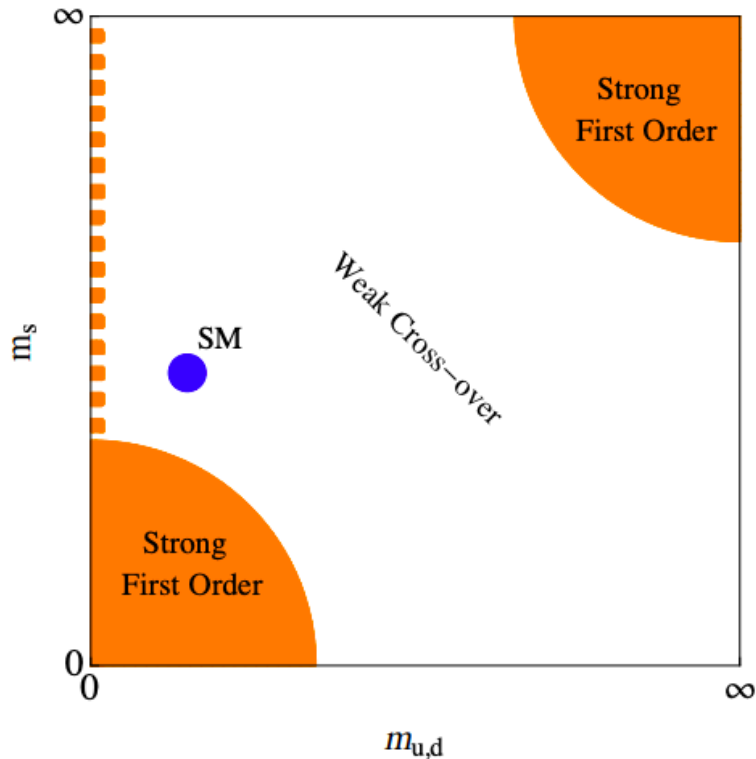


Figure 2.3: A illustration of the Columbia plot [38] from [39], which encompasses the phase diagram of $N_f = 3$ QCD. The mass of the up-type and down-type quarks are assumed to be approximately degenerate. The SM exists in the weak cross-over regime. Two regimes of SFOPT exist corresponding to the restoration of chiral symmetry (bottom left) and pure Yang-Mills symmetries (top right).

where all masses, scales, and degrees of freedom differ from that of the SM. In these QCD-like theories the dynamics are still governed by the $SU(N_d)$ gauge group. N_d is the number of colours in this new sector. For it to be similar to QCD the theory must confine at some scale Λ_d . Otherwise, the remaining parameters of the theory are free ². Within the Standard Model and most with QCD-like theories the masses of the u-type and d-type quarks are almost degenerate due to the approximate isospin symmetry. Near the scale Λ_d only quarks with $m \leq \Lambda_d$ have any effect on the dynamics

²This is not completely true since both the number of flavours and colour dictate whether the theory confines at Λ_d .

of the PT. Considering only the light quarks ($m_d \approx m_s$) a phase diagram can be constructed. Fig. 2.3 is a loose representation of this phase diagram, produced in [39], known as the Columbia plot [38]. We can see that the masses of the light quarks of the SM put the QCD PT within the weak cross over regime, as expected. Even more interestingly is that the phase diagram hosts two antipodal regimes of SFOPT. In one regime the quarks are relatively light. When the quarks become massless the chiral symmetry $SU(N_d)_R \times SU(N_d)_L$ is restored and once spontaneously broken induces the SFOPT. The second regime is reached once the masses become extremely large relative to the scale Λ_d . The heavy quarks are effectively integrated out with only gluons remaining, known as Yang-Mills theory. The symmetry restored in this case is a global Z_3 symmetry. This argument slightly changes when the number of light flavours of quarks is more than three [40]. But to a good approximation these two extremes give us a good representation of the dynamics at critical temperatures $T_c \sim \Lambda_d$

2.2.2 N-Naturalness

N -Naturalness is a theory that assumes the Universe is filled with N non-interacting hidden sectors of particles. One of these sectors hosting all of the Standard Model physics. In the most generic form of the theory these sectors can host any number of novel gauge symmetries with unique particle content. In original scenario these hidden sectors are taken to be N -copies of the Standard Model differing in only the Higgs mass squared m_h^2 . The Higgs mass parameter can take on values ranging from $-\Lambda_H$ and Λ_H , where Λ_H is the scale that cuts off the Higgs quadratic divergence in Eq. (1.25). The expectation is that the Higgs mass will be accidentally tuned to $|m_H^2|_{\min} \sim \Lambda_H/N$ in the SM sector. Each sector is conveniently defined by its vacuum

expectation value, using its relationship to the Higgs mass parameter Eq. (1.13).

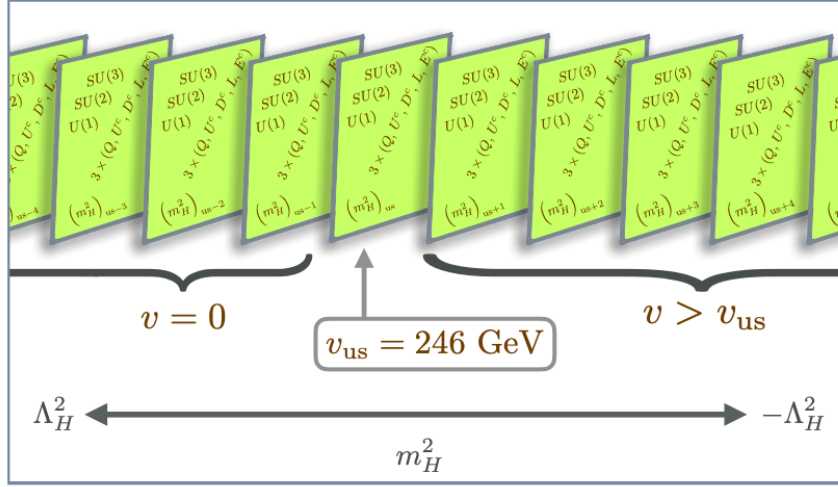


Figure 2.4: A visual representation of the many sectors of N -naturalness.

Fig. 2.4 is a pictorial representation of where we exist in the distribution of N -sectors. Notice that the sector with the smallest non-zero VEV is taken to be our own v_{us} . A negative VEV is not physical so every sector with $(m_H^2)_i > (m_H^2)_{\text{us}}$ becomes zero. So far we have not imposed any constraints on how these sectors are distributed. Technically, these sectors can be distributed in any fashion that is consistent with experimental constraint, but the more complex the distribution the less natural the theory is. Generic distributions of multiple hidden sectors will be discussed in Chapter 4. Assuming the sectors are uniformly distributed, the mass parameter for the i^{th} sector becomes,

$$(m_H^2)_i = -\frac{\Lambda_H^2}{N}(2i + r), \quad (2.19)$$

where we live in sector $i = 0$, and r is a parameter that tunes the spacing between sectors. Having $r = 1$ equates to a uniform splitting.

N -Naturalness, as the name implies, provides natural solutions to the hierarchy

problem discussed in Chapter 1. The hierarchy between the Λ_H^2 and the scale of gravity Λ_G is reduced by $\Lambda_G \sim M_{\text{pl}}/N$. To solve the full hierarchy problem we need the two scales to be around the same order $\Lambda_H^2 \sim \Lambda_G$, resulting in a total of $N \sim 10^{16}$ sectors. If instead there exists a higher theory at a lower scale $\Lambda_H \sim 10$ TeV then the number of sectors allowed is $N \sim 10^4$. Implying a solution to the little hierarchy problem $\Lambda \sim 10$ TeV. Both these solutions assume that no other implicit degrees of freedom in the theory affect Λ_G . The N sectors can be partitioned up into two categories, sectors with $(m_H^2)_i > 0$ and $(m_H^2)_i < 0$.

Sectors with $(m_H^2)_i < 0$ exhibit the same dynamics as our own but with a non-zero vev,

$$v_i \approx v_{\text{us}} \sqrt{i}. \quad (2.20)$$

where the uniform splitting $r = 1$ was taken. Meaning that sectors further from our own have large particle masses that scale with v_i . The EW portion of the sector will undergoes spontaneous symmetry breaking initiated by the vev of the higgs. Although for sectors with quark masses sufficiently larger than the QCD scale Λ_{QCD} , the QCD symmetry becomes that of the pure Yang-Mills theory. From Section 2.1.2 we know that the breaking of these pure QCD symmetries happens alongside a SFOPT.

In the case of sectors with $(m_H^2)_i > 0$, the vev is $v_i = 0$. Therefore the Higgs no longer undergoes the usual symmetry breaking. The EW symmetry is instead broken by radiative corrections from the QCD PT, lowering the temperature at which it's broken. The consequence is that these scenarios have a relatively light spectrum of particles. These light fermion masses are generated by higher order processes, with the Higgs integrated out, given by,

$$m_f \sim y_t y_f \frac{\Lambda_{\text{QCD}}^3}{(m_H^2)_i} \lesssim 100\text{eV}, \quad (2.21)$$

where y_t and y_f are the Yukawa couplings of the top quark and fermions, respectively. Again, the scenario of relatively massless quarks was previously treated. As the quarks become small the chiral symmetry is restored. Once the symmetry becomes broken a SFOPT is initiated. The interplay between the SFOPT from multiple different sectors will be the topic of Chapter 4.

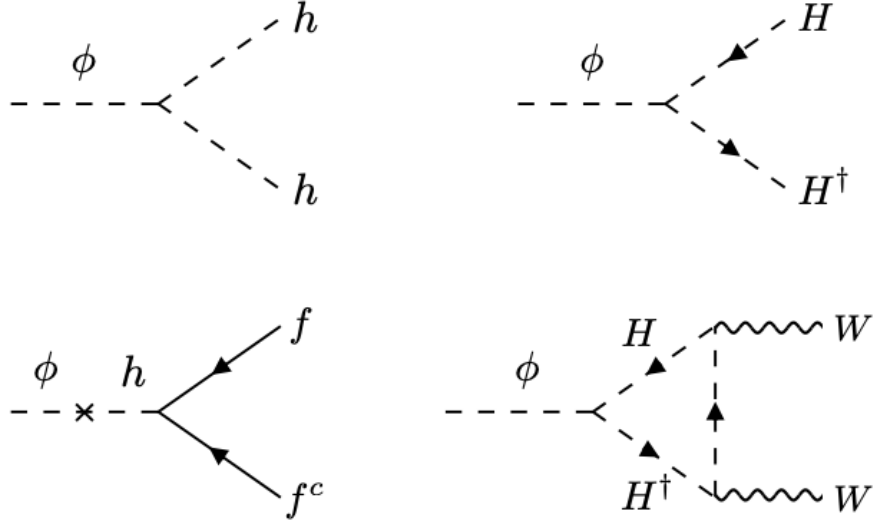


Figure 2.5: The various decay channels of the reheaton with the EW sector particles. The left (right) column is for $v \neq 0$ ($v = 0$). The top (bottom) row is for m_ϕ greater (lighter) than the m_H .

If we naively take the sectors to take up equal fractions of the Universe’s energy density, and thus equal temperatures, then we run into the problem of overheating the Universe. Each sector adds additional relativistic degrees of freedom. Eq. (2.13) shows how the components of radiation energy density are related to N_{eff} . Having sectors with equal temperatures would result in adding $\Delta N_{eff} \approx N$, exceeding the allowable constraints. Therefore the sectors must be reheated in such a way that our sector is predominately heated. This is accomplished through the proposed “reheaton” field in a post-inflationary era of the Universe. The reheaton field is a scalar field which

couples universally to each sector's Higgs through,

$$\mathcal{L}_\phi = -a\phi \sum_i |H_i|^2 - \frac{1}{2}m_\phi^2\phi^2. \quad (2.22)$$

For the theory to be consistent the prefactor must scale as $a \sim 1/N$. It's not obvious from Eq. (2.22) that the reheaton preferentially decays into our sector. It becomes more apparent once the Higgs is integrated out which requires the reheaton to be much lighter, comparatively. Integrating out the Higgs depends on the vevs in the sector, leading to the following lagrangians,

$$\begin{aligned} \mathcal{L}_\phi^{v \neq 0} &= \mathcal{C}_1 a y_q \frac{y}{m_\phi^2} \phi q q^c, \\ \mathcal{L}_\phi^{v=0} &= \mathcal{C}_2 a \frac{g^2}{16\pi^2} \frac{1}{m_H^2} \phi W_{\mu\nu} W^{\mu\nu}, \end{aligned} \quad (2.23)$$

where $W_{\mu\nu}$ is the EW SU(2) field strength, g is the weak coupling, and \mathcal{C}_j are numerical prefactors. Solving for the reheaton decay widths give, $\Gamma_{(m_H^2)_i < 0} \sim 1/m_{H_i}^2$ and $\Gamma_{(m_H^2)_i > 0} \sim 1/m_{H_i}^4$, for sectors with and without EW symmetry breaking. The decay channel diagrams are presented in Fig. 2.5. There is also a $\phi \rightarrow \gamma\gamma$ diagram that is left out because it contributes a negligible scaling behaviour. It's now obvious from the decay widths that the reheaton populates the SM sector with the most energy density. It is noteworthy to point out a possible communication channel, induced by ϕ , between each sector in the quintic term $\kappa |H_i|^2 |H_j|^2$. As long as the coefficient scales as $\kappa \sim 1/N$ the sectors are sufficiently disconnected.

The ratio of decay widths between the i^{th} sector is proportional to ratio of energy densities of the sectors,

$$\frac{\Gamma_i}{\Gamma_{us}} \propto \left(\frac{\rho_i}{\rho_{us}} \right)^{1/4}. \quad (2.24)$$

Fig. 2.6 shows the profile of reheating each sector as a fraction of our sector for a $m_\phi = 100$ GeV. The dotted lines represent the expected scaling while the solid lines are of a full numerical calculation. In the $(m_H^2)_i > 0$ sectors, the numerical calculation follows the expected scaling and blows up near sector one. Sectors with $(m_H^2)_i < 0$ dramatically divert from the expected scalings. This is due to the sector's quark masses surpassing the Λ_{QCD} threshold. The implications of reheating multiple sectors will be explored In Chapter 4.

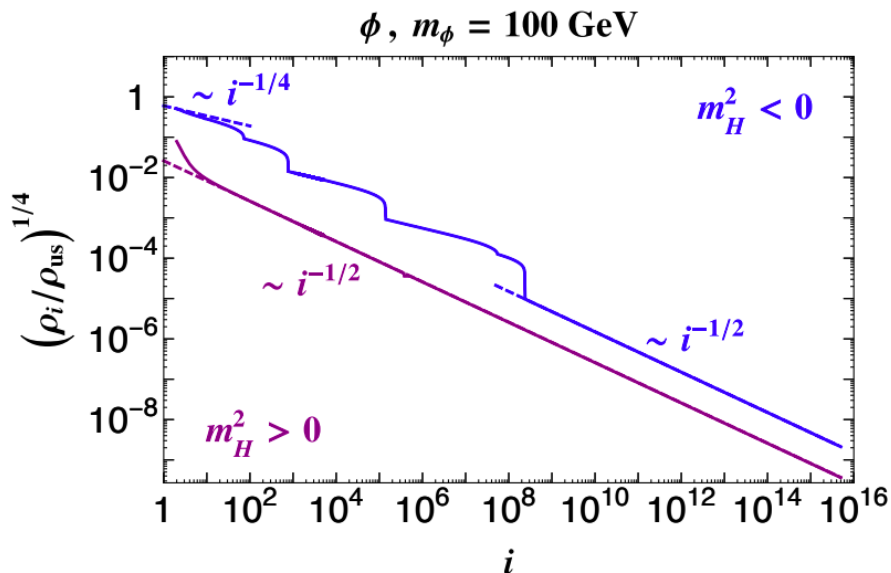


Figure 2.6: The ratio of energy densities deposited in the i^{th} sector as a function of sector number and the energy density in our sector from [41]. The scalar reheaton is taken to have mass of $m_\phi = 100$ GeV. Dotted lines represent the expected scaling of the sectors. The solid lines our numerical results using Eq. (2.23).

2.3 Gravitational Waves

2.3.1 Linearized Einstein Equation

Before the 21st century our only means of measuring the astrophysical objects in our night sky, far from our small position in the Universe, has been by using electromag-

netic radiation (ER) of one form or another. Methods like photometry (broadband light) and spectroscopy (narrowband light) have been integral in making significant statements about our Universe thus far. Although highly successful in propelling the field of astronomy into a measurable science, the light we measure in our local vicinity is riddled with systematic noise. Whether the light emitted stems from the surface of a nearby star or from the last scattering horizon, substantial distortion is done to the signal as it travels from its source to our detectors. Sky based observatories, which help to avoid the effects of atmospheric attenuation, are still subject to inter and extragalactic foreground effects. These effects are only understood through loose parametric modelling of background data. Even if astronomers could account for these astrophysical contaminations, their measurements are still limited to distances up to the last scattering of light (recombination). This chapter will follow the discussions in [4].

In 2015 the LIGO experiment discovered the first significant direct evidence of a new mode for humanity to measure the night sky [42]. Gravitational waves (GW), first postulated by Einstein a century ago, are wave phenomenon in which the medium of oscillation is space-time itself. Unlike electromagnetic radiation, which relies on the electromagnetic field as its medium, gravitational waves can propagate uninhibited by other sources of electromagnetic contaminations. The gravitational waves detected to the current day are sourced from highly energetic gravitational systems such as black hole and neutron star mergers. As GW interferometers advance, astronomers will be able to probe larger scales of the Universe that would involve cataclysmic gravitational effects, including the big bang.

The theory of GWs is, in essence, a theory concerning local disturbances in the geometry of space-time and therefore relies on general relativity. Similar to solving

the equations of an evolving FLRW Universe, the Einstein equation relates how the local curvature of space-time is influenced by mass-energy. The compact tensor form of the Einstein equation is,

$$G_{\mu\nu} = 8\pi T_{\mu\nu}, \quad (2.25)$$

where the Einstein tensor $G_{\mu\nu}$ is a non-linear function of the metric $g_{\mu\nu}$, and $T_{\mu\nu}$ is the energy-stress tensor. $G_{\mu\nu}$ is built up from theory's metric. In case of the GW, the metric is merely a small perturbation from flat space $\eta_{\mu\nu} = \text{diag}(-1, 1, 1, 1)$ represented as,

$$g_{\mu\nu} = \eta_{\mu\nu} + h_{\mu\nu}(x). \quad (2.26)$$

The metric perturbations $h_{\mu\nu}$ are extremely small quantities such that $h_{\mu\nu} \ll 1$. Solutions to Eq. (2.25) are found using the metric perturbation and a non-zero energy-momentum tensor representing the source of the disturbance. The Minkowski metric is ignored as it is not a function of the coordinates. Propagation of GW in a vacuum are solutions with a zero source term.

Solving the now linearized Einstein equation requires solving 10 non-linear differential equations in $h_{\mu\nu}$. Similar to the wave solutions of the Maxwell equations, gauge conditions are imposed on the metric perturbation which add four new constraints to the 10 equations. The Lorentz gauge is commonly used for GW solutions and takes the form of $\partial_\mu \bar{h}^{\mu\nu} = 0$. Here, $\bar{h}^{\mu\nu}$ is a convenient form of the metric perturbation³. The linearized Einstein equation takes the form of,

$$\square \bar{h}_{\mu\nu} = -16\pi T_{\mu\nu} \quad (2.27)$$

³Keeping in mind that index raising is accomplished through contractions with $\eta_{\mu\nu}$ not $g_{\mu,\nu}$

It is easy to spot the similarities between Eq. (2.27) and a sourced wave equation commonly seen throughout EM. In this case, the wave equations are of rank-2 tensor quantities. It may not be obvious because of the use of natural units but the GW propagate at the speed of light. Otherwise, another velocity scale would have appeared in Eq. (2.27). General solutions of the wave equations understood in terms of causal propagation,

$$\bar{h}^{\mu\nu}(t, \hat{x}) = 4 \int d^3x' \frac{[T^{\mu\nu}(t', \hat{x}')]_{ret}}{|\hat{x} - \hat{x}'|}. \quad (2.28)$$

Keeping in mind that a casual observer evaluates $[T^{\mu\nu}(t', \hat{x}')]_{ret}$ at the retarded time. Once the source's stress-energy is explicitly defined the propagating modes of $h_{\mu,\nu}$ can be evaluated. The topic of gravitational sources is a richly studied field and outside a few examples surpasses the scope of this thesis. Two notable cases are of axially symmetric and rotating sources, or spherically symmetric and expanding sources. In both these systems solving Eq. (2.28) leads to zero GW emission. Therefore GW are more likely to be sourced from complex dynamical systems involving binary influence, mergers, and phase transitions.

In free space $T_{\mu\nu} = 0$ and Eq. (2.27) reduces to the vacuum wave equations. The solutions become plane waves propagating along some direction \hat{k} . Without loss of generality, we consider propagation along the z -coordinate. Using the above choice of gauge condition, which also assumes a traceless metric, the plane wave solutions are given by,

$$h_{\mu\nu} = \begin{pmatrix} 0 & 0 & 0 & 0 \\ 0 & a \cdot f_+(z-t) & b \cdot f_\times(z-t) & 0 \\ 0 & b \cdot f_\times(z-t) & -a \cdot f_+(z-t) & 0 \\ 0 & 0 & 0 & 0 \end{pmatrix}, \quad (2.29)$$

where $f_{+/\times}(z-t)$ is a generic plane wave with angular frequency ω for polarization modes $+$ and \times . Since the non-zero elements are only in the x-y plane, any point masses along this plane will stretch and contract with amplitudes a and b . This is how we define the polarizations of GW along a set of coordinates. As one axis contracts the other stretches, producing a characteristic pattern that gravitational interferometers can take advantage of.

2.3.2 Stochastic Gravitational Waves

Eq. (2.28) tells us that GW can be produced through exciting new phenomena like merging of two neutron stars. These types of binary merging events produce GW with frequencies around the detectability of modern interferometers. One of the advantages in measuring these merger events is in knowing their characteristic *chirp* spectrum. Merger events can be simulated to a high accuracy from stellar astrophysical models. Gravitational interferometers will employ these models as templates to fit each event's time series, greatly increasing the signal-to-noise ratio. The remainder of this section will focus on gravitational waves from the early universe. Specifically, events that form a stochastic gravitational background. Similar to the cosmic microwave background, this GW background is formed from many individual GW processes at a much earlier time in the Universe. Instead of consisting of single *chirp* spectrum the GW background has a stochastic power law spectrum built by the convolution of the many random processes at that time t_* .

Stochastic GW backgrounds are conjectured to be produced at volatile times of the cosmic history, including the big bang and inflation. The GW background can be initiated by SFOPTs. Going back to the tea kettle analogy, the SFOPT are manifest through many percolating bubbles of the new stable phase. We can hear when the kettle is boiling because of the collisions of the bubbles imparts energy to source sound waves into the surrounding medium. This analogy is similar to SFOPTs of an earlier Universe. When two bubbles of the new phase collide they exchange a portion of their energy in sourcing gravitational perturbations in the surrounding space-time. These perturbations becoming GW that traverse space at the speed of light. If the entire Universe is percolating, many bubbles are formed and collide, producing a stochastic GW background. Eventually this background will free stream into our current era as a lower energetic version of itself, similar to the CMB today. The dimensionless energy density it had at the time of production is given by,

$$\Omega_{\text{GW}} = \frac{\rho_{\text{GW}}}{\rho_c}. \quad (2.30)$$

Gravitational waves produced at a temperature T_* will propagate undisturbed in the expanding Universe. Their frequency f and their energy density Ω_{GW} will decrease following Eq. (3.16) as a^{-1} and a^{-4} , respectively. The scale factor at production a_* and today a_0 are related by the exact form of Eq. (2.12),

$$\frac{a_*}{a_0} = \left(\frac{g_{0s}}{g_{*s}} \right)^{1/3} \frac{T_0}{T_*}, \quad (2.31)$$

where $g_{0,s}$ and $g_{*,s}$ are the entropic degrees of freedom of today and production, respectively. T_0 is the temperature of the CMB today of 2.348×10^{-13} GeV. Future GW observatories will measure both the frequency today f_0 and the fraction of energy

density today $\Omega_{\text{GW},0}$. Following from eq. Eq. (2.2) the frequency at production f_* will redshift into,

$$f_0 = \left(\frac{a_*}{a_0}\right) f_* = \beta(T_*) f_*, \quad (2.32)$$

where $\beta(T_*)$ is only function of the temperature at production. Energy density fractions evolve in both the energy density ρ_{GW} and the critical energy density ρ_c . Evolving both gives the total fraction of GW energy density today as,

$$\Omega_{\text{GW},0} = \left(\frac{a_*}{a_0}\right)^4 \left(\frac{H_*}{H_0}\right)^2 \Omega_{*\text{GW}} = \mathcal{A} \Omega_{*\text{GW}}, \quad (2.33)$$

where \mathcal{A} is a constant⁴ and the factor H_*/H_0 comes from the ratio of the critical densities of today and at production. H_0 is the Hubble rate measured today. H_* is the Hubble rate at production and is assumed to be during a radiation dominated era such that it scales as $H \propto T^2$. The take away here is that the strength of the GW background today is not a function of the production temperature, only its frequency is. In Chapter 4 it will be shown how the shifting of GW frequencies, but not energy densities, for more than one sector undergoing a SF OPT can produce interesting and novel signals.

⁴Up to a factor of g_{*s} .

Chapter 3

Data, Simulations, and Reconstructions

*“There are three kinds of lies: lies, damned
lies, and statistics.”*

— *Mark Twain*

3.1 Collider Physics

The particle colliding experiments running at the LHC are all subject to the same initial conditions: collisions of a proton-proton beam at some energy E_{cm} . Having the capability of steering and colliding highly energetic particles is no easy feat, accomplished by the culmination of decades of research and development. The accelerator physics challenges would never have been met if it weren't for discoveries within tangential fields such as radio-frequency superconductivity, cryogenics, and engineering. These areas alone have advanced at such significant rates due to the particle physics agenda continually pushing the technical boundaries. The remainder of this section will not focus on the difficult, but crucial, accelerator physics and engineering, but

instead on the easier topic — the actual particle physics.

In essence, particle colliding experiments merely count the number of events, inclusively or exclusively, over the duration of the experimental run. This can be reduced to the holy grail equation in particle physics [5],

$$N = \sigma \mathcal{L} \epsilon, \tag{3.1}$$

where N is the number of events, $\mathcal{L} = \int (d\mathcal{L}/dt)dt$ is the integrated luminosity of the proton beam over the duration of the run, the cross section σ is a measure of the probability of a certain event to occur, and ϵ is the efficiency of detecting an event. The luminosity is approximately constant and precisely monitored throughout the experiment. The efficiencies are related to effects not captured by the cross section that might change how events are recorded. Prime examples are inefficiencies in detector response, and acceptance filters known as triggers. Triggers and other detector limitations will be the prime focus of Chapter 5. The luminosity can be treated as an initial condition while the efficiencies are related only to the detection process. This leaves the cross section to contain all of the interesting particle physics. Meaning, the processes that occur during the hard collisions are encoded into the measured cross sections. These cross sections are dependent on the variables measured at these experiments, presented in the following section.

Two proton beams, each with equal energy E , collide at one of the experiment's interaction points (IP). The proton's momenta are aligned with the direction of the z -axis. These energies are taken to be much larger than the mass of the proton. For example, currently the LHC is running at $E \sim 6.5$ TeV [43], where as, the proton has

mass $m_p \sim 1$ GeV. The two momenta can then be written as,

$$P_1^\mu = (E, 0, 0, E), \quad P_2^\mu = (E, 0, 0, -E) \quad (3.2)$$

The center-of-mass (CM) energy being $E_{cm} = \sqrt{s} = 2E$, here we use the Mandelstam variable $s = (P_1^\mu + P_2^\mu)^2$.

At energies close to the mass of protons, the protons can be thought of as fundamental, in the sense that collisions are elastic. Instead, the energies at the LHC are so high that the fundamental colliding objects are the partons inside the proton (gluons, quarks). These collisions are inelastic in nature, where the interior objects of the proton are probed. The hard collisions in question are thus of the proton's partons colliding. The partons then carry a fraction of the momentum of their mother protons,

$$p_1^\mu = x_1 P_1^\mu, \quad p_2^\mu = x_2 P_2^\mu, \quad (3.3)$$

where x_i is the momentum fraction of parton species i . The distribution of x_i for a proton is known as the proton distribution function (PDF) $f_p(x_i, \eta)$ and is dependent on the energy scale η . The PDF of the proton has been well studied through data-driven methods at fixed target experiments.

The variables of interest are now the momentums of the partons in the CM frame, p_i . In the case of collisions along the beam z -axis, it's convenient to form a basis of variables that are independent of successive boosts along the z -axis. This allows experiments to relate measurements, such as the cross section, between the lab frame and the CM frame with ease. Therefore, assuming a general parton momentum $p = (E, p_x, p_y, p_z)$ and boosting it in the z direction with boost factor β gives,

$$\begin{aligned}
E' &= E \cosh(\beta) + p_z \sinh(\beta) \\
p'_x &= p_x \\
p'_y &= p_y \\
p'_z &= p_z \cosh(\beta) + E \sinh(\beta).
\end{aligned}
\tag{3.4}$$

Since p_x and p_y are invariant under successive Lorentz boosts along z , the transverse momentum p_T is commonly used, defined as,

$$p_T \equiv (p_x, p_y). \tag{3.5}$$

Similarly, the azimuthal angle ϕ around the z -axis is boost invariant,

$$\phi = \tan^{-1} \frac{p_x}{p_y} \tag{3.6}$$

The final boost invariant variable to complete our basis is the rapidity y . Most of the particles produced in a collision are effectively massless when compared to the high energies of the hard interaction. Therefore, we consider the pseudorapidity η , which is the rapidity in the massless limit. In doing so, we can relate the pseudorapidity to the polar angle θ along z ,

$$\eta = \ln \tan^{-1} \frac{\theta}{2}. \tag{3.7}$$

When the masses of the resulting particles are sufficiently big, the rapidity must be used instead. This is the case for studies of the heavy massive bosons Z, W . Otherwise, the new basis (p_T, ϕ, η) can be easily mapped to the geometric coordinates of the detectors. In Fig. 3.1 the coordinate frame overlays the ATLAS detector

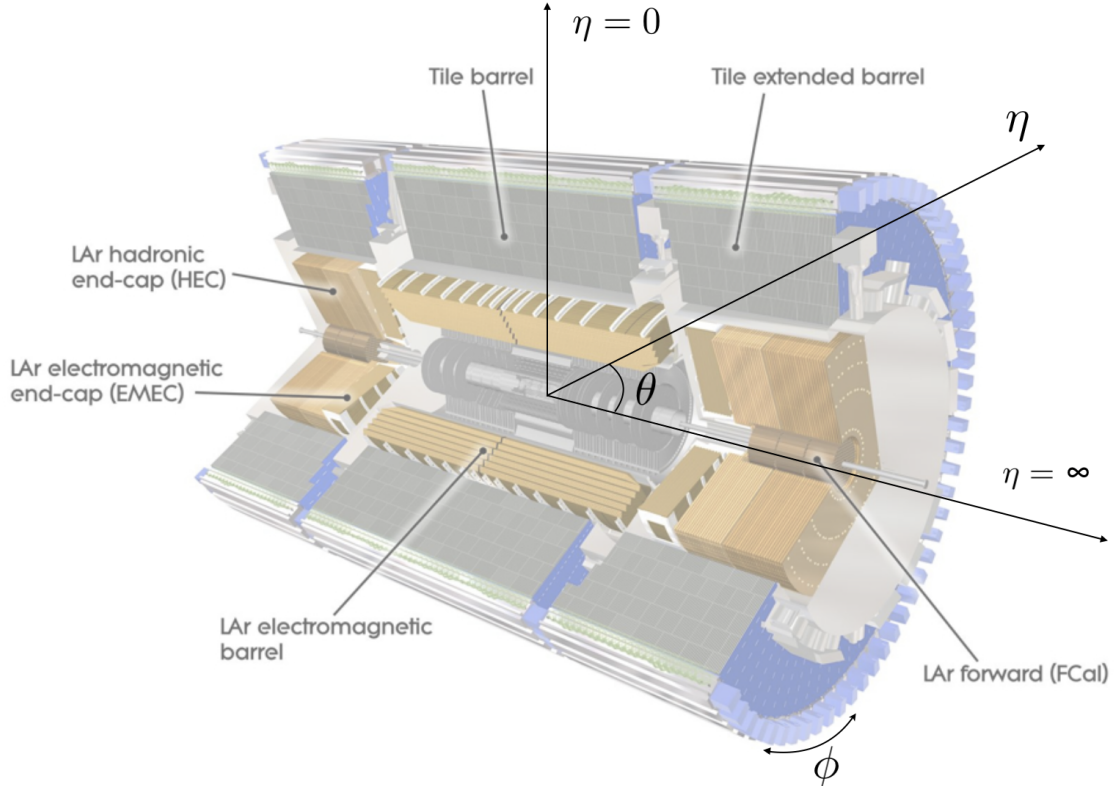


Figure 3.1: The boost invariant quantities η and ϕ mapped onto the ATLAS experiments coordinate system. The pseudorapidity η is a function of the polar angle θ . The ATLAS detector comprises of a cylindrical geometry to take advantage of this coordinate frame [44].

packages. It is easy to see that their geometry was designed to take full advantage of these boost invariant coordinates.

The last boost invariant variable to consider is a distance analogue. It's obvious that the euclidean distance between objects in the lab frame differs from that of the CM frame. Instead a useful invariant quantity is,

$$R_{ij} = \sqrt{(\phi_i - \phi_j)^2 + (\eta_i - \eta_j)^2}. \quad (3.8)$$

This concept of a distance in (ϕ, η) will become important in the discussion of reconstructed jets of particles in Section 3.3.

3.2 Monte Carlo Showering Simulations

3.2.1 Sudakov Probability and Parton splitting

In Section 1.2.4 the theory of the strong force was introduced within the framework of QCD. One of the substantial differences between QCD compared to the EW theory is that, at some scale Λ_{QCD} , the coupling becomes large enough to make the theory non-perturbative. This mechanism is what allows for the strong binding of quarks and gluons into the colour singlet states: hadrons. This was previously discussed in the context of a PT, where the theories fundamental constituents changed between the quark phase and the hadron phase. Without it, the Universe would be devoid of the structure we see today, leaving the quarks and gluons to roam freely within it. Although necessary for life, the non-perturbative nature of QCD makes it tremendously difficult to calculate the dynamical outcomes of particles charged under its symmetry group. Only soft and collinear approximations dominate our understanding of how partons evolve from some small scale to the limits of the hadronization scale Λ_{QCD} . This evolution producing the unique parton showers of Section 1.2.4. In this section, current simulation methods of these parton showers will be discussed. The following section will discuss how these simulations deal with the non-perturbative hadronization stage using data-driven models.

The study of parton showers is a rich and complicated field. Our current models of parton showers in the SM QCD theory has been generalized and adapted for many different versions of QCD-like theories such as in the Hidden Valley framework of Section 1.3.2. A detailed discussion of parton splitting functions and collinear-soft evolution can be found in refs [45]. The focus will therefore be on a general qualitative view on how certain simulation tools deal with coloured partons in the

hard interactions. Specifically, we can generate a probabilistic evolution of the partons from scales μ_0 to $\mu_0 + d\mu$ using Monte Carlo¹ methods.

Monte Carlo methods allow us to run many instances of an event, randomly sampled from some distribution. In the case of parton showers, we sample from the probability distribution of the parton to radiate additional partons. As a toy model, we can consider the decay of some particle with decay width Γ . The probability of the particle staying intact, therefore stable, between time $t' = 0$ and time $t' = t$ is given by,

$$\mathcal{P}_{\text{stable}}(t, 0) = \exp\left[-\int_0^t dt' \Gamma(t')\right]. \quad (3.9)$$

Keeping in mind that Γ is generally a function of the evolution parameter t . The probability of the particle decaying within the same time interval is therefore,

$$\mathcal{P}_{\text{decay}}(t, 0) = 1 - \mathcal{P}_{\text{stable}}(t, 0) = 1 - \exp\left[-\int_0^t dt' \Gamma(t')\right]. \quad (3.10)$$

Ideally we are looking for the probability of the rate of decay at each instance of the evolution parameter. Differentiating the decay probability gives the probability density of the particle to decay at exactly time t ,

$$\frac{d\mathcal{P}_{\text{decay}}(t, 0)}{dt} = \Gamma(t) \cdot \mathcal{P}_{\text{stable}}(t, 0). \quad (3.11)$$

Therefore the instantaneous rate of decay is proportional to the probability of not decaying the particle within a defined time interval.

To relate this to parton showering, we just need the probability distribution of

¹Technically, modern simulation packages use Markov Chain Monte Carlo methods, which take advantage of the stochastic nature of parton showers to greatly reduce the random sampling of the high dimensional parameter space.

the parton a not splitting into partons b, c ². This distribution is well-known in QCD as the Sudakov form factor,

$$S_{a \rightarrow bc}(T, t) = \exp \left[- \int_t^T \frac{dt'}{t'} \int_{z_-}^{z_+} dz \int_0^{2\pi} \frac{d\phi}{2\pi} \frac{\alpha(t', z)}{\pi} \Gamma_{a \rightarrow bc} \right], \quad (3.12)$$

where the probability is now between the scales (t, T) , z is the light-cone momentum that ensures 4-momentum conservation, ϕ is the azimuth kinematical variable, and α is the strong coupling constant. The kernel $\Gamma_{a \rightarrow bc}$ is no longer the decay width, but now the splitting (function) probability calculated in QCD. $S_{a \rightarrow bc}(T, t)$ satisfies the conditions for a probability distribution as it is bounded between $(0, 1)$. Eq. (3.12) becomes the master formula for sampling the evolution of a given parton, where the probability of branching is randomly sampled in binned steps of the evolution parameter $t, t + dt$. The form of the splitting kernel produces large logarithms between the two evolving scales. More specifically, these logarithms are enhanced in the collinear and soft radiation limit, unique to only particles charged under the strong force.

There are a few sophisticated implementations of parton showering models, most notable is the PYTHIA implementation [46]. Fortunately, PYTHIA hosts parton showering schemes within the hidden valley framework [47]. This will be the main tool used in Chapters 5 and 5 for dark showering simulations.

3.2.2 Hadronization and Tuning

The parton showering process cuts off at a scale around Λ_{QCD} . This is when the coupling becomes large enough to bind the quarks and gluons into colour singlet configurations in the form of hadrons, known as hadronization. With a large coupling the theory becomes non-perturbative, making exact calculations intractable under the

²if the parton is just radiating a single new parton, this still holds as b will just become the updated version of a

current framework. When simulating the fragmentation of partons into hadrons, data-driven methods are used instead. A theoretically motivated model of fragmentation is tuned to collider data. There are currently two well used fragmentation models, the clustering model [48] and the Lund string fragmentation model [49,50]. The Lund string fragmentation model will be the focus of this section as it's the model used within the PYTHIA.

The Lund string model was developed in the 1980s. It was motivated by spectroscopic observations of various hadronic species. Experiments showed that the potential, as a function of distance r , had both the usual Columb term and a new linear term,

$$V_{\text{QCD}}(r) \approx -\frac{4}{3} \frac{\alpha_s}{r} + \kappa r. \quad (3.13)$$

In the case of a $q\bar{q}$ pair, the potential between the two quarks would increase with some strength κ . Leading to the concept of confinement between coloured particles. Lattice calculations confirm the potential structure and constrain the coupling strength to be $\kappa \approx 1 \text{ GeV/fm}$ [51].

In the Lund string model, the field lines of the potential between two quarks is conceptually thought of as a string. This string between both particles sets the dynamics as the pair moves in 1+1 dimensional space-time. Once the string is maximally extended, set by κ , the string breaks. Since free quarks are not permitted in nature, quarks produced from the string break will quickly form a new quark-antiquark string. This process will continue until producing different flavours of light mesons, which we refer to as the hadronization process. The resulting hadrons are produced with momentum fractions z distributed by,

$$f(z) = N \frac{(1-z)^a}{z} \exp\left(\frac{bm_T^2}{z}\right), \quad (3.14)$$

where a and b are tuned parameters, $M_T = \sqrt{m^2 + p_T^2}$ is the transverse mass, and N is the normalization. After the hadrons tunnel out of the potential they are considered free. These free hadrons will either become stable, relative to detector time scales, or decay into lower mass SM particles. Parameters a and b are tuned by these decay rate observations from collider physics experiments.

3.2.3 Dark Showering Uncertainties

The previous sections focused on showering and hadronization within the SM QCD. These arguments change when we instead consider QCD-like theories, such as in the hidden valley (HV) framework. In Chapter 1, we saw how QCD-like theories can produce confining sectors, such as in dark QCD, for a variety of particle content and gauge groups. Consider for an example a hidden sector with a general $SU(N)$ gauge group where the number flavours of light quarks is not too large such that its beta function runs negatively. We can then ask whether the parton splitting process in the new sector deviates from that of the SM expectation. If so, are the Monte-Carlo methods previously established still valid? Assuming that the Sudakov form factor is the theoretical basis of our Monte-Carlo, implies that our radiation (split partons) is soft and collinearly dominated. Meaning, that as long as the dynamics of our sector preferentially radiate partons at small angles, then the sampling of the Sudakov form factor would give consistent results³. If the theory priors include large emission angles, the predictions becomes less and less consistent as the average emission angle increases. Theoretically consistent models do exist when the emission approaches the isotropic radiation regime, as seen in [52]. All dark showering models considered will assume approximate soft and collinear emission for the remainder of

³With small corrections to the overall coupling constant, number of colours, and flavours in the prefactor.

the thesis.

Given that our model’s dynamics implies consistent parton showering, then the largest uncertainties stem from the dark hadronization schemes. As mentioned previously, the hadronization parameters are tuned empirically, using existing measurements at collider experiments. Therefore, we are unable to validate the hadronization scheme model parameters for QCD-like models. Instead, two approaches are taken; first, the model parameters are motivated by comparing the new sectors particle spectrum to that of the SM QCD sectors; second, first-order simulations of the theory are conducted using computational lattice techniques. The latter case will inevitably converge towards the theory’s correct parameters. The difficulty in lattice simulations is on timescale of the computation. Because of its resource intensive nature, only a few lattice studies exist that precisely estimate the a dark QCD-like sector’s hadron spectrum. Specifically, for models with an $SU(2)$ gauge group. The studies in Chapter 5 will focus on dark QCD models with $SU(3)$, so instead the former approach is taken. The HV module in PYTHIA allows for a simplified hadron sector with SM QCD motivated hadronization parameters. This introduces a large source of error in the calculations of hadron multiplicities and momentum spectra [53]. With that said, the novel signature spaces of these dark confining sectors is still properly represented by these showering implementations.

3.3 Jet Reconstructions

Now that we understand the detailed evolution of quarks and gluons from the hard interaction to hadronization, we can discuss the different types of observables experimentalists expect to measure at colliding experiments. QCD showering will produce collimated sprays of energetic partons close to the original direction of the mother par-

ton's momentum. This is a consequence of the collinear enhancement from the large logs in Eq. (3.12). The resulting conglomeration of collinear partons is referred to as a jet. Defining a jet must be done consistently at multiple levels of a jets' evolution. Meaning, the characteristics of a jet must be similar at the parton level, the hadron level, and the detector level. Here the detector level means the energy deposits that are associated with the visibly decayed products of the jet. Jet algorithms are used as methods of quantifying a jet at these various levels of granularity. These algorithms also circumvent any modifications done by higher order corrections of the theory. In the case of QCD, the higher order corrections will introduce radiation in both the collinear and soft regime. A jet algorithm that is insensitive to these modifications is said to be infrared-safe.

There are a few families of algorithms which solve the issue of infrared-safe jet definitions. They are usually split up into two categories; cone algorithms [54] and k_T -algorithms [55,56]. We will focus on the latter and its variants, as it is used extensively at the LHC experiments. Unlike the cone algorithms, which cluster objects within a predefined cone, the k_T -algorithms cluster objects by using a distance metric. The general distance measure in momentum space for objects (i, j) is defined as,

$$\begin{aligned}
 d_{iB} &= (p_{Ti})^{2p} \\
 d_{ij} &= \min[(p_{Ti})^{2r}, (p_{Tj})^{2p}] \frac{R_{ij}}{R}
 \end{aligned}
 \tag{3.15}$$

where p_T is the transverse momentum defined in Eq. (3.5), R_{ij} is the distance measure in (η, ϕ) defined in Eq. (3.8), and R is a predetermined jet cone radius. The procedure is to iteratively pair up objects with the smallest distances, with respect to the beam d_{iB} or with each other d_{ij} . Recursively, new objects are made from the previous step. It continues until the distances between each new object, including the beam, are

larger than some chosen threshold, which is related to the resolution of the transverse momentum of two isolated jets. The k_T -algorithms can be subdivided into different forms depending on the values of the parameter p .

$$k_T = \begin{cases} k_T, & p = 1 \\ \text{Cambridge-Achen}, & p = 0 \\ \text{Anti-}k_T, & p = -1 \end{cases} \quad (3.16)$$

In the case of $p = 0$, the distance measure weights the relative strength of the p_T . This can become a problem when comparing initial state radiation with final state radiation, both of which carry significantly different p_T patterns. On the other hand, Cambridge-Achen (CA) is independent of p_T and therefore insensitive to the differences in initial and final state radiation. A disadvantage with using CA is that it produces irregular jet shapes, since it uses only the relative distances in the (η, ϕ) plane to distinguish objects. The Anti- k_T method makes a compromise between the two other forms, providing reliable jet shapes that are consistent for various products of the hard interaction.

ATLAS and CMS, both use the Anti- k_T as their jet clustering algorithm of choice. Although both use different jet cone radius; ATLAS using 0.4 on average and CMS using 0.5. What they do agree on is a get radius for 'fat jets' of $R = 1.0$. The term fat jets is used for topologies of jets that host two or more partons [57]. This can arise from highly boosted heavy objects, such as the Higgs and W, whose decay products are approximately collinear to each other.

3.4 Statistical Tests & Machine Learning

Even with the most advanced experimental program, actual discoveries are only accomplished through rigorous understanding of the resulting data. Proper statistical inference allows the analyst to make sense of the data, creating a narrative which eventually answers questions like, “Given that the experiment measured two reconstructed jets with $p_T > 500\text{GeV}$, can we claim the discovery of a new particle?”. Monumental measurements like that of the the W mass and the discovery of the Higgs boson are only publicly announced after a high level of belief is reached. This level of belief in the resulting conclusion is formed through an arduous process of hypothesis testing. This section will discuss the basics of hypothesis testing and the supervised test-statistics used by modern analysts and will follow [7] and [58].

Say we wanted to test whether the data measured at an experiment favoured one hypothesis versus some standard hypothesis. Usually, we refer to the standard hypothesis as the null hypothesis H_0 . In the context of particle physics, the Standard Model is usually taken as the null hypothesis. The analyst then asks whether an alternative hypothesis H_1 has better agreement with the data X . The data X being a realization of some random variable \mathbf{x} , which can take the form of a vector containing a combination of measurable quantities such as mass, momentum, etc. The random variable \mathbf{x} is distributed by its pdf $f(\mathbf{x})$. In all applicable scenarios, the pdf is conditional on a set of model parameters. Each hypothesis will have a different expectation for the set of model parameters. Therefore we take the pdfs to be conditional on the hypothesis $f(\mathbf{x}|H_i)$. Particle physicists refer to the null hypothesis $f(\mathbf{x}|H_0)$ as the background, and the alternative hypothesis $f(\mathbf{x}|H_1)$ as the signal⁴.

The random variable \mathbf{x} can take on an arbitrary number of dimensions. Con-

⁴It is assumed that the signal hypothesis includes both signal events plus background events.

sider the case of the ATLAS experiment, where the hard collision event produces high multiplicities of particles, each with their own physical measurements. Instead of attempting to model the distribution of \mathbf{x} through simulations, analysts consider dimensionally reduced variables in the form of test-statistics. Without loss of generality, we will assume that the test statistic is a scalar, $t = t(\mathbf{x})$. t is then distributed from $g(t|H_0)$ for background and $g(t|H_1)$ for signal. To test a hypothesis is to make a definitive statement based on some deciding criteria using the sampled test statistics t . A decision boundary is chosen such that $t = t_b$ at the boundary. Then the null hypothesis is said to be rejected based on which region, partitioned by the boundary, does the sampled t lay. This naturally leads to the type I & II errors. The probability of getting a type I error, or false positive rate, is defined as the probability of rejecting the null hypothesis when true, here denoted as α . The probability of getting a type II error, or the false negative rate, is the probability of failing to reject the null hypothesis when false, denoted as β . The two types of error can be cast in terms of the pdfs as,

$$\begin{aligned}\alpha &= \int_{t_b}^{\infty} g(t|H_0) dt \\ \beta &= 1 - \int_{t_b}^{\infty} g(t|H_1) dt\end{aligned}\tag{3.17}$$

Again, our test-statistic is 1-D and therefore our boundary is a single value. The same arguments apply to statistics of N dimensions, in which case, the boundary is a N-1 dimensional hypersurface.

The Type 1 error α is referred to as the significance. Most analysts will choose a decision boundary that minimizes α to a desired significance. Modern particle experiments require a high level of significance to trust a case of rejecting the Standard

Model expectation (the null hypothesis). Currently, the particle physics community demands a Gaussian equivalent significance of $\sim 5\sigma$. Since the desired significance sets the boundary we plot it as a function of the β (or false positive rate) for each boundary value. The resulting plot is known as the receive operating characteristic (ROC) curve, shown in Fig. 3.2. A test-statistic that perfectly discriminates the alternate hypothesis from the null will have a ROC curve that reaches the upper left of Fig. 3.2, for some boundary value t_b . This boundary value would become the optimal separating criteria for the two distributions under both hypotheses. Where as in the case of a completely linear ROC curve the discriminating power becomes 50/50, making it as useful as blindly guessing the outcome. Another application of the ROC curve is in finding how efficiently a test-statistic correctly identifies an event with new particles versus an event with just background. This will be the statistical lens used in Chapter 5, in which the true positive rate will shed light on how efficiently a detector accepts novel signal events, over the Standard Model background. So far the topic has been on testing a hypothesis based on some test-statistic. Making actual choices in a test-statistic isn't trivial and has lead to modern applications in non-linear multivariate methods and machine learning. The Neyman-Pearson lemma [60] gives us a procedure for constructing the optimal test-statistic—the likelihood ratio. In practice, we take the log likelihood ratio,

$$t(\mathbf{x}) = \text{Ln}\left(\frac{f(\mathbf{x}|H_0)}{f(\mathbf{x}|H_1)}\right). \quad (3.18)$$

The likelihood ratio is the optimal test-statistic in the sense that it optimizes the power of the test $(1 - \beta)$ for a set significance. This procedure becomes intractable as the dimensions of the data becomes large. Each multidimensional distribution must first be estimated using Monte Carlo methods, each carrying their own (nuisance)

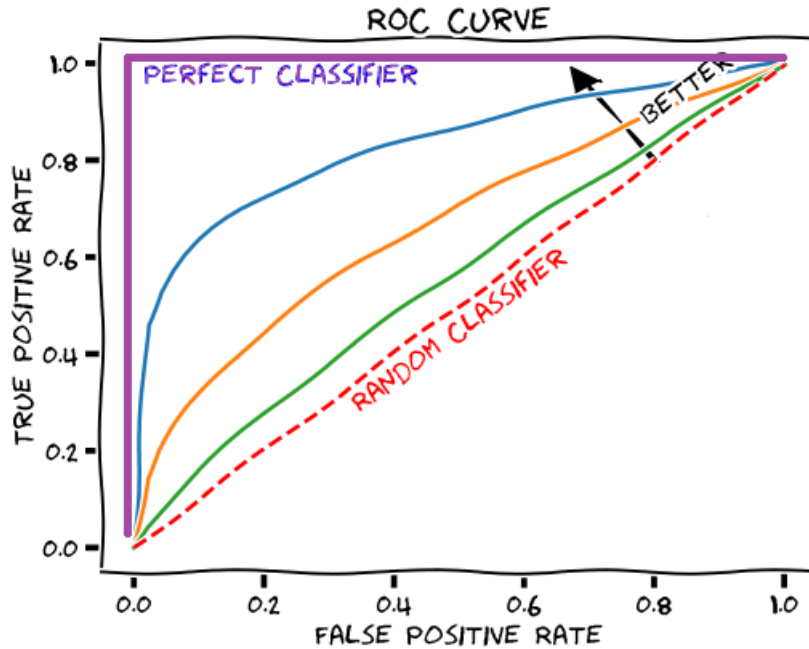


Figure 3.2: An educational sketch of the receiver operating characteristic (ROC) curve. The true positive rate (α) is plotted against the false positive rate (β). The dotted red line shows the completely random classifier, which has 0.5 discriminating power. The perfect classifier is shown in purple where, for a certain boundary value, the true positive rate is 100% and the false positive rate is 0%. [59]

parameters. Instead, test-statistics can be constructed by data-driven methods, where a function is trained on the data. The rest of this section will discuss machine learning methods which optimally train non-linear functions as a test-static. Specifically, classification algorithms will be looked at in terms of classifying signal events from background, trained on simulated data. The machine learning (ML) algorithm will be synonymous with the test-statistic and will be used interchangeably.

A ML algorithm can be set up by designating a task, a performance, and an experience. The task, in the case of classification, would be to distinguish multiple categories of an event. In essence, the task can be thought of estimating the pdfs of the data under each category/hypothesis. The performance stage is creating a metric

that tests and evaluates the performance of the ML on that specific task. An example of a performance metric for regression is the generalized least squares, or χ^2 -function. Through optimization of the performance metric the parameters of the regression are estimated. Finally, the experience stage considers the types of features we want the ML to experience. For example, the size and characteristics of the dataset (i.e. do we supervise the process by giving a labelled dataset to the algorithm or unsupervise it by giving it unlabelled data). The scope of this chapter will only focus on supervised learning, since the application of Chapter 5 will look at labelled simulation data.

Knowing that particle collision event classification is the task, measuring its performance can be further investigated. There is a general performance metric, or error loss predictor, for most classification algorithms. This metric is known as the cross-entropy loss within the statistics community [61] (Shannon entropy within the physics community),

$$H(x) = \sum_i^{\text{class}} \hat{p}_i \log(p(x|\theta)_i), \quad (3.19)$$

where the sum is over the i^{th} classifications category (signal and background), \hat{p} is the known label value of 0 (false) or 1 (true), and $p(x|\theta)_i$ is the label output from the ML algorithm with parameters θ on the data point x . The metric is applied on the entire labelled dataset, where a error cost $H(x)$ is evaluated for each labelled pair. To find the optimal parameters θ , the cross entropy is minimized. This is referred to as training the ML algorithm. Eq. (3.19) can be derived from the maximum (log) likelihood estimator of a multinomial distribution. Therefore the cross entropy is a well motivated loss function for any multinomial distributed output⁵, such as signal and background categories.

⁵This is the same argument for why the generalized least squares loss is used for regression, as it's the maximum log likelihood estimator for normally distributed random variables.

Closed form solutions of the performance metric's minimum, for a general model $p(x|\theta)$, do not exist. Instead, optimization methods like stochastic gradient descent are used to converge onto the global minimum. During the training stage the model parameters θ are updated using gradient descent for a desired batch size of training data. Over and under fitting of the model can occur during the training stage, due to factors such as poor model choices and/or a failure in the optimization. Any factors that affect the output but aren't explicit model parameters are known as hyper-parameters. A second independent dataset is then used to constrain these hyper-parameters, referred to as the development (dev) set⁶. To test how well the ML algorithm does on general data another independent dataset is used to test it's performance, referred to as the test set. Currently, there are a large number standardized ML algorithms each with applications suitable to certain tasks. Only neural networks will be discussed as an example, because of it's general structure highlights key aspects of non-linear methods.

3.4.1 Neural Networks

Modern neural networks (NN) were developed in the 1980s [62], motivated by how neurons in our brain function. Each neuron (node) represents an activation function between various connected layers or other neurons. NN were viewed as the universal approximator [63] — an algorithm that with enough data could predict any smooth function. The general NN is broken down into three layers; input layer, hidden layers, and output layer. An example of a general NN is shown in Fig. 3.3. The input layer consists of just the input features (i.e particle mass, momentum, angles) where each

⁶The development set is commonly confused with the test set for many ML applications. It should be noted that the test set must be unbiased, meaning it should not have any impact on the choices of model parameters or hyper-parameters. The dev set does impact the model choices by tuning the hyper-parameters.

feature is designated its own node. On the other end of the network is the output layer, where each node represents some form of the output. The number of nodes inside the output layer is determined by the problem, or task. There would be a single output node for a regression task, where as a multi-categorical classification task would require multiple nodes for each category. The hidden layers are essentially any layer of nodes that do not contain the input or output layers. Meaning, there can be any set number of hidden nodes within a NN. For example, the simplest regression network would comprise of just the input layers, the features of our data, with a single node output layer. Each input node representing a parameter in the regression model. The final output would consist of just the linear weighted sum of the input node values. This example is in essence just standard linear regression.

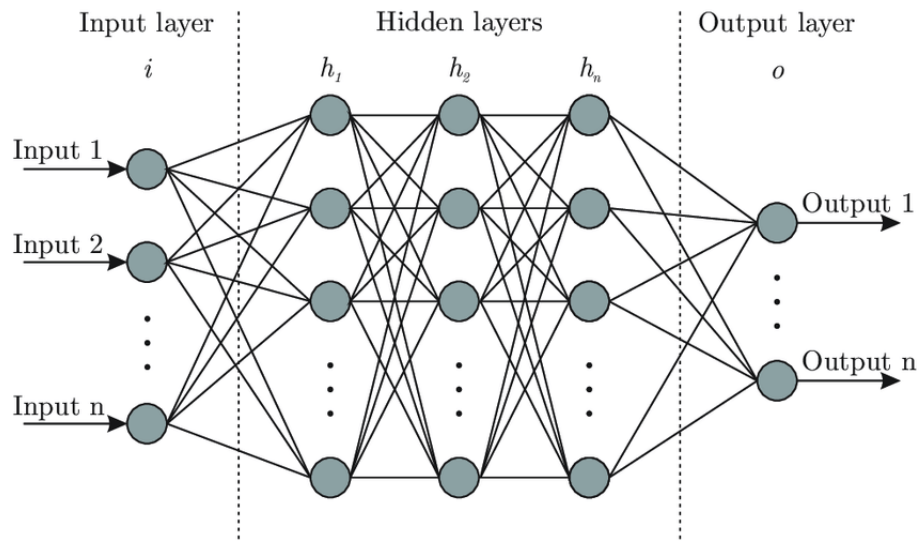


Figure 3.3: A schematic of a general NN architecture. The NN is organized in input layer, hidden layers, and output layer. The weights of each layer are represented by each connection. All connections are shown but can be removed by setting its corresponding weight to zero.

Non-linear methods generally outperform linear methods on complex tasks. The reason being, that for some complex tasks, linear methods are constrained in their solution spaces when attempting to solve the task. An example of such a issue is the

XOR problem [64], where a ML algorithm is tasked to predict the output of a XOR logic gate. If each node of a NN computed only a linear function of the previous layer's nodes, then NN would need a node in the input layer for each object in the XOR gate. In comparison a non-linear NN could solve the task with less than two nodes per layer. What makes a NN non-linear are the hidden layer connections, where each node's output is fed to a chosen non-linear activation function $\sigma(x)$. If the activation function was itself a linear function than the total output of the NN would also be linear, because compounded linear functions are themselves linear. Therefore for a NN to be more robust than conventional linear methods at least one of its layer's output must be a non-linear function of its input. With all of that in mind, a general neural network architecture is defined at the k^{th} layer as,

$$\begin{aligned} z^{(k)} &= \mathbf{W}^{(k-1)}h^{(k-1)}, \\ h^{(k)} &= \sigma^{(k)}(z^{(k)}), \end{aligned} \tag{3.20}$$

where \mathbf{W}^i , h^i , z^i , σ^i are the weight vector, layer output, linear output, and activation function of the i^{th} layer. For a NN with l layers, the output layer is defined as h^l and the input layer as h^0 .

Guaranteeing a consistent output, or an optimal convergence, requires the activation function to be monotonic. In the case of a classification task, the output layers would have a activation function such that its output can be partitioned into a categorical variable (i.e. signal or background). The standard function that accomplishes this is the logistic function,

$$\sigma(z) = \frac{1}{1 + e^{-z}}. \tag{3.21}$$

For a binary categorical output, two regions are chosen to discriminate between the two categories. Usually this is done by equal splitting, $\sigma < 0.5$ for signal and $\sigma > 0.5$ for background.

Once the NN architecture (or any other ML algorithm) is defined, the performance metric Eq. (3.19) is minimized using gradient descent on batched examples from the training set. Where each pass of the gradient descent updates the weight vectors \mathbf{W} . The architecture is further refined as the hyper-parameters (number of nodes, layers, etc) are tuned using the dev set. Finally, a test set is used to give an unbiased estimate on the precision and accuracy of the trained ML algorithm, usually visualized using a ROC curve of Fig. 3.2.

Chapter 4

Gravitational Waves from Multiple Hidden Sectors

“The universe has spoken and we have understood”

— *David Blair*

4.1 Introduction

The recent experimental detection of gravitational waves [65] gives humanity a new way to observe the universe. Future experiments [66–75] will greatly expand the frequency range observable. Thus far, experiments have only observed recent events such as black hole mergers, but phase transitions in the early universe can leave an imprint as a *stochastic* gravitational wave background [76–81]. Thus, searches for this background of gravitational waves can give direct information of the history of the universe before big bang nucleosynthesis. Because gravity is universal, gravitational waves can allow us to probe hidden sectors that couple very weakly, or not at all, to the Standard Model as long they are reheated after inflation. This was first explored

in [39], and there has been significant work on this idea since [40, 82–98].

In this work, we explore the possibility of having multiple decoupled hidden sectors. Large numbers of hidden sectors can solve the hierarchy problem as in the Dvali Redi model [99], in the more recently explored N naturalness [41] framework, or in orbifold Higgs models [100, 101]. They can also be motivated by dark matter considerations [85, 102–104]. Motivated by solutions to the hierarchy problem, we consider hidden sectors with the same particle content as the Standard Model that have all dimensionless couplings (defined at some high scale) equal to those of the Standard Model. The only parameter that varies across sectors is the dimension two Higgs mass squared parameter, m_H^2 . This simple ansatz can lead to very rich phenomenology and interesting gravitational wave spectra, but we stress that it is only a starting point for exploring the space of theories with multiple hidden sectors.

In this setup, there are two qualitatively different kinds of sectors:

- **Standard Sectors:** Those with $m_H^2 < 0$ where electroweak symmetry is broken by the vacuum expectation value (vev) of a fundamental scalar. As in [41], we assume that the standard sector with the smallest absolute value of m_H^2 is the Standard Model.
- **Exotic Sectors:** Those with $m_H^2 > 0$. In this case, electroweak symmetry is preserved below the mass of the Higgs, and broken by the confinement of QCD [105].

Cosmological observations, particularly limits on extra relativistic degrees of freedom at the time of Big Bang Nucleosynthesis and the time of the formation of the cosmic microwave background (CMB) [36], require that most of the energy in the universe is in the Standard Model sector as we will quantify. Therefore, the hidden sectors cannot be in thermal equilibrium at any time, and the physics of reheating must dump energy

preferentially in the Standard Model sector. This can be accomplished with primordial axion-like particle (ALP) models [106, 107] and with the reheaton method [41]. We will also explore alternative parametrizations of reheating that satisfy this condition.

In all the above models, there is some energy in the hidden sectors, and these sectors undergo thermal evolution independent of the SM sector. If their initial reheating temperature is above their weak scale, the standard sectors will undergo phase transitions associated with the breaking of electroweak symmetry and with confinement of QCD. The exotic sectors will also undergo a phase transition when QCD confines and electroweak symmetry is broken simultaneously. The condition for these transitions to leave imprints on the stochastic gravitational wave spectrum is that they strongly first order phase transitions (SFOPT) [76–79]. This does not occur at either the electroweak or QCD phase transition in the SM, but as we will show, it does happen for the QCD phase transition in some standard sectors and in *all* exotic sectors that reheat above the QCD phase transition.

This work is organized as follows: section 4.2 introduces the particle content of the model, section 4.3 discusses the phase transition behaviour of the both the standard and exotic sectors present, section 4.4 lays out hidden sector reheating, section 4.5 applies constraints from cosmological observables allowing for the calculation of gravitational wave signatures in section 4.6, and, finally, section 5.6 ties everything up.

4.2 Particle Setup

We consider the following Lagrangian as in [41]:

$$\mathcal{L} = \sum_{i=-N/2}^{N/2} \mathcal{L}_i, \quad (4.1)$$

with $\mathcal{L}_0 = \mathcal{L}_{\text{SM}}$ being the Standard Model Lagrangian, and \mathcal{L}_i being a copy of the SM Lagrangian with different fields, but with all dimensionless parameters the same. Each of the Lagrangians does contain a dimensionful operator:

$$\mathcal{L}_i \subset - (m_H^2)_i H_i^\dagger H_i \quad (4.2)$$

where H_i is a Higgs field in each sector, and the mass term is parametrically given by

$$(m_H^2)_i \sim -\frac{\Lambda_H^2}{N}(2i + r), \quad (4.3)$$

where Λ is some high scale cutoff, N is the number of sectors, and r is the mass parameter in the SM in units of Λ_H^2/N . We view the parameterization of Eq. (4.3) as a random distribution in theory space up to the cutoff Λ , therefore this setup solves the hierarchy problem if $r \sim \mathcal{O}(1)$ [41]¹ and our sector is the one that has the smallest absolute value of the Higgs mass parameter. We have taken for simplicity that there equal numbers sectors with positive and negative m_H^2 , but this assumption does not affect our analysis. This N naturalness framework can be generalized: the various sectors can possess a wide range of particle content that can be freely selected by the model builder. The one exception to this is that “our” sector must consist of the Standard Model.

From the above Lagrangians, the Higgs in sectors with $i \geq 0$ will get a vev given by:

$$v^i = \sqrt{-(m_H^2)_i/\lambda_i} \sim \Lambda_H \sqrt{\frac{2i + r}{\lambda N}}, \quad (4.4)$$

λ_i is the quartic coefficient of the scalar potential and is the same across all sectors, $\lambda_i = \lambda$. This is another way to see how this framework can solve the hierarchy

¹Constraints require r to be somewhat smaller than 1.

problem: the Higgs vev is parametrically smaller than the cutoff for $N \gg 1$. The “standard sectors” with $i > 0$ feature electroweak symmetry breaking just like in the SM, however the vevs scale with the changing mass parameter: $v_i \sim v_{\text{SM}}\sqrt{i}$. This means that the masses of the fermions and the W and Z will also increase proportional to \sqrt{i} . The consequences of this scaling on the confinement scale of QCD in the $i \geq 1$ sectors is further discussed in Sec. 4.3.

The “exotic sectors” with $i < 0$ provide a radical departure from our own. $m_H^2 > 0$ leads to no vev for the Higgs, and electroweak symmetry is only broken at very low scales due to the phase transition from free quarks to confinement at the QCD scale Λ_{QCD} [105], and the masses of the W and Z are comparable to those of QCD resonances. The mass of fundamental fermions are produced via four-fermion interactions generated after integrating out the SU(2) Higgs multiplet. This leads to very light fermions:

$$m_f \sim y_f y_t \Lambda_{\text{QCD}}^3 / (m_H^2)_i \leq 100 \text{ eV}, \quad (4.5)$$

with y_f representing the Yukawa coupling to fermion f . As we will see, the extremely light quarks that appear in these sectors dramatically change the nature of the QCD phase transition — unlike the SM, the transition is strongly first order. Again, this is further developed in Sec. 4.3. Crucially, this results in the production of gravitational waves. This is the physical signature we explore in this paper; the calculation and results are presented in Sec. 4.6.

4.3 QCD Phase Transition

We now study the nature of the QCD phase transition across the different sectors. Due to the confining nature of QCD, the exact nature of the phase transition is often difficult to ascertain analytically and requires the study of lattice simulations. In

the SM, it is known that the phase transition is a crossover and does not lead to gravitational wave signals [108, 109]. In the general case with 3 or more colours, the phase transition can be strongly first order in two regimes [110–112]:

- Three or more light flavours.
- No light flavours.

Light indicates a mass small compared to the confinement scale Λ_{QCD} , but what that means quantitatively is not precisely determined. In the SM, the up and down quarks are light, but the strange is not sufficiently light for an SFOPT. For the standard sectors in our setup, the quark masses increase with increasing vev, so for sufficiently large i , all the quarks will be heavier than Λ_{QCD} ,² and those large i sectors will undergo an SFOPT if they are reheated above the the confinement scale. Conversely, exotic sectors with zero vev feature six very light quarks, so *all* the exotic sectors undergo SFOPT at the temperature of QCD confinement.

We now calculate the QCD confinement scale for each sector following the same procedure as [113]. First, due to the parameters of each sector being taken to be identical save for the Higgs mass squared (thus $v \neq v_i$, where v is the SM vev), we assume that the strong coupling of every sector is identical at some high scale. Using the one-loop running, the β function can be solved:

$$\alpha_s^i(\mu) = \frac{2\pi}{11 - \frac{2n_f^i}{3}} \frac{1}{\ln \mu/\Lambda^i}, \quad (4.6)$$

where n_f^i is the number of quark flavours with mass less than $\mu/2$ and Λ^i is the scale where it would confine if all quarks remain massless. In the SM defined at scales well above all the quark masses, we have $\Lambda_{QCD} = 89 \pm 5$ MeV in \overline{MS} [114]. Because we

² Λ_{QCD} does vary with i , but the sensitivity is very weak as we will see below.

have set the strong couplings equal at high scales, $\Lambda = \Lambda^i$ for all i at high scales for all sectors. However, since the masses of the quarks in each sector are different, we end up with a unique running of the coupling for each sector. At every quark mass threshold for a given sector, we match the coupling strengths above and below the threshold and determine the new Λ^i for the lower scale. For example, at the mass of the top quark, we match a five flavour coupling with the six flavour one:

$$\alpha_s^{i(5)}(2m_t^i) = \alpha_s^{i(6)}(2m_t^i) \quad (4.7)$$

and thus

$$\Lambda_{(5)}^i = (m_t^i)^{2/23} (\Lambda_{(6)}^i)^{21/23}. \quad (4.8)$$

Suppressing the i 's for notational cleanliness, we can arrive at similar relations at the bottom and charm thresholds

$$\begin{aligned} \Lambda_{(4)} &= (m_b)^{2/25} (\Lambda_{(5)})^{23/25}, \\ \Lambda_{(3)} &= (m_c)^{2/23} (\Lambda_{(4)})^{25/27}. \end{aligned} \quad (4.9)$$

These can be combined to show that

$$\Lambda_{(3)} = (m_t m_b m_c)^{2/27} (\Lambda_{(6)})^{21/27}. \quad (4.10)$$

This type of matching procedure can be done as many times as necessary for a given sector. The process terminates when Λ_i for a given scale is larger than the next quark mass threshold (i.e running the scale down arrives at the Λ_{QCD} phase transition before reaching the next quark mass scale). In cosmological terms, we can envision a sector's thermal history unfolding, whereas the plasma cools below each quark mass threshold

and said quarks are frozen out. At a certain point, the sector arrives at the QCD phase transition and confinement occurs — if this occurs when ≥ 3 quarks are at a much lower scale or all quarks have already frozen out, we get the desired phase transition.

4.3.1 Standard Sectors

As shown in Eq. (4.4), for standard sectors with increasing index i the vevs of said sectors increase $v_i \propto \sqrt{i}$. This leads to increasingly heavy particle spectra for higher sectors — eventually leading to sectors that are essentially pure Yang-Mills that feature strong first order phase transitions. This, of course, prompts the question: at what index i do said phase transitions begin? Using the methods outlined in the prior section we determine Λ_{QCD} to have a relevant value of

$$\Lambda_{(2)}^i = (m_s^i m_c^i m_b^i m_t^i)^{2/29} (\Lambda_{(6)}^i)^{21/29} \quad (4.11)$$

at the energy scale we're interested in. $\Lambda_{(6)}^i$ is identical for all sectors and is taken to have a standard model value of $\Lambda_{MS}^{(6)} = (89 \pm 6) \text{ MeV}$ [114]. Rewriting Eq. (4.11) in terms of standard model variables,

$$\Lambda_{(2)}^i = (m_s m_c m_b m_t i^2)^{2/29} (\Lambda_{(6)})^{21/29}. \quad (4.12)$$

where m_q without a superscript is the mass of q in the SM. We take the sector with SFOPT to be the ones when the mass of the up quark, down quark, and QCD phase transition scale are all comparable:

$$m_u^i \sim m_u \sqrt{i} \sim (m_s m_c m_b m_t i^2)^{2/29} (\Lambda_{(6)})^{21/29}. \quad (4.13)$$

This can be solved for i :

$$i^c \sim \frac{(m_s m_c m_b m_t)^{4/21} (\Lambda_{(6)})^2}{(m_u)^{58/21}} \sim 10^6. \quad (4.14)$$

As we will see in Sec. 4.4, in the original N naturalness setup [41], the energy dumped into the i th sector scales as i^{-1} , so there will not be enough energy in the sectors with $i > i^c$ to see a signature of these phase transitions. However, if we move away from the original N naturalness reheating mechanism and begin exploring mirror sectors with large vevs and with relative energy densities $\rho_i/\rho_{SM} \sim 10\%$, a possibility allowed by current constraints, we can have sectors with relatively high dark QCD scales that produce detectable gravitational waves. From Eq. (4.11) we can determine the confinement scale of an arbitrary mirror sector. If we take Higgs vevs as high as the GUT scale $\sim 10^{16}$ GeV, then we can use Eq. (4.12) to get confinement scales as high as ~ 38 GeV. The signals of this sector and other test cases like it are explored in Sec. 4.6.

4.3.2 Exotic Sectors

In every exotic sector the fermion masses are exceptionally light: their masses are generated by dimension six operators with the Higgs integrated out as shown in Eq. (4.5), and are therefore all below the confinement scale. The exotic sectors all have identical one-loop running of the QCD gauge coupling, and thus all have approximately the same confinement scale given by $\Lambda_{\text{ex}} \sim 90$ MeV. These sectors all have six light fermions, so a strong first order phase transition occurs for all exotic sectors at this temperature. The confinement of these sectors directly leads to the production of both baryons and mesons as we have the spontaneous breaking of $SU(6) \times SU(6) \rightarrow SU(6)$ and thus 35 pseudo-Goldstone bosons (pions). The masses

obtained through the phase transition can be approximated through the use of a generalization of the Gell-Mann–Oakes–Renner relation [115, 116],

$$m_\pi^2 = \frac{V^3}{F_\pi^2}(m_u + m_d), \quad (4.15)$$

where $V \sim \Lambda_{QCD}$, F_π is the pion decay constant. One expects that within a given sector $F_\pi \sim V \sim \Lambda_{QCD}$ [116] and as exotic sectors have $\Lambda_{ex} \sim 90$ MeV while the SM features $\Lambda_{QCD} = (332 \pm 17)$ MeV [114] we expect at most $\mathcal{O}(1)$ difference in the $\sqrt{\frac{V^3}{F_\pi^2}}$ coefficient relative to the SM value. So, for pions in exotic sector i :

$$m_\pi^i \sim \sqrt{\frac{m_a^i + m_b^i}{m_u + m_d}} m_\pi. \quad (4.16)$$

Here, a and b denote the component quark flavours.

4.4 Reheating N Sectors

A key issue within N naturalness is how to predominantly gift energy density to our own sector so as to not be immediately excluded by cosmological constraints, particularly those from number of effective neutrinos (N_{eff}). Here we review the results of [41]. Reheating occurs through the introduction a “reheaton” field. After inflation, the reheaton field possesses the majority of the energy density of the Universe. Although this field can generically be either bosonic or fermionic, we reduce our scope to a scalar reheaton ϕ . Our focus is primarily the production of gravitational waves from multiple sectors and a fermion reheaton does not change the scaling of the energy density of the exotic sectors and thus does not affect expected gravitational wave profiles.

In order to maintain the naturalness of our SM sector, the reheaton cou-

pling is taken to be universal to every sector's Higgs. However, a large amount of the Universe's energy density must ultimately be deposited in our own sector for N naturalness to avoid instant exclusion. In order to accomplish this, the decay width of the reheaton into each sector must drop as $|m_H|$ grows. If we insist that the reheaton is a gauge singlet that is both the dominant coupling to every sector's Higgs and lighter than the naturalness cutoff Λ_H/\sqrt{N} , then we construct a model that behaves as desired. The appropriate Lagrangian for a scalar reheaton ϕ is:

$$\mathcal{L}_\phi \supset -a\phi \sum_i |H_i|^2 - \frac{1}{2}m_\phi^2\phi^2. \quad (4.17)$$

Note that cross-quartic couplings of the form $\kappa|H_i|^2|H_j|^2$ that could potentially ruin the spectrum of N naturalness are absent, taken to be suppressed by a very small coupling. Effective Lagrangians for the two different types of sectors present in this theory can be obtained by integrating out of the Higgs bosons in every sector:

$$\begin{aligned} \mathcal{L}_\phi^{v \neq 0} &\supset C_1 a y_q \frac{v}{m_h^2} \phi q q^c, \\ \mathcal{L}_\phi^{v=0} &\supset C_2 a \frac{g^2}{16\pi^2 m_H^2} \phi W_{\mu\nu} W^{\mu\nu}, \end{aligned} \quad (4.18)$$

with C_i representing numerical coefficients, g the weak coupling constant, and $W^{\mu\nu}$ the SU(2) field strength tensor. Immediately from Eq. (4.18), we can see that the matrix element for decays into standard sectors is inversely proportional to that sectors Higgs mass, $\mathcal{M}_{m_H^2 < 0} \sim 1/m_{h_i}$ (since $v \sim m_H$). The loop decay of $\phi \rightarrow \gamma\gamma$ is always sub-leading and can be neglected. It should be noted that as one goes to sectors with larger and larger vevs, the increasing mass of the fermions ($m_f \sim v_i \sim v_{SM}\sqrt{i}$) eventually leads to situations where the decay to two on-shell bottom or charm quarks is kinematically forbidden, $m_\phi < 2m_q$. For sectors where this kinematic threshold is

passed for charm quarks, the amount of energy in these sectors becomes so small that contributions to cosmological observables can be safely ignored. All in all, we end up with a decay width that scales as $\Gamma_{m_H^2 < 0} \sim 1/m_h^2$. Since we can expect energy density to be proportional to the decay width, $\frac{\rho_i}{\rho_{SM}} \approx \frac{\Gamma_i}{\Gamma_{SM}}$, this indicates that energy density of standard sectors falls:

$$\rho_i \sim r_s \frac{\rho_{SM}}{i} \quad (4.19)$$

with r_s being the ratio of the energy density of the first additional standard sector over the energy density of our sector. For the exotic sectors, Eq. (4.18) indicates a matrix element scaling $\mathcal{M}_{m_H^2 > 0} \sim 1/m_{H_i}^2$ and is also loop suppressed. This leads to a significantly lower energy density than the standard sectors. Both the decay width and energy density for these sectors scale as:

$$\Gamma_{m_H^2 > 0} \sim \rho_i \sim 1/m_H^4 \sim 1/i^2. \quad (4.20)$$

As a final note, in this setup the reheating temperature of the SM, T_{RH} , has an upper bound on the order of the weak scale. If this bound is not observed, the SM Higgs mass would have large thermal corrections — leading to the branching ratios into other sectors being problematically large [41]. Thus we only consider relatively low reheating temperatures $\lesssim 100$ GeV.

Ultimately, after examining the gravitational wave case produced by standard N naturalness, we also consider a more generic parameterization where the reheating temperature of each sector is a free parameter and is in general uncorrelated with the Higgs mass parameter. This allows us to explore a broader model space with multiple dark sectors at a huge range of scales. For these models, the reheating mechanism remains unspecified.

4.5 Constraints

In general, the multi-hidden sector models explored feature a huge number of (nearly) massless degrees of freedom. Dark photons and dark neutrinos abound in these sectors and, assuming a relatively high reheat temperature, the leptons, quarks, and heavy bosons of these sectors can also be relativistic. In N naturalness this feature is realized quite dramatically: each of the N sectors possess relativistic degrees of freedom. The presence of these particles can have two main effects: extra relativistic particles can alter the expansion history of the universe through changes to the energy density or hidden sectors can feature annihilations that reheat the photons or neutrinos of our sector near Big Bang Nucleosynthesis (BBN) and affect the light element abundances. The effective number of neutrino species, N_{eff} , is impacted by these contributions and, as such, is the strictest constraint that must be dealt with when studying these type of multi-phase transition models. The SM predicts that $N_{eff}^{SM} = 3.046$ [35]. This is in good agreement with the 2σ bounds from studies of the Cosmic Microwave Background (CMB) by Planck combined with baryon acoustic oscillations (BAO) measurements [36]:

$$N_{eff} = 2.99_{-0.33}^{+0.34}. \quad (4.21)$$

Various different assumptions about the history of the universe can be made and different data sets can be chosen to obtain slightly different results [94] — for the purposes of this exploratory work, wading through this landscape is unnecessary. Additionally,

$$\frac{(\Delta N_{eff}^i)_{CMB}}{(\Delta N_{eff}^i)_{BBN}} \geq 1 \quad (4.22)$$

for any decoupled hidden sector [41]. Because the constraints on N_{eff} are stronger at photon decoupling than at BBN, we can focus purely on the constraints provided by

the former. Future CMB experiments [117] will improve the bound from Eq. (4.21) by about an order of magnitude. This could significantly reduce the allowed temperature ratio of any hidden sector, or alternatively could provide evidence for such sectors in a way that is complementary to the gravitational wave signatures described below. For fully decoupled sectors that never enter (or reenter) thermal equilibrium with our sector, we obtain additional contributions to N_{eff}^{SM} [94]

$$\Delta N_{eff} = \frac{4}{7} \left(\frac{11}{4} \right)^{4/3} g_h \xi_h^4. \quad (4.23)$$

Here, g_h represents the effective number of relativistic degrees of freedom for the hidden sector³, and we parameterize the hidden sector temperature by [94]

$$\xi_h \equiv \frac{T_h}{T_\gamma}, \quad (4.24)$$

and these should be evaluated at the time of photon decoupling. We take this approach and generalize it to include many additional sectors:

$$\Delta N_{eff} = \sum_i \frac{4}{7} \left(\frac{11}{4} \right)^{4/3} g_i \xi_i^4. \quad (4.25)$$

For a dark sector with one relativistic degree of freedom, its temperature must be $T_{DS} \sim 0.6 T_{SM}$ to not be excluded. Applying the energy density formula [118],

$$\rho_i = \frac{\pi^2}{30} g_i T_i^4, \quad (4.26)$$

to both said dark sector and the SM then taking the ratio indicates that the dark sector would have an energy density $\rho \sim 0.038 \rho_{SM}$.

³ $g_h = N_{\text{boson}} + 7N_{\text{fermion}}/8$.

4.5.1 Exotic Sector Contributions

We begin by computing the constraints on exotic sectors; these are significantly weaker than those for standard sectors [41]. At the time of photon decoupling, $T_\gamma \sim 0.39$ eV while the temperature of the exotic sectors is lower. This means that for sectors with small and moderate i , we can use Eqs. (4.5) and (4.16) to see that the pions will be non-relativistic leaving at most 7.25 effective degrees of freedom per sector from photons and neutrinos. For very large i , the pions can be much lighter, but those sectors also have very little energy in them in the standard reheating scenario. Coupling the number of effective degrees of freedom per sector with the energy density scaling of $\sim 1/m_H^4$ as in Eq. (4.20) means that the zero vev sectors have small temperature ratios. Assuming a reheating temperature of 100 GeV and a completely uniform distribution of sectors, the temperature of the first exotic sector is slightly more than 6% of our sector at reheating. Applying Eq. (4.25) to this particular situation gives us:

$$\Delta N_{eff} = \sum_i \frac{4}{7} \left(\frac{11}{4}\right)^{4/3} g_i \left(\frac{(T_{RHE1}/T_{RH})}{i^{1/2}}\right)^4 \sim 10^{-4}, \quad (4.27)$$

with T_{RHE1}/T_{RH} being the ratio of the reheat temperatures of the 1st exotic sector and our own sector (0.06 in standard $N_{naturalness}$ with $r = 1$). This sum is dominated by $i = 1$, the sector with the lowest Higgs mass (and thus the most energy density) gives us a contribution of $\mathcal{O}(10^{-4})$ to ΔN_{eff} . Evolving the sectors thermal histories forward in time to the recombination era gives us a slightly larger value, but still of order $\mathcal{O}(10^{-4})$, well below current CMB bounds. It should be noted that modifying the exotic sectors' structure (e.g. adjusting the exotic sectors to have a lower Higgs mass squared or clustering multiple hidden sectors close to the first exotic one) leads to a ΔN_{eff} contribution that is larger than the base $N_{naturalness}$ case. This increase

is typically not excluded by current bounds, indicating a large degree of liberty in the structure and number of exotic hidden sectors.

4.5.2 Standard Sector Contributions

Within the context of vanilla N naturalness, the majority of contributions arise from standard sectors. This is explored in detail in [41]; here we briefly summarize these arguments. All additional standard sectors are very similar to our own: they have the same particle content and couplings and differ only by the Higgs mass. As our sector is taken to be the lightest so as to be preferentially reheated, every other standard sector features an earlier freeze-out of their respective particles. This ultimately leads to each sector having at most the same number of relativistic degrees of freedom as the SM.

In [41], the standard sector contributions are expressed as:

$$\Delta N_{eff} = \frac{1}{\rho_{\nu}^{us}} \sum_{i \neq us} \rho_i. \quad (4.28)$$

In the case that the reheaton is lighter than the lightest Higgs (ours), this can be expressed as

$$\begin{aligned} \Delta N_{eff} &\sim \sum_{i=1}^{N_b} \frac{1}{2i+1} + \frac{y_c^2}{y_b^2} \sum_{i=N_b+1}^{N_c} \frac{1}{2i+1} \\ &\simeq \frac{1}{2} \left(\log 2N_b + \frac{y_c^2}{y_b^2} \log \frac{N_c}{N_b} \right) \end{aligned} \quad (4.29)$$

with $y_{c,b}$ representing the charm and bottom yukawa couplings and

$$N_{b,c} = \left(\frac{m_\phi^2}{8m_{b,c}^2} - \frac{1}{2} \right) \quad (4.30)$$

with m_ϕ being the mass of the reheaton.

Application of these results indicates that for a majority of the parameter space, vanilla N naturalness requires mild fine-tuning (r in Eq. (4.4) set to a value $\lesssim 1$). Numerical results for the fine-tuning required for various reheaton masses were presented in [41].

4.5.3 Generalized Reheating Scenarios

The generalization of possible reheating mechanisms mentioned in section 4.4 — where the reheating mechanism no longer depends on the Higgs’ mass parameter of a given sector — opens up a wide range of hidden sectors for study. Specifically, this allows mirror sectors with large Higgs vevs to be reheated to significant energy densities and thus produce gravitational waves with enough power to be detected. Crucially, despite this analysis being limited to mirror sectors with large Higgs masses, this analysis pertains to any strong, confining phase transition at high scales. Since N_{eff} constraints remain our strongest cosmological bounds for massive standard sectors, our starting point for exploring the limits of high transition temperatures is Eq. (4.25). Assuming heavy, standard sectors (with the only relativistic particles being photons and neutrinos) we can saturate the bounds of Eq. (4.21) and solve for the maximum temperature allowed for any number of sectors:

$$\begin{aligned}
T_i &\sim 0.38 T_{SM} && 1 \text{ hidden sector,} \\
T_i &\sim 0.25 T_{SM} && 5 \text{ hidden sectors,} \\
T_i &\sim 0.21 T_{SM} && 10 \text{ hidden sectors,} \\
T_i &\sim 0.12 T_{SM} && 100 \text{ hidden sectors,}
\end{aligned}
\tag{4.31}$$

where all the hidden sectors have the same temperature as one another.

Using these restrictions, we can examine the behaviour of standard sectors with a much larger vev than our own. In terms of the N naturalness framework, this means we can get an SFOPT for QCD if we look at sectors with i greater than the critical index of Eq. (4.14) where all the quark masses are above the QCD confinement scale, as long as their temperatures are below the bounds presented here.

4.6 Gravitational Wave Signals

We now turn to the gravitational wave signatures of our setup. At high temperatures, each of the hidden sectors has QCD in the quark/gluon phase, but at temperatures around $\Lambda_{\text{QCD},i}$, the i^{th} sector undergoes a phase transition into the hadronic phase that we computed for the different sectors in Sec. 4.3. As discussed in that section, this phase transition will be strongly first order (SFOPT) for certain numbers of light quarks, which will generate gravitational waves. This differs from QCD in the SM sector, as the PT is a crossover and not first order [119]. A SFOPT proceeds through bubble nucleation, where bubbles of the hadronic phase form in the vacuum of the quark phase. These bubbles will expand, eventually colliding and merging until the entire sector is within the new phase. These bubbles are described by the following Euclidean action [120]:

$$S_E(T) = \frac{1}{T} \int d^3x \left[\frac{1}{2} (\nabla\phi)^2 + V(\phi, T) \right], \quad (4.32)$$

where the time component has been integrated out due to nucleation occurring not in vacuum but in a finite temperature plasma. ϕ is the symmetry breaking scalar field with a non-zero vev. In the case of the chiral phase transition, the scalar field breaking the $SU(N_f)_R \times SU(N_f)_L$ chiral symmetry is the effective quark condensate

$\phi_i \sim \langle q\bar{q} \rangle_i$ of the respective sector. We leave the thermalized potential $V(\phi, T)$ general. As previously stated, an exact QCD potential at the time of the chiral phase transition is not well understood outside of lattice results. In [40] chiral effective Lagrangian was used to calculate a low energy thermalized potential for confining $SU(N)$. The amount of energy density dumped into the individual sectors dictates the energy budget for the PT and hence for the gravitational waves. Assuming that the SM sector is radiation dominated, a quantity that characterizes the strength of the PT is the ratio of the latent heat of the phase transition, ϵ , to the energy density of radiation, at the time of nucleation [121],

$$\alpha \equiv \frac{\epsilon}{g_* \pi^2 (T_\gamma^{nuc})^4 / 30}, \quad (4.33)$$

with ϵ being calculable from the scalar potential. Assuming that there is a negligible amount of energy being dumped back into the SM, which would cause significant reheating of ρ_γ , the latent heat ϵ should correspond to the energy density of the hidden sector going through the PT. The parameter g_* in the denominator of Eq. (4.33) is the number of relativistic degrees of freedom at the time of the phase transition, with contributions from species in both the visible and dark sectors. It has weak temperature dependence in a single sector, but when dealing with multiple hidden sectors, g_* gains contributions from all N sector's relativistic degrees of freedom, weighted by their respective energy densities

$$g_* = g_{*,\gamma} + \sum_i g_{*,i} (\xi_i)^4, \quad (4.34)$$

with ξ being the temperature ratio defined in Eq. (4.24). The bounds from effective number of neutrinos [36] mean that $\xi_i \lesssim 1$ for all i , so $g_* \approx g_{*,\gamma}$. In the case of dark

QCD-like chiral phase transitions, the temperature of the phase transition is on the order of the symmetry breaking scale of the respective sector, $T_h^i \sim \mathcal{O}(\Lambda_{QCD,i})$. The work of [40] calculated α with an effective chiral Lagrangian have found various upper bounds. We take the optimistic scenario where the numerator is bounded above by the symmetry breaking scale

$$\alpha_i \approx \xi_i^4 \approx \left(\frac{\Lambda_{QCD,i}}{T_\gamma^{nuc}} \right)^4, \quad (4.35)$$

where T_γ^{nuc} is the temperature of the SM photon bath at the time of the phase transition. Another important parameter to characterize the phase transition is its inverse timescale, β [80]. The inverse timescale can be calculated using the action in Eq. (4.32),

$$\beta \equiv \left. \frac{dS_E(T)}{dt} \right|_{t=t_{nuc}}. \quad (4.36)$$

The ratio of β and the Hubble constant, at the time of nucleation, H controls the strength of the GW signal,

$$\frac{\beta}{H} = T_h^{nuc} \left. \frac{dS_E(T)}{dT} \right|_{T=T_h^{nuc}}. \quad (4.37)$$

Due to the lack of a general analytic QCD potential, it is not possible to use Eq. (4.37) to calculate β/H . There are dimensional arguments [77, 78] that predict $\beta/H \sim 4\text{Log}(M_p/\Lambda_{QCD,i})$, although these arguments make specific assumptions about the potential. In more recent work, some authors [40, 96] have attempted to estimate it using first-order chiral effective theories and the Polyakov-Nambu-Jona-Lasinio (PNJL) models which motivates a β/H of $\mathcal{O}(10^4)$. These studies claim a large range of values with no consensus reached on the precise order of the scaled inverse timescale. Under these circumstances, our signal projections will consider both extremes of the

parameter space where, $\beta/H \sim 10 - 10^4$. A more realistic scenario may exist in between both cases.

4.6.1 Production of Gravitational Waves

Gravitational waves are produced with contributions from different components of the SFOPT's evolution. It is commonplace to parameterize the spectral energy density in gravitational waves by [122]

$$\Omega_{\text{GW}}(f) \equiv \frac{1}{\rho_c} \frac{d\rho_{\text{GW}}(f)}{d\log(f)}, \quad (4.38)$$

where $\rho_c = 3H^2/(8\pi G)$ is the critical energy density. The total gravitational wave signal is a linear combination of three leading contributions:

$$h^2\Omega_{\text{GW}} \approx h^2\Omega_\phi + h^2\Omega_v + h^2\Omega_{\text{turb}}. \quad (4.39)$$

Each components is scaled by its own unique efficiency factor, κ . The three leading order contributions to the GW power spectrum are as follows:

- **Scalar field contributions** Ω_ϕ : Caused by collisions of the bubble walls, the solutions being completely dependent on the scalar field configuration, with efficiency factor $\kappa_\phi = 1 - \alpha_\infty/\alpha$ [123, 124].
- **Sound wave contributions** Ω_v : Sound waves within the plasma after bubble collision will produce β/H enhanced gravitational waves, with efficiency factor $\kappa_v \propto \alpha_\infty/\alpha$ [125].
- **Magnetohydrodynamical contributions** Ω_B : Turbulence within the plasma, left over from the sound wave propagation, will produce gravitational waves with

efficiency factor $\kappa_{turb} \approx 0.1\kappa_v$ [126].

The parameter α_∞ denotes the dividing line between the runaway regime ($\alpha > \alpha_\infty$) and the non-runaway regime ($\alpha < \alpha_\infty$). Explicitly [80, 94, 121],

$$\alpha_\infty = \frac{(T_h^{nuc})^2}{\rho_R} \left[\sum_{bosons} n_i \frac{\Delta m_i^2}{24} + \sum_{fermions} n_i \frac{\Delta m_i^2}{48} \right], \quad (4.40)$$

for particles with n_i degrees of freedom that obtain mass through the phase transition.

The exotic sectors have essentially massless degrees of freedom pre-phase transition and pions with negligible masses post-phase transition. Other composite particles, such as baryons, do gain a mass of the order of Λ_{ex} ; this is, however, still much smaller than the order of ρ_R leading to small α_∞ according to Eq. (4.40).⁴ Heavy standard sectors that undergo SFOPT for QCD feature no baryons due to all quarks being above their respective QCD scales. They do, however, feature glueballs that obtain a mass of the order of the SFOPT and, just as in the case for exotic sectors above, feature small α_∞ .

Each component of the spectral energy density in Eq. (4.38) is proportional to a power of their respective efficiency factors κ . The relative strength of the efficiency factors is dependent on the ratio $\frac{\alpha_\infty}{\alpha}$ — since both α_∞ and α are parameterically small [40, 96], a range of possible scenarios can occur. Here, we discuss the two ends of this spectrum: pure runaway walls and pure non-runaway walls. The former scenario with runaway bubble walls leads to the efficiency factors for the sound wave and MHD contributions being small and ensures GWs are dominantly produced from bubble collisions, $h^2\Omega_{GW} \approx h^2\Omega_\phi$: this is what we assume for the remainder of this section. In the latter case, bubbles are non-runaway (but $v_w \sim 1$ still [94, 127])

⁴It should also be noted that although free quarks cease to exist post phase transition in these exotic sectors, their masses are so light that they do not contribute relevant amounts to α_∞ .

such that non-bubble collision contributions being important — ultimately leading to significant changes to the GW profile. This case and the gravitational waves it produces are examined in the appendix. Intermediate results are of course possible, and would feature profiles somewhere in between the two extremes.

The form of the GW energy density at the time of nucleation is given by [94],

$$h^2\Omega_{\text{GW}}^* = 7.7 \times 10^{-2} \left(\frac{\kappa_\phi \alpha}{1 + \alpha} \right)^2 \left(\frac{H}{\beta} \right)^2 S(f) \quad (4.41)$$

where we use $v = 1$ for runaway bubbles. Quantities such as Ω_{GW}^* that are calculated at the time of nucleation are denoted with an asterisk, and they must then be evolved to relate to their values at the time of observation. $S(f)$ is the spectral shape function for the signal and a parametric form has been found through numerical simulations [124] of bubble wall collisions:

$$S(f) = \frac{3.8 (f/f_p)^{2.8}}{1 + 2.8 (f/f_p)^{3.8}}. \quad (4.42)$$

The peak frequency, f_p is a function of the temperature of the SM at the time of nucleation. The various hidden sectors can phase transition at different scales and therefore temperatures, causing a shift in the GW spectrum's peak frequency given by [124],

$$f_p = 3.8 \times 10^{-8} \text{ Hz} \left(\frac{\beta}{H} \right) \left(\frac{T_\gamma}{100 \text{ GeV}} \right) \left(\frac{g_*}{100} \right)^{\frac{1}{6}}, \quad (4.43)$$

where g_* is calculated using Eq. (4.34), although, due to the lack of substantial reheating into the hidden sectors, the SM contribution is dominant.

Now that the framework has been laid out for the creation of GW from a single SFOPT, we generalize to multiple sectors going under independent, coherent SFOPT. In the models presented in this paper, we consider a subset of N hidden sectors that

undergo a phase transition at a SM temperature of T_γ^i . As the GWs propagate in free space, the energy density and frequency spectrum, at the time of production $\Omega_{\text{GW}}^*(f)$, will redshift to today's value $\Omega_{\text{GW}}^0(f) = \mathcal{A} \Omega_{\text{GW}}^*((a_0/a)f)$. The redshifting factor, \mathcal{A} , accounts for the redshifting of both ρ_{GW} and ρ_c [94, 128],

$$\mathcal{A} \equiv \left(\frac{a}{a_0}\right)^4 \left(\frac{H}{H_0}\right)^2 \quad (4.44)$$

where a (a_0) and H (H_0) are the scale factor and Hubble constant at the time of nucleation (observation), respectively. Assuming that the sectors are completely decoupled before and after their respective SFOPT, the total GW signal that would be measured today is given by the coherent sum,

$$\Omega_{\text{GW}} = \sum_i^N \mathcal{A}^i \Omega_{\text{GW}}^{i,*}((a_0/a)_i f). \quad (4.45)$$

We assume that the parameters of the SFOPT do not differ between sectors: the relativistic degrees of freedom, phase transition rate, and the dark QCD scale, are all similar. This makes the redshifting factor \mathcal{A}^i independent of sector number. Applying this to the standard reheating scenario of N natrualness, introduced in 4.4, we get GW signals as seen in Fig. 4.1. Plotted are the individual contributions to the signal from each phase transitioned sector, as well as the coherent sum of all sectors. Future GW interferometers and pulsar timing array sensitivity curves are shown in comparison to the signal. The sensitivity curves are interpreted as the region of possible detection if intersected with the GW signal, and the construction of these curves is detailed in Section 4.6.2. Notice that the total signal is dominated by the first sector's contribution. This is caused by the quartic temperature ratio suppression in Eq. (4.33) and the large temperature gaps between adjacent sectors. Such a sup-

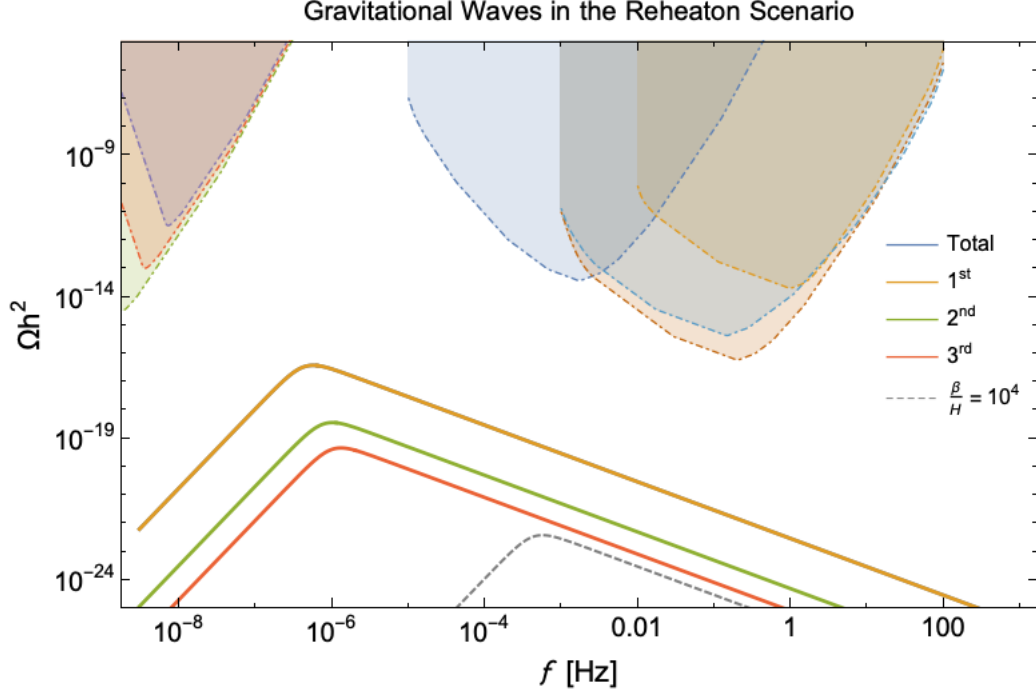


Figure 4.1: Gravitational wave spectral energy density (solid curves) for standard N naturalness using the scalar reheaton model of section 4.4. The curve corresponding to the sum of the sectors is approximately equal to the $i = 1$ curve. All contributions are assumed to be purely from bubble collisions Ω_ϕ . The colored solid lines use $\beta/H = 10$ where as the dashed gray line is the total contribution of all sectors for $\beta/H = 10^4$ (the sum of all sectors is roughly equal to the $i = 1$ curve and sectors beyond the first are below the range of this plot). The shaded dashed curves are the power law noise curves [129] calculated from expected sensitivity as described in Section 4.6.2. The ones on the right are space-based interferometers: Lisa [72] (blue), DECIGO [75] (light blue), BBO [69] (red). The ones on the left are for the pulsar timing array SKA [71] for exposure time of 5-years (purple), 10-years (orange), and 20-years (green).

pression leads to standard N aturalness evading future detector thresholds by a few orders of magnitude in units of energy density.

This is not the case if we consider more generalized reheating scenarios. Once the restriction that sectors with small Higgs masses are preferentially reheated has been lifted, we can explore a much more vast landscape of hidden sectors than are allowed in the reheaton case. Here, we construct several different scenarios that are

both detectable and demonstrate a variety of gravitational wave profiles. Specifically, we explore benchmarks that lead to a deviation in the peak behaviour of the total GW signal (the superposition of stochastic GW from individual SFOPT) from a standard power law signal.

It should be noted that the key phenomenological constraint on all of these models is ΔN_{eff} , giving us a maximum allowed temperature ratio (when compared to the SM) for each reheated hidden sector: Eq. (4.31) shows the maximum temperature ratios for specific numbers of additional hidden sectors. Due to the rather harsh scaling of the GW strength, α , with temperature ratio shown in Eq. (4.35), we take the optimistic approach of keeping the temperature ratio as high as allowed by CMB data for all of the hidden sectors.

In the following, we focus on heavy standard sectors — pure Yang-Mills sectors with much heavier particles (specifically quarks) and, as shown in Sec. 4.3, the SFOPT these entail. The reason for this arises from Eq. (4.43): every exotic sector features a phase transition that occurs at $\Lambda_{ex} \sim 90$ MeV. If we maximize the allowed temperature ratio, this gives us a (SM) photon temperature, T_γ , that places our signal directly in the frequency void between the detection region of pulsar timing arrays and space-based interferometers (see Sec. 4.6.2). The location of the peak can be changed by dropping the temperature ratio, but the adjustment required to end up with a signal with an appropriate peak frequency makes the overall signal too weak to detect. As shown in Sec. 4.3, standard sectors can have much higher temperature phase transitions. As such, maintaining the maximum allowed temperature ratio between the hidden sector(s) and the SM gives a much larger photon temperature and a proportionally larger peak frequency; ultimately allowing for detection by space-based interferometers.

Parameters for multi-hidden sector benchmarks				
Maximized signal				
Sector	Higgs vev (GeV)	Λ_{QCD}^{AS} (GeV)	T_γ (GeV)	Index
1	24.6×10^9	38.6	87.7	10^{16}
Large split				
Sector	Higgs vev (GeV)	Λ_{QCD}^{AS} (GeV)	T_γ (GeV)	Index
1	246×10^6	10.8	30.3	10^{12}
2	7.8×10^9	28.1	78.6	10^{15}
Medium split				
Sector	Higgs vev (GeV)	Λ_{QCD}^{AS} (GeV)	T_γ (GeV)	Index
1	246×10^6	10.8	30.3	10^{12}
2	778×10^6	14.9	41.6	10^{13}
Five sector				
Sector	Higgs vev (GeV)	Λ_{QCD}^{AS} (GeV)	T_γ (GeV)	Index
1	246×10^6	10.8	38.8	10^{12}
2	426×10^6	12.6	45.2	3×10^{12}
3	778×10^6	14.9	53.3	10^{13}
4	1.3×10^9	17.3	62.1	3×10^{13}
5	2.5×10^9	20.5	73.3	10^{14}

Table 4.1: Outline of parameters used for the various multi-hidden sector scenarios. The higgs vev is the vev for the given additional sector, Λ_{QCD}^{AS} is the QCD phase transition in the additional sector, and T_γ is the temperature of the SM photon bath when the SFOPT occurs in the additional sector. The index indicates the equivalent sector from the N naturalness model (Eq. (4.4)). It should be noted that although the various sectors undergo phase transitions at different temperatures, they are all assumed to be reheated to the same initial temperature.

There are four scenarios that we examine, with key parameters presented in Tab. 4.1.

- **Maximized signal:** A single additional heavy hidden sector reheated to a temperature that saturates current experimental bounds. The SM photon bath temperature at the time of the hidden sector PT is 87 GeV. In the N naturalness framework this is equivalent to reheating a standard sector with $i \sim 10^{16}$ up to the maximum allowed temperature ratio.

- **Large split scenario:** A scenario where two additional hidden sectors have been reheated — these sectors have Higgs vevs that are split by a factor of

$$\frac{v_{h1}}{v_{h2}} = \sqrt{10^3}. \quad (4.46)$$

This results in a difference in the scale of the SFOPTs leading to the SM photon bath temperature changing a large amount during the time between the PTs. This, in turn, leads to a large separation in the peak frequency of their gravitational wave signals. In the N naturalness framework this is equivalent to reheating two standard sectors, one with $i \sim 10^{12}$ and another with $i \sim 10^{15}$ up to the maximum allowed temperature ratio.

- **Medium split scenario:** Similar to the previous case: these sectors have Higgs vevs that are split by a factor of

$$\frac{v_{h1}}{v_{h2}} = \sqrt{10}, \quad (4.47)$$

resulting in a much smaller difference in the peak frequency of their gravitational wave signals. In the N naturalness framework this is equivalent to reheating two standard sectors, one with $i \sim 10^{12}$ and another with $i \sim 10^{13}$ up to the maximum allowed temperature ratio.

- **Five sector scenario:** Five sectors are reheated to the maximum allowed temperature ratio, each with vevs that are

$$(v_{hi})/(v_{h(i+1)}) \sim \sqrt{3} \quad (4.48)$$

larger than the previous sector.

In all cases where multiple sectors are reheated, we assume for simplicity that all the hidden sectors are reheated to the same temperature.

The GW results of these cases are presented in Fig. 4.2. In all cases, the summed GW signal is detectable by one or more proposed interferometers. When changing the assumptions on β/H , the scenarios in Fig. 4.2 are still detectable for values ranging between $\mathcal{O}(1)$ and $\mathcal{O}(100)$. As β/H increases (decreases) the peak frequency moves to higher (lower) frequencies, dictated by Eq. (4.43), where as the amplitude decreases (increases) shown in Eq. (4.41).

The frequency dependence in Eq. (4.42) takes the form of f/f_p , this causes a cancellation between the redshifting factors. As multiple sectors phase transition at different times, and therefore different SM photon temperatures, the peaks will shift relative to each other, purely from the linear temperature dependence of the peak frequency $f_p \sim T_\gamma$ given in Eq. (4.43). This is seen in Fig. 4.2, where the spectrum peaks are shifted causing a peak broadening of the summed spectrum. The broadening can be substantial if the hidden sectors transition between a large gap of time (temperature). Eventually, a temperature limit will be reached where two (or multiple) distinct peaks will be visible, provided that the amplitudes are comparable.

4.6.2 Detection of Stochastic Gravitational Waves

A *stochastic* gravitational wave background could be detectable if the signal-to-noise ratio (SNR) is above some threshold value, $\rho > \rho_{th}$, dictated by the capabilities of future interferometers and pulsar timing arrays (PTA). These interferometers/PTAs quote their experimental sensitivities in terms of spectral noise curves, $S_{\text{eff}}(f)$, which can be translated into units of energy density through $h^2\Omega_{\text{eff}}(f) = \frac{2\pi^2}{3H^2}f^3S_{\text{eff}}(f)$. If the experiment uses a single (multiple) detector, the auto-correlated (cross-correlated)

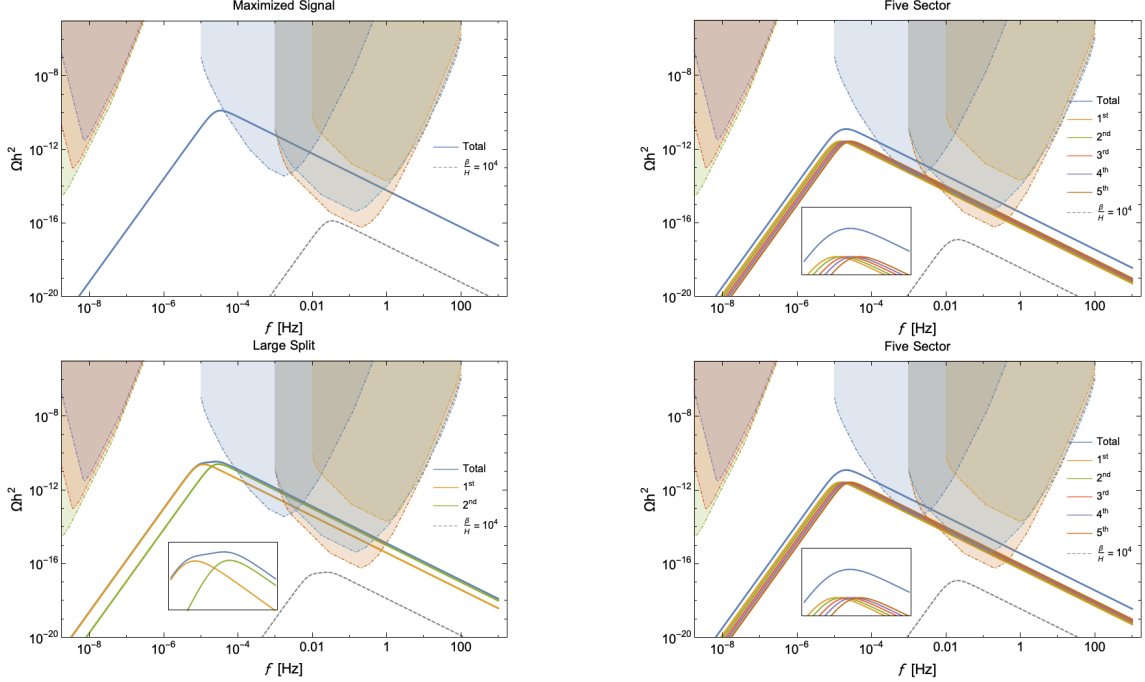


Figure 4.2: Gravitational wave spectral energy density for the various scenarios found in Tab. (4.1). All contributions are assumed to be purely from runaway bubble collisions Ω_ϕ . The colored solid lines use $\beta/H = 10$ where as the dashed gray line is the total contribution of all sectors for $\beta/H = 10^4$. The inset is a closer look at the region around the peaks for the $\beta/H = 10$ case. The shaded curves are the same as Fig. 4.1.

SNR is used in comparing to the threshold value ρ_{th} . The auto-correlated and cross-correlated SNR are explicitly given as [130],

$$\begin{aligned}
 \rho^2 &= \mathcal{T} \int_{f_{\min}}^{f_{\max}} df \left(\frac{h^2 \Omega_{\text{GW}}(f)}{h^2 \Omega_{\text{eff}}(f)} \right)^2 && \text{(auto-correlated)} \\
 \rho^2 &= 2\mathcal{T} \int_{f_{\min}}^{f_{\max}} df \left(\frac{h^2 \Omega_{\text{GW}}(f)}{h^2 \Omega_{\text{eff}}(f)} \right)^2 && \text{(cross-correlated)},
 \end{aligned} \tag{4.49}$$

where \mathcal{T} is the exposure time of the experiment. The integration covers the entire broadband range of frequencies (f_{\min}, f_{\max}). LISA [72] and B-DEICIGO [75] are proposed to be single detector interferometers, where as BBO [69] and DEICIGO [74] would be built from an array of multiple interferometers. GW signals produced from

an early cosmological phase transition would be seen as a stochastic background. Assuming that the GW follows a power law background in frequency, it is commonplace to quote the power law integrated (PLI) sensitivity curves [129]. The PLI curves are constructed using information from the power law form of the signal,

$$h^2\Omega_{\text{GW}}(f) = h^2\Omega_\gamma \left(\frac{f}{f_{\text{ref}}} \right)^\gamma \quad (4.50)$$

where γ is the spectral index of the power law, and f_{ref} is an arbitrary reference frequency which has no effect on the PLI sensitivities. $h^2\Omega_\gamma$ is the energy density calculated using Eq. (4.49) with spectral index γ and reference frequency f_{ref} . The method of calculating the PLI curves involves plotting $h^2\Omega_{\text{GW}}(f)$, using Eq. (4.50), for various spectral indices γ and for some fixed threshold value of ρ_{th} . Each curve will lay tangent to the PLI curve, more formally,

$$h^2\Omega_{\text{PLI}} = \max_\gamma \left[h^2\Omega_\gamma \left(\frac{f}{f_{\text{ref}}} \right)^\gamma \right]. \quad (4.51)$$

The spectral noise curves used to create the PLI curves shown in Figs. 4.1 and 4.2 were taken from [75, 94, 131–133] for the interferometers, and [71, 94] for the square kilometre array (SKA) pulsar timing array. We have assumed an observation time of $\mathcal{T} = 4$ years for the interferometers and $\mathcal{T} = 5, 10, 20$ years for the various stages of SKA. In the case of the PTA experiments, the sensitivity curves are dependent on how frequently the pulsar’s timing residuals, δt , are measured. When using Eq. (4.49) to construct the PLI curves for SKA, the upper integration bound is inversely proportional to pulsar’s timing residual, $f_{min} = 1/\delta t$. In this work, it is assumed that $\delta t = 14$ days, but this may underestimate the capabilities of SKA as well as the cadences of the pulsar populations. If the timing residuals are lowered the maximum

frequency reach of SKA increases, and the corresponding PLI curves in Figs. 4.1 & 4.2 are shifted to the right, possibly giving the PTAs sensitivity to some of the scenarios considered here.

4.7 Conclusion

As detection capabilities increase, gravitational wave signals continue to grow in importance as phenomenological signatures that can offer us a unique glimpse into the universe as it was in the early epochs. The space-based interferometers planned for the next generation of GW experiments will be sensitive enough to begin searching for signals of the cataclysmic disruption of space-time due to SFOPT. As we inch closer to these measurements becoming available, it becomes important to develop ways to analyze and understand this data.

Here, we examined scenarios, including N naturalness, that involve multiple hidden sectors and calculated the GW profiles present. Our GW projections demonstrate that although N naturalness with the reheaton scenario presented in [41] is not projected to be detectable in the near future, more generalized scenarios with multiple hidden sector SFOPTs are in an observable region and will begin to be probed by next generation space experiments. Both cases feature important parts of their GW signals in the void between frequencies detectable by pulsar timing arrays and space-based interferometers — providing theoretical impetus for new experiments capable of probing this region of frequency space.

Further, our results provide a framework for understanding and using GW signals in two different ways: first as a unique signal for specific theories featuring multiple SFOPTs and also as a challenge to broaden the understanding of GW detector sensitivity.

In the former case, this demonstrates the power of GW signals to probe deep into the unknown arena of complex hidden sectors. Individual SFOPT are understood to create GW that are assumed to follow an approximate power law. If a model predicts the presence of 2, 5, or more additional sectors, or features a single extra sector with multiple PTs, deviations from a standard power law can occur. The multiple transitions that occur in the models outlined here create signals that follow this trend: although the individual GW do obey approximate power laws, their sum does not — leading to a unique signal indicating so-called dark complexity. Explicitly, a broadening or distortion of the signal around the peak frequency, precisely where the signal has the most energy, could point to a multi-SFOPT scenario and gently guide us in the direction of multiple hidden sectors.

Shifting to the other part of our framework, our results leads to the question “how well can experiments probe non power law signals?” For frequency ranges away from the peak of the total, GW signals the quoted detection thresholds should hold: the signals fall off as a power law to a very good approximation. However, for areas around the peak frequency the answer is less clear; the PLI curves are built under the assumption of a power law. Work has been done [134] in examining GW signals using peak amplitudes and peak frequencies as the defining observables: this is rooted in the assumption that GW signals have a model-independent spectral shape around peak frequencies. However, our results indicate that this assumption of model-independence cannot hold for all cases: sectors with similar (but different) transition temperatures can create either peak broadening or multi-hump features that differ significantly from a standard power law shape. This points to the need for future work to better understand where the power law approximation breaks down and how this affects detection prospects for the next generation of GW detectors.

Chapter 5

Triggering on Emerging Jets

*“In critical moments, people sometimes see
exactly what they wish to see.”*

— *Mr. Spock*

5.1 Introduction

Confining hidden sectors with a confinement scale around the GeV scale have received significant attention for potential discovery at colliders [29, 52, 135–140] (for a recent review, see chapter 7 of [141]), building on the seminal hidden valley work [26, 142, 143]. Besides providing interesting signatures at colliders, they can also be motivated by asymmetric dark matter [28, 144, 145] and by neutral naturalness [146–149]. This has led to several phenomenological studies at the LHC [53, 150–152], flavour experiments [153], and future proposed experiments [154, 155]. There is also an experimental search [156] that puts direct limits on certain regions of parameter space.

If the dark confining sector has a mediator to the SM whose mass is much larger than the confining scale, then the lifetime of the lightest dark hadrons that are not stable will be parametrically larger than their inverse mass. One particularly inter-

esting region of parameter space is where the lifetime of the decaying dark hadrons is in the mm–m range, leading to spectacular signatures at the LHC’s detectors [29]. For example, if the dark gauge group is QCD-like, then when dark quarks are produced, they will shower and hadronize, producing dark jets. This is analogous to the production of ordinary quarks at a high energy lepton collider which then produce SM jets. Each of the dark hadrons will decay at a different position in the detector, and the energy of the dark jet will “emerge” into the detector. This signature was thus termed an emerging jet [29]. At distances long compared with the typical $c\tau$ of the dark hadrons, the dark jet will look like a QCD-jet.

Motivated by the asymmetric dark matter scenario of [28], the work [29] considered a scalar mediator X that is charged under QCD and dark-QCD. That means that the dominant collider signal will be pair production of the mediator, and each collider event will contain two emerging jets and two SM jets. This is also the scenario experimentally constrained in [156]. Another well motivated possibility is the one considered in the original hidden valley literature [26, 142, 143]: a vector mediator Z' that couples to both quark and dark quark currents. A third possibility, the one expected in the neutral naturalness scenarios [146–149], is the SM Higgs or another scalar as the mediator (H) to the dark sector. In both of the latter cases, we see two important differences between the original case of the X :

- The production cross section of dark hadrons is a free parameter and not set by pair production via SM QCD.
- The production, at leading order, does not include the associated production of SM jets in the hard event.

These cases are therefore more challenging experimentally.

A particularly important challenge with exotic signatures at the LHC is triggering. The event rate at the LHC is extremely high, and a trigger is employed to reduce the event rate by several orders of magnitude and attempt to record all the events of interest. The triggers were designed to be extremely efficient on many types of events and new physics models, but they are not designed for more exotic scenarios such as emerging jets. In the case of the X mediator, if its mass is $\mathcal{O}(\text{TeV})$, then the associated jets in combination with the very high total energy in the event makes triggering relatively straightforward.

In this work we study the significantly more difficult case of triggering on the Z' mediator, focusing on the relatively lower mass regime, $M_{Z'} \sim 100 \text{ GeV} - 1 \text{ TeV}$. We will take a two-pronged approach. First, we will consider how well current triggers can capture these events, and explore how the addition of initial state radiation can increase the efficiency. Using ISR to leverage an experimental search is now a commonplace strategy for various searches for new physics, with phenomenological analyses for supersymmetric models [157–160] going back nearly forty years. This strategy has also been used to search for model independent effective operators [161–163], and it is colloquially known as the mono- X strategy. Experiments at the LHC have used the presence of a single high transverse momentum associated objects to search for various new physics models. Initially, these methods focused on effective models [164, 165], and they are now used extensively to search for invisible states. A broad range of recent examples include mono-jet [166], mono-photon [167], mono- W and mono- Z [168], placing constraints on many different types of models. In this work we show that both QCD and electroweak radiation can increase the trigger efficiency and increase the total number of events recorded, but ultimately QCD will lead to a higher rate than electroweak radiation.

The second strategy we employ is to consider new triggers using modern machine learning (ML) techniques. The landscape of machine learning applications within particle physics is becoming ever broader and more complex. Its utilities ranges from substructure classifications [169], such as jet discrimination [170, 171], adjustments to particle flow algorithms using images of calorimeter responses [172], to multivariate analysis techniques explored at both CMS and ATLAS as the LHC moves towards the energy and intensity frontiers. [173, 174]. We look to investigate novel triggers based on simple machine learning methods that can be applied to the triggering stream. Complementary studies include [175] where a deep neural-net (DNN) is implemented at L1 resulting in high trigger efficiencies for a HL-LHC 15 KHz target output, as well as the study of a more traditional trigger for displaced vertices [176]. CMS (ATLAS) has been conducting analyses of this type on low level information reconstructed from the triggering stream under the guise of Data scouting (Online trigger analysis) [177–179].

One possible downside in the use of ML techniques in particle physics is that we might not understand the unique physical features that the algorithm is converging on [180]. We can easily use these methods as a black box while taking for granted the physical insight we might be losing out on. Some work has been done to try to mine features in these black boxes [181]. This is a significantly less important problem when considering triggers where the most important task is to get interesting events recorded quickly. Emerging jets contain complex dark substructures between the invisible dark sector hadrons and the visible SM particles they decay into. The question of *what aspect of the dark substructure is the machine learning?* for example, to distinguish signal from background, is irrelevant in-situ. The dataset, once written offline, can be pruned for features using more modern “human readable”

methods [182]. With that in mind, all use of ML methods in this paper will take a pragmatic approach, where we focus on writing as many interesting events onto record with little regard for physical insight.

in this work, we use hits in the tracker as input into a potential new trigger discriminator. Tracking is traditionally not used in triggering because track reconstruction is too computationally time consuming [183,184]. We skirt this problem by not reconstructing tracks, but rather by simply counting hits in a region of the detector. This is similar to the strategy proposed in [185] for b -tagging. This technique can be effective in distinguishing emerging jets because the dark sector particles will not leave hits but their decay products will. Therefore, if the dark sector particles lifetime $c\tau \sim \text{mm} - \text{m}$, an emerging jet will have increasing numbers of hits in detector layers further from the interaction point. QCD jets, on the other hand, will typically have the same number of hits in most layers because unstable SM hadrons will typically decay before hitting the first or second layer of the detector, with the exception of a few strange mesons. We will show that this type of observable fed into a machine learning algorithm can be an effective trigger for a wide class of model parameters. We also explore the universality of such strategies and show that a trigger trained on one parameter point can be sensitive to a broad swath of parameter space.

The remainder of this paper is structured as follows: in Section 5.2 we describe the concrete model we use for our analysis, and in Section 5.3 we describe our simulation pipeline. In Section 5.4 we describe how the mono- X strategy can be used to improve event collection with current triggers, and in Section 5.5 we outline how new triggers can also be used to explore new parameter space. Conclusions are given in Section 5.6.

5.2 Models for emerging jets

The study of generic hidden sectors at the LHC is an interesting and important question. For concreteness we will specify a class of models and leave the more general case to future work. We consider an $SU(N_d)$ gauge group with confinement scale $\Lambda_d \simeq$ GeV and n_f flavours of vectorlike quarks with masses below confinement scale. The dark quarks are singlets under all SM gauge groups. If there is an accidental baryon number symmetry analogous to QCD, then the baryons of this sector could be dark matter [28].

Unlike previous work which studied a scalar mediator [29], we consider a vector mediator, Z'_μ as in some of the original hidden valley literature [26], whose mass M is larger than the dark confinement scale, $M \gg \Lambda_d$. This is the simplest s -channel mediator to the hidden sector, and can be thought of as a simplified model to parametrize more general mediator models. The UV theory and mechanism to give mass to the Z' is left unspecified, but we assume the additional states needed to not affect the emerging jet phenomenology. This assumption is justified by the separation of scales: the UV physics of the Z' is expected to be around the mass of the Z' and can easily be made heavier, while the emerging jet phenomenology is characterized by the scale Λ_d which, as noted above, is small compared to the Z' mass.

This mediator couples to the quark and dark quark currents:

$$\mathcal{L} \supset \frac{1}{2} M^2 Z'^\mu Z'_\mu + Z'^\mu (g_q \bar{q} \gamma_\mu q + g_d \kappa_{ij} \bar{Q}_i \gamma_\mu Q_j), \quad (5.1)$$

where q are SM quarks, Q are dark quarks, and $g_{q/d}$ are coupling constants. The matrix κ_{ij} is $n_f \times n_f$ and introduced to break the $SU(n_f)$ hidden flavour symmetry which would otherwise stabilize some of the dark pions. We do assume flavour uni-

versality for the coupling to SM quarks to avoid bounds from flavour physics, and SM flavour indices are summed and not written. The Z' is a singlet under SM and unbroken dark gauge groups, so gauge indices among the quarks and dark quarks are contracted in the standard way.

This model contains a rich spectrum of dark hadrons, with a multiplet of dark pions, π_d expected to be the lightest. All heavier mesons have a lifetime of order Λ_d^{-1} and decay to dark pions if kinematically allowed (i.e. $\rho \rightarrow \pi\pi$ in the SM). Dark baryons in these models are often very long lived. In the parameter regions we consider, dark pions are significantly lighter than dark baryons (as in QCD) and thus are typically produced in much larger abundances than dark baryons. This can be confirmed with SM data [186] as well as a large N_c expansion [187] of QCD. Therefore we ignore the effects of dark baryons in this study, but of course these assumptions can be violated if the hadron spectrum is significantly different from that of the SM.

For simplicity, we take a common mass of the dark pions, m_{π_d} , and we assume there are no large hierarchies between the entries in the κ matrix. These assumptions allow us to consider a common lifetime for all the dark pions, but for a study of non-trivial dark flavour dynamics, see [153]. The Z' mediates a decay of the dark pions that can be computed using dark chiral perturbation theory with a width given by

$$\Gamma(\pi_d \rightarrow \bar{q}q) \approx \sum_q \frac{g_q^2 g_d^2 N_c m_q^2 f_{\pi_d}^2}{32 \pi M^4} m_{\pi_d} \quad (5.2)$$

where $N_c = 3$ is the number of SM colours, f_{π_d} is the dark pion decay constant which we take to be $\sim \Lambda_d$, and m_q is the mass of the SM quark in the final state. Here and in the formulas in the remainder of this section, we have assumed that the entries in the κ matrix are $\mathcal{O}(1)$ and can be ignored for a leading order estimate. The sum is over all SM quarks that are kinematically accessible, and we have ignored phase

space effects, but they can be trivially added. The factor of m_q^2 is a spin-parity affect analogous to the decay of the charged pion in the SM, implying that the decay will be dominated by the heaviest quark kinematically accessible. We can estimate the proper decay length for a benchmark pion mass of 2 GeV:

$$c\tau_0 \approx 80 \text{ mm} \times \frac{1}{g_d^2 g_q^2} \times \left(\frac{2 \text{ GeV}}{f_{\pi_d}} \right)^2 \times \left(\frac{100 \text{ MeV}}{m_q} \right)^2 \left(\frac{2 \text{ GeV}}{m_{\pi_d}} \right) \left(\frac{M_{Z'}}{1 \text{ TeV}} \right)^4. \quad (5.3)$$

which we see can be macroscopic but smaller than the size of an LHC detector for a wide range of parameter space.

Dark quarks (and thus dark jets) are produced at colliders like the LHC via an s -channel Z' . If kinematically accessible, resonant production where the Z' is on shell will dominate the production. The lowest order cross section for this production process at a proton-proton collider is

$$\begin{aligned} \sigma(pp \rightarrow Z' \rightarrow Q\bar{Q}) &= \sum_{f=u,d} \int dx_1 f_f(x_1) \int dx_2 f_f(x_2) \\ &\times \frac{g_d^2 g_q^2}{72\pi} \left(\frac{x_1 x_2 s}{(x_1 x_2 s - M_{Z'}^2)^2 + \Gamma^2 M_{Z'}^2} \right). \end{aligned} \quad (5.4)$$

Where $f_i(x_i)$ is the parton distribution function for fermion i and momentum fraction x_i . The Mandelstam variable s is set to the centre of mass energy $\sqrt{s} = 13 \text{ TeV}$. The total decay width of the Z' is given by Γ , which has two contributions $Z' \rightarrow q_i \bar{q}_i$ and $Z' \rightarrow Q_i \bar{Q}_i$,

$$\Gamma(Z' \rightarrow X\bar{X}) \simeq \frac{N n g^2 M_{Z'}}{24\pi} \quad (5.5)$$

where for X being a SM (dark) quark, N is the number of (dark) colours which we take to be 3, n is the number of accessible flavours, and g is the coupling to (dark) quarks. We have ignored kinematic factors which are only important if the Z' is

approximately degenerate with a pair of (dark) quarks.

From these equations, assuming resonant production is dominant, we can show that to leading order the cross section for the process $q\bar{q} \rightarrow Z' \rightarrow Q\bar{Q}$ depends only on the mass of the Z' and the variable

$$\eta^2 \equiv \frac{g_d^2 \cdot g_q^2}{g_d^2 + \left(\frac{n_f}{n_d}\right)g_q^2}, \quad (5.6)$$

scaling linearly with η^2 . We have assumed the number of dark colours is also 3. The production cross section at a centre of mass energy $\sqrt{s} = 13$ TeV is shown in Fig. 5.1 as a function of mass for a couple of benchmark values of η^2 . We see that number of such events at the LHC with an integrated luminosity $\sim 100 - 3,000 \text{ fb}^{-1}$ can be very large.

Alongside the LO contribution to the Z' production are higher order terms from initial state radiation (ISR) coming off of the incoming quark lines. In Fig. 5.2 we show this for QCD gluon radiation. These gluons will hadronize into additional hard QCD jets affecting the overall event topology. ISR is not exclusive to QCD, the quarks may radiate a hard W , Z or photon. These ISR contributions have a smaller rate than the leading order process, but they can be easier to detect experimentally.

Independent of ISR, the choice of portal to the hidden sector can add stringent constraints on the mediator from collider and direct detection experiments [152], as was seen for the scalar mediator case explored in [29]. In our case, these Z' portals are of interest for detector searches because of the freedom in the production cross section of dark hadrons parameterized by the couplings to both the SM and the hidden sector $g_{q/d}$. This portal, however, does have resonant dijet production proportional to g_q^4 which can place constraints [188–190]. Most studies at modern collider experiments are only sensitive to the higher mass regime $M_{Z'} > 1$ TeV, but some searches have

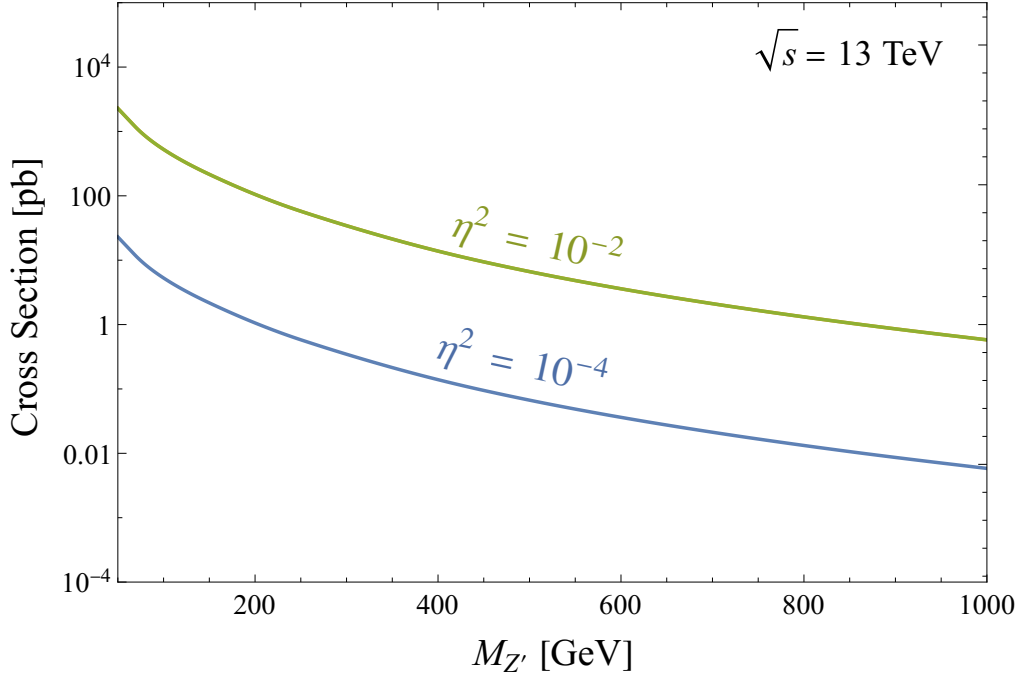


Figure 5.1: Cross section of $pp \rightarrow Z' \rightarrow Q\bar{Q}$ for a leptophobic Z' as a function of its mass $M_{Z'}$. Generated by convolving the partonic cross sections of u, d -quarks with their respective parton distribution functions at a centre of mass energy of $\sqrt{s} = 13$ TeV. η is a function of the Z' Lagrangian parameters defined in Eq. (5.6).

employed in-situ analysis to probe lower masses [191, 192]. Typical upper bounds at the lower mass regime are $g_q \lesssim 0.1$. We do demand that the dark mesons have lifetimes between 1mm - 1000m. Doing so puts additional constraints on the product of couplings $g_d \cdot g_q$ from Eq. (5.1). Assuming lower mediator masses, dark pion masses, and decay constant at $\mathcal{O}(\text{GeV})$, emerging jet events with displaced vertices are consistent with $g_d \cdot g_q \lesssim 0.2$.

For the rest of this work, we take $c\tau$ to be a free parameter. The mass of the Z' and $c\tau$ are related by Eq. (5.3), but there are enough parameters in the models such that we can tune each variable independently. Therefore we vary the mass of the Z' as it broadly controls the total energy in the event. For the dark QCD parameters,

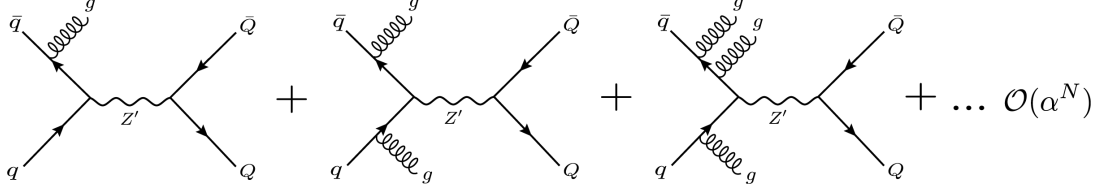


Figure 5.2: Higher order QCD initial state radiation diagrams of $q\bar{q}$ induced Z' resonant production. Gluons are radiated from the quark lines in the form of detectable hard QCD jets. EW splittings are also possible with diagrams scaling with the EW couplings.

Model	A	B	C	D	E	F
Λ_d	10 GeV	4 GeV	10 GeV	10 GeV	10 GeV	20 GeV
m_V	20 GeV	8 GeV	20 GeV	20 GeV	20 GeV	40 GeV
m_{π_d}	5 GeV	2 GeV	5 GeV	5 GeV	5 GeV	10 GeV
$c\tau_{\pi_d}$	150 mm	5 mm	50 mm	500 mm	5 mm	500 mm

Table 5.1: Dark sector parameters for our benchmark models. Λ_d is the dark confinement scale, m_V is the mass of the dark vector mesons, and m_{π_d} is the pseudo-scalar mass. $c\tau_{\pi_d}$ is the rest frame decay length of the pseudo-scalars. We take $N_c = 3$ and $n_f = 7$ in both benchmarks. Models **A** and **B** are considered in Section 5.4, while Models **A**, **C**, **D**, **E** and **F** are considered in Section 5.5.

we use six benchmark parameter points shown in Table 5.1. The first two, Model **A** and Model **B**, have different dark pion masses of 2 GeV and 5 GeV and 2 different lifetimes of 5 mm and 150 mm, respectively. These models are used in studying current triggers in Section 5.4.¹ Models **C**, **D** and **E**, are identical to Model **A** but with lifetimes ranging from 5mm to 500 mm. Model **F** has the same lifetime as Model **D** but a heavier hadron spectrum. Models **A**, **C**, **D**, **E** and **F** are considered in the machine learning trigger analysis of Section 5.5.

5.3 Event generation

Here we describe our simulation pipeline to generate Monte Carlo events for the models described in the previous section. The events were generated using a modified

¹These were also the benchmarks used in [29].

spin-1 mediator model² [137] implemented using the `FeynRules` [193] package. The model is outputted as a UFO [194] file which allows generation of hard processes with `Madgraph5_aMC@NLO` [195], and we use LHC conditions with a centre of mass energy of 13 TeV. This output is interfaced to the Hidden Valley [47, 196] module of `Pythia8` [46], which simulates showering and hadronization in the dark sector as well as decays of dark hadrons to either other dark hadrons or to SM states. Initial state radiation (ISR) in QCD or EW, i.e jets, leptons and EW gauge bosons, are included at leading order in the hard processes in `Madgraph5_aMC@NLO`, and we use `Pythia8` to shower and hadronize SM quarks. The resulting hadrons are clustered into jets using the Anti- k_t algorithm [197] implemented in `FASTJET` [198], where the ATLAS tracker’s pseudorapidity is $|\eta| < 2.49$ and the jet angular parameter $R = 0.4$.

Double counting of jets can occur when introducing ISR at the matrix element (ME) level and then subsequently hadronizing the partons in `Pythia8`. To avoid this, we use the MLM matching and merging procedure [199]. An `XQCut` of $M_{Z'}/10$ is used at the matrix element level which forces the production of only partons with a minimum K_T separation. Matching in `Pythia8` is done by enforcing `QCut > XQCut`. For photon ISR, a minimum transverse momentum cut is placed on additional photon radiation of $P_T > 10$ GeV (the default value in `Madgraph5_aMC@NLO`) to avoid soft and collinear divergences. We stress that our simulation of ISR is at leading order, and we do not attempt to resum logarithms of the threshold scale.

For the analysis of current triggers in Section 5.4, one million events are generated for each Z' mass within the range [50 GeV, 1500 GeV], with a step size of 50 GeV, for Models **A** and **B** in Table 5.1. A Z' width of $\Gamma_{Z'} = M_{Z'}/100$ is used throughout. A crude detector volume cut is implemented at the `Pythia8` stage. All particles that have not decayed outside of a cylinder of ($r = 3000$ mm, $z = 3000$

²<https://github.com/smsharma/SemivisibleJets>

mm) are considered stable. This cut was placed to mimic the detector volume out to the muon spectrometer. For the analysis of current triggers, background rates are already known and do not have to be estimated.

In Section 5.5, the focus is on using a machine learning approach for novel triggers. We are less interested in hard ISR events and therefore use Pythia8's hidden valley production process $f\bar{f} \rightarrow Z_\nu$ processes instead of Madgraph5_aMC@NLO. Hits on the ATLAS inner tracker are used as discriminating variables. A proper detector simulation of the inner tracker is outside of the scope of this work, but we use a crude detector simulation with code used in [52] which encompasses the ATLAS tracker from the Inner Bilayer (IBL) to the Transition Radiation Tracker (TRT). This detector simulation assumes simple models of energy loss through each thin layer of the detector. We use this custom simulation package because standard detector simulations used in phenomenological studies such as DELPHES do attempt to simulate the response to displaced decays. An emerging jet registers various hits as function of the radial distance from the interaction point. Section 5.5 considers Models **A**, **C**, **D**, **E** and **F**, and we choose a Z' mass of $M_{Z'} = 500$ GeV. This set of models span a wide range of lifetimes while keeping all other model parameters equal.

When considering new triggers, we must also estimate the background. Various background processes are considered, but the backgrounds are dominated by $pp \rightarrow b\bar{b}$ events which have high multiplicity and hadrons with longer lifetimes producing many displaced vertices that can mimic an emerging jet signal. We simulate 10^5 events of $gg \rightarrow b\bar{b}$ using Pythia8's heavy flavour hard $b\bar{b}$ processes. The inclusive background cross section σ_{bkg} is taken from the Pythia8 event generation stage, which is used to estimate the instantaneous background rate. Pileup is added to both signal and background events with Pythia8's minimum bias events. For each

signal or background event, a number of minimum bias events are added randomly sampled from a poisson distribution with mean of $\mu = 50$, mimicking the Run 2 conditions used in the trigger menus for the analysis of Section 5.5. The LHC is expected to go through a series of upgrades leading for Run 3 and beyond allowing for higher luminosities. Estimates within the first phase of Run 3 give mean pileup contributions as high as $\mu = 80$ [200]. Advances in hardware and changes to trigger thresholds are expected to relax the effects of this increase of soft minimum bias events on future searches [201].

5.4 Current triggers

A consequence of having high instantaneous luminosities, such as at the LHC, is the necessity of implementing triggering streams on specified event criteria. ATLAS/CMS produce event rates in the MHz range, which is far too large to write every event onto record. Triggers were introduced to greatly reduce the event rate that is written for offline use, to a manageable ~ 1 kHz. Although emerging jet experimental searches do exist [156], models with unique phenomenology such as emerging jets may not be visible to the current dedicated trigger sets used at ATLAS and CMS [183,184]. In this section, we quantify the efficiency of current triggers for emerging jet phenomenology.

In addition to leading order production, we also study the effects of ISR on trigger efficiencies which come from Feynman diagrams of the type shown in Fig. 5.2. Multiple QCD jets (and/or electroweak gauge bosons) can modify the naive expectation of a two-pronged emerging jet scenario. Each additional hard object will change the event's topology from back to back scattering in the transverse plane. Emerging jets on their own provide unique detector signals that may have difficulty passing trigger selections in various parameter regions. We will show that the inclusion of

Triggers	Lower (GeV)	Higher (GeV)	Offline (GeV)
Single Jet	100	420	435
Single γ	20*	140	145
Single e	22*	26*	27
Single μ	20	26*	27
MET	50	110	200
H_T	//	850	//

Table 5.2: The 2017 ATLAS triggers [202] used in Section 5.4 analysis. Triggers are separated by lower level (L1) thresholds, Higher level (HLT) thresholds and offline selection criteria. Reconstructed jets used in the Single Jet, MET and H_T trigger have $R = 0.4$. Thresholds with (*) must additionally satisfy the isolation cone criteria in Eq. (5.8). A lower level threshold isn't given for the H_T as we seed it from the lower level Single Jet trigger instead.

hard SM objects, such as jets and leptons, increases the likelihood of passing the triggers. Numerical trigger thresholds used in ATLAS [202] and used for this analysis are shown in Table 5.2.

5.4.1 Description of triggers

The trigger systems at both experiments are separated into two disjoint online subsystems: the low level hardware trigger system (L1), and the high level software trigger system (HLT). L1 primarily deals with low level information from energy depositions in the calorimeter towers and minimally reconstructed jet variables. Track reconstruction and jet algorithms are available at HLT triggers for more sophisticated triggering criteria. Here, we will describe the triggers that are relevant to our analysis.

MET Triggers: Dark sector mesons with sufficiently long lifetimes τ_d will typically escape the detector before decaying and thus contribute to Missing Transverse Energy (MET). Energy deposited within the calorimeter towers is reconstructed for MET calculations at both ATLAS and CMS. In the plane transverse to the beam, the transverse momentum P_T is conserved with a zero net P_T , and thus this observable

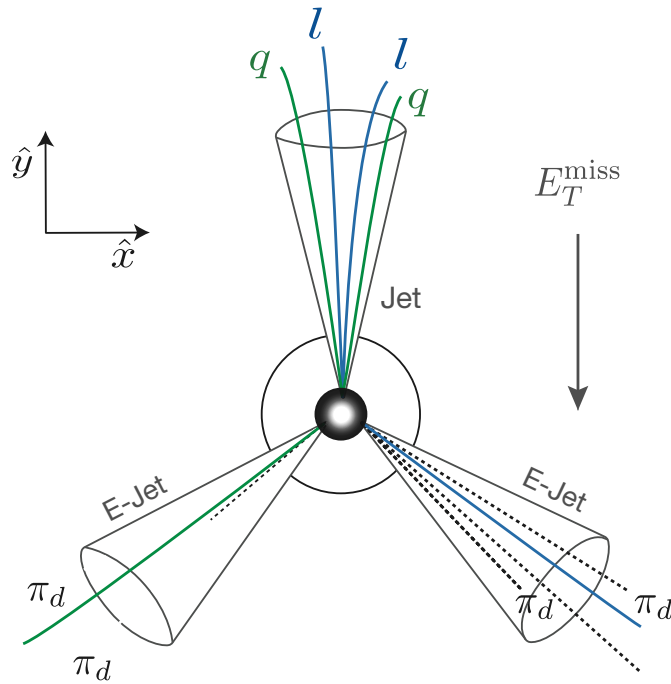


Figure 5.3: The Mercedes topology of three jets recoiling off of each other within the p_T plane. In this case, two emerging jets carrying missing transverse energy recoil off of a visible hard QCD jet. This configuration produces more missing transverse energy as the jet momenta are balanced in opposite directions.

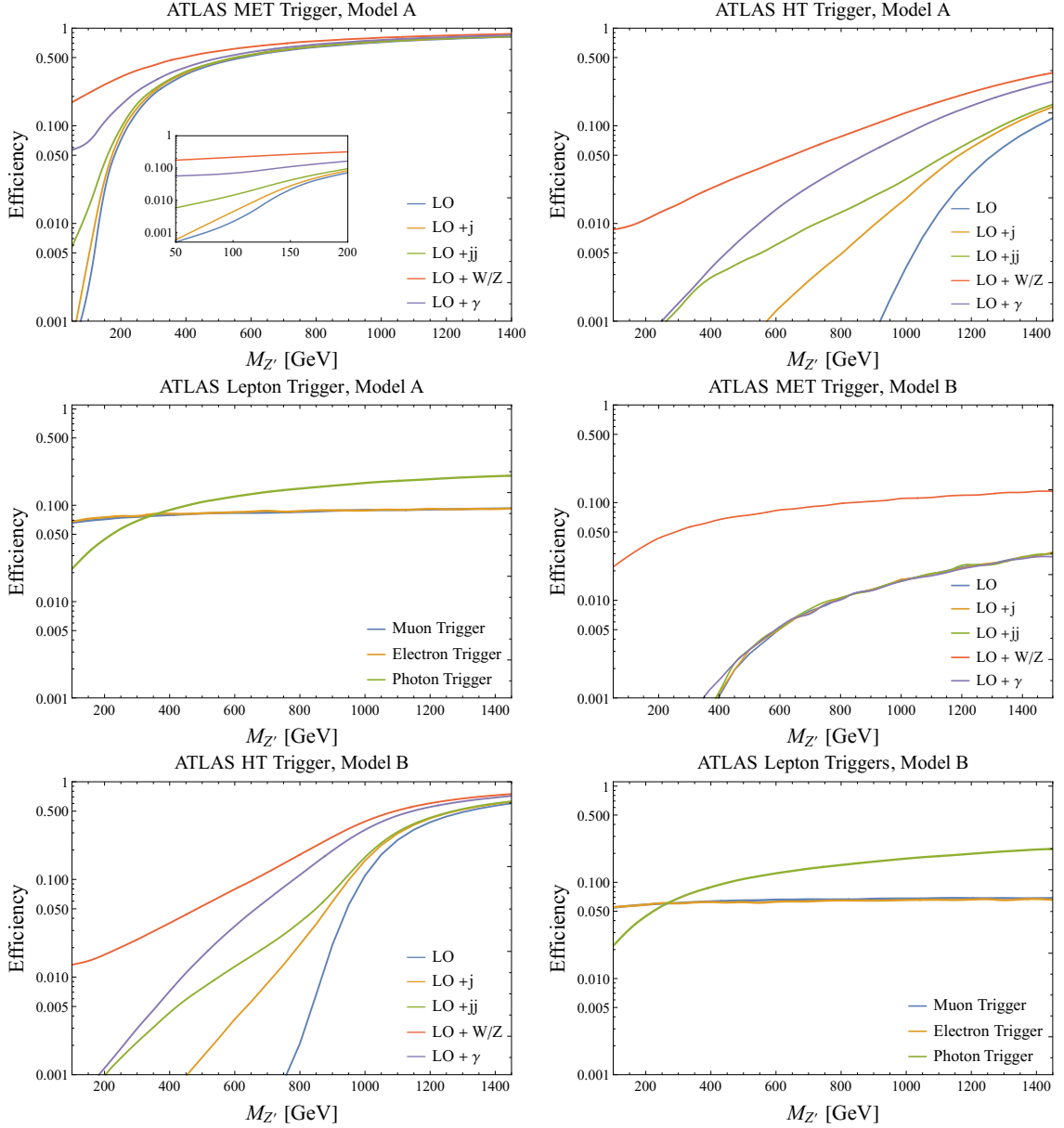


Figure 5.4: ATLAS trigger efficiencies, at truth level, for various processes outlined in Section 5.3. The first (second) row corresponds to Model **A** (**B**) from Table 5.1. In the first column, we have the MET triggers; in the second column, the H_T triggers; and, in the third column, the lepton and photon triggers. Both the electron and muon trigger efficiencies considered W/Z ISR while the photon trigger considered photon ISR only. All processes were generated under LHC conditions of a centre of mass energy of 13 TeV. The trigger thresholds were taken from the ATLAS trigger menu summarized in Table 5.2.

is sensitive to production of invisible particles. Energy deposition in each tower is summed and a transverse momentum vector is constructed using

$$P_T = \sqrt{(\sum P_x)^2 + (\sum P_y)^2}. \quad (5.7)$$

Any non-zero contribution is taken to be $\text{MET} = |P_T|$.

Triggers cut on an event's MET according to the trigger menu thresholds in Table 5.2, at both L1 and HLT. L1 thresholds are lower than the HLT, although the calculated MET might differ between reconstructed calorimeter tower energies at both levels. It is usually precise enough to assume that HLT is seeded from L1 with 100% efficiency, therefore we only consider the HLT efficiencies.

Typical Z' events, even if the dark hadrons have long lifetimes, tend to have relatively low MET because the two emerging jets are produced back to back, so there can be significant cancellation between them. Hard initial state radiation can qualitatively change this picture as shown in Fig. 5.3. With additional radiation the two emerging jets are no longer collinear, and their MET will to some extent add. Furthermore, the additional radiation means that the energy of each jet will be larger (for fixed Z' mass), which also tends to increase the MET. Fig. 5.3 shows QCD radiation, but the same logic applies to EW radiation.

H_T Triggers: The H_T trigger is a threshold on the scalar P_T sum of the event's reconstructed objects. These triggers help reduce rates by focusing on events with large final state transverse energy E_T . The H_T is built from objects with $|\eta| < 2.5$ and jets are only included if they have $P_T \geq 50$ GeV.

For the Z' model here, as the mediator mass increases, the trigger is more likely to be satisfied due to the larger final state momentum imparted onto the constituents. At lower mediator masses, the efficiency can be increased with additional hard QCD

radiation. The QCD jets are more visible than the dark sector jets and lead to a higher H_T . This is also realized in the EW ISR case, as the hard photon/ W/Z carries all of the ISR energy,³ and if properly reconstructed, contributes significantly to final state E_T . This effect can be seen in Fig. 5.3.

Lepton and Photon Triggers: ISR of a W^\pm, Z can add additional hard leptons and/or missing energy with neutrinos, and radiation of photons can also be used. Triggers that cut on identified leptons (e and μ) and photons, are considered. The trigger menu hosts a range of triggers depending on the level of reconstruction necessary for the identification of the event's particles.

Leptons and photons in the trigger are required to pass isolation criteria. For leptons, ATLAS identifies uses various classifications. These criteria are known as tight (loose) isolation [203, 204], which are defined by

$$\sum_{i \in \text{cone}} \frac{P_T^i(\Delta R < R^l)}{P_T^l} < \mathcal{I}, \quad (5.8)$$

where in Eq. (5.8), $\mathcal{I} = 0.6$ (1.5) for tight (loose) isolation, P_T^l is the transverse momentum of the candidate lepton, P_T^i are the transverse momentum of the visible non-candidate objects within the isolation cone, ΔR is the distance between the i^{th} particle and the candidate lepton l , and $R^l = 0.2$ (0.3) is the cone radius for electrons (muons). This is accomplished with P_T calculated from lepton track measurements.

In the case of photons, the isolation condition is given by

$$\sum_{i \in \text{cone}} E_T^i(\Delta R < R^\gamma) < 0.022 \cdot E_T^\gamma + 2.45 \text{ GeV}. \quad (5.9)$$

The photon isolation uses calorimeter measurements of the transverse energy E_T since

³In leptonic decays of the W or decays of the Z to neutrinos, the energy of the neutrinos of course do not contribute to H_T .

photons do not leave tracks, E_T^γ is the transverse energy of the candidate photon, and E_T^i is the transverse energy of the i^{th} cone constituent. Since we are simulating events without full detector effects, we assume that the truth level transverse energy of the photon is equal to that of the reconstructed calorimeter energies.

Trigger menus may demand different levels of isolation strictness between L1 and HLT. In Table 5.2, for the single electron trigger considered, both L1 and HLT must adhere to tight isolation criteria where as the muon trigger has isolation only at L1. It is important to consider these drastic differences of kinematic acceptance between L1 and HLT when calculating the total efficiency. Because of this, we do not assume that the lepton triggers are seeded from an L1 trigger with $\epsilon_{L1} = 1$ (100% efficiency). Instead, we calculate the L1 efficiency and project the product $\epsilon = \epsilon_{L1} \cdot \epsilon_{HLT}$ in our results.

5.4.2 Results with current triggers

We first calculate the trigger efficiency for different triggers in Model **A** and Model **B**. In this section we do not use a detector simulation as the output of `Pythia` should be a reasonable estimate of these simple variables. The efficiency is the number of events that pass the threshold, and therefore get written for offline use, over the total number of events, and these are shown in Fig. 5.4, with the top (bottom) row being for Model **A** (**B**). In the first column we see that for Model **A**, any kind of radiation increases the MET trigger efficiency because in Model **A** the dark hadrons have long lifetimes, and initial state radiation increases their momentum and makes them not back to back. Radiation of W/Z does the best because of the presence of neutrinos. For Model **B**, notice that we only get significant improvement with W/Z radiation.

In the second column of Fig. 5.4 we see that QCD radiation can significantly

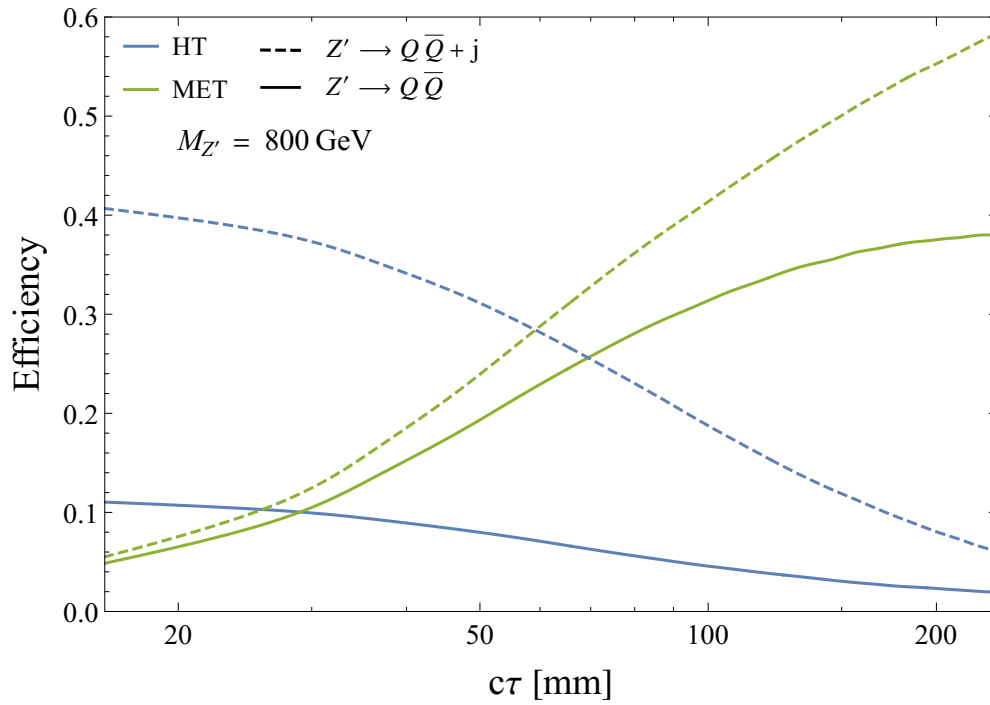


Figure 5.5: ATLAS trigger efficiencies as a function of the dark pion lifetime $c\tau$. The LO process is shown in the solid lines, the LO + j process is shown in the dashed lines. An inverse relationship is exhibited between MET and H_T efficiencies.

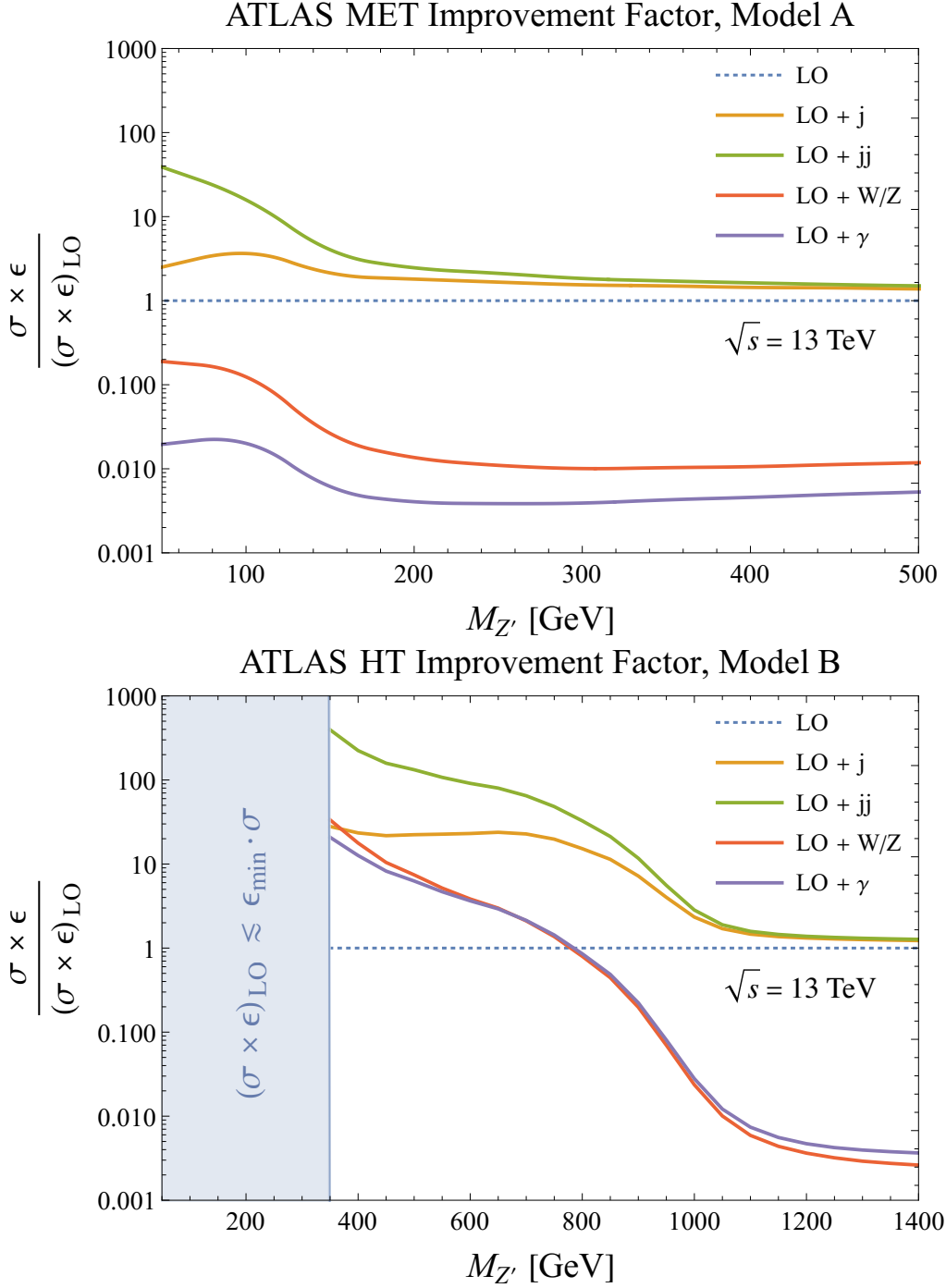


Figure 5.6: Cross section times efficiency of various processes (leading order, 1-jet ISR, 2-jet ISR, electro weak ISR) scaled by their respective leading order process. The left plot uses the MET trigger and Model **A**, while the right uses H_T and Model **B**. The dotted line is the leading order process, which when normalized to itself, is just unit as a reference for the rate boost obtained from additional processes. On the right plot, the blue region on the left has zero events that we simulated pass the trigger, $\epsilon \lesssim \epsilon_{\min} = 1/400\,000$.

increase the efficiency of the H_T trigger for both lifetime benchmarks, and two hard jets does better than a single extra jet. Both W/Z and photon radiation do better than QCD radiation because of the the clean visible momentum carried by the EW radiation. At low masses $M_{Z'} \lesssim 500$ GeV, the efficiencies are similar for both models while at higher masses $M_{Z'} \gtrsim 500$ GeV, Model **B** becomes far more efficient as it carries more visible particles in the final state. The improvement due to extra radiation is very important at low mass, a section of the Z' parameter space not easily probed, but less so at high mass because the trigger can already be quite efficient at leading order in that case.

We also show the trigger efficiency as a function of dark pion lifetime for a fixed Z' mass of 800 GeV in Fig. 5.5. As expected, as the lifetime increases, more of the energy escapes the detector and the MET trigger gets better while the H_T trigger gets worse. This explains the differences of the first and second columns of Fig. 5.4 between both Models **A** and **B**.

Finally in the third column of Fig. 5.4 considers the effect on lepton (photon) triggers on the process with additional W/Z (photon) radiation. The two models are almost identical, showing that these triggers are picking up the extra electroweak radiation. This assures us that the dark pion lifetimes and parameters of the confined hidden sector have little bearing on the EW focus of the lepton triggers. The slightly higher efficiency for lepton triggers (e, μ) in Model **A** because of the dark pion long lifetimes leaving less contaminants within the lepton isolation cone, i.e Eq. (5.8). In terms of the dependence on $M_{Z'}$, the electroweak radiation is roughly constant, while the photons tend to be harder at larger $M_{Z'}$ so the efficiency increases.

Although a useful metric, the efficiency does not consider the overall probability of the event occurring because it does not take into account that extra radiation

reduces the cross section. Therefore when looking at the total rate, we consider the cross section of the process times its respective efficiency. To get a proper sense of the rate independent of some of the unknown particle physics such as the couplings of the Z' , we take the ratio of the cross section times efficiency with respect to the leading order (LO) result with no additional radiation, and show the results in Fig. 5.6. In the left column we show the improvement achieved for the MET trigger in Model **A**. We see that QCD radiation can lead to significant improvements at low mass, and even at high mass simulating extra radiation increases the overall rate by $\mathcal{O}(100)\%$. We also see that simulating two additional jets gives significant improvement relative to only a single jet at low mass. Electroweak radiation only gives a modest improvement in the event rate, roughly 10% at low mass and even more modest at high mass. This is because the rate suppression due to α is significantly stronger than that from QCD that goes like α_s .

In the right column of Fig. 5.6 we show the improvement for the H_T trigger in Model **B**. At low mass, none of the 400 000 events we simulate at leading order pass the trigger, so considering radiation opens a new parameter regime for discovery. Even at intermediate masses, $M_{Z'} \sim 500$ GeV, additional radiation gives orders of magnitude improvement in rate. As with Model **A**, two additional jets gives the greatest improvement, but all processes considered can be significant.

5.5 Machine learning triggers

The current triggers of Section 5.4, although well understood, are still limited in their capacity to find new physics. They have forced us to consider subsets of model parameter space that best produce specific signals that current triggers discriminate best on and create blind spots in other regions of parameter space. The experiments at the

LHC have been investigating more novel ML methods to replace the cut based methods used for most analysis. Examples include W and top quark discrimination using boosted decision trees (BDT) [205,206], QCD jet substructure using adversarial neural networks (ANN) [207], and even alternatives to simulations of detector responses using generative adversarial networks (GAN) [208]. These non-linear methods are not limited to primary detector features, such as hard jets and charged particle tracks, as they can be trained (unsupervised) to converge on non-intuitive abstract features within an event.

We are interested in methods that can be employed at the triggering stage. Previous proposals advocated using BDTs as a fast and reliable high level trigger [209]. Similar to cut based methods, ML algorithms can be trained on a array of new physics simulations, opening up the door for unique correlations between new physics models that could prove generic for a dedicated trigger. Additionally, the computational resources necessary in training and testing the ML method does not impact the resources in-situ as the training/testing stage is done prior to implementation on the trigger stream.

Emerging jets produce interesting signatures and are complimentary to other models consisting of hidden sector portals with dark showers. Examples include semi-visible jets [135,137] and SUEPS [52], which exhibit extreme cases of a similar baseline theory to that of emerging jets. In this section, we employ the use of the ATLAS inner trackers in training ML methods for emerging jet signals for the purpose of triggering. Like the complimentary models mentioned above, emerging jets produce a wealth of uncharacteristic lifetimes as compared to the SM. Here we show that recruiting the inner tracker allows an ML algorithm to converge on discriminating features that exploit this gap in lifetimes between the new physics and the SM. Whether ML

methods converge on generic features of new physics or those more specific to the training model, understanding what is the physics behind these ML features has been a long standing question. Answering this question requires solving an inverse problem of the ML output, and proves more and more difficult as ML methods such as NN and BDT become more complex, although there is some recent progress [182]. Fortunately we can largely disregard this problem since the purpose of the trigger is to get as many interesting events onto record as possible. Anything written onto record can then be properly analyzed offline. So we take the pragmatic approach to ML and focus our attention on producing the highest trigger efficiency independent of what it is “seeing.”

As in Section 5.4, the trigger systems at both L1 and HLT are limited by their allocated computational resources. These triggering operations must be fast enough to reduce the input data stream to ~ 1 kHz. This can be challenging when data from all areas of the detector package are simultaneously used within the triggering systems in some form or another. Fitting non-linear algorithms, including those using ML methods, at the trigger level, can be taxing on the available resources. In this case, we look at low level variables such as hits on the tracking detectors and simple jet reconstructions from L1. This is similar to the strategy proposed in [185] in a different context. The lack of fully constructed particle tracks and momentum measurements allows for fully trained algorithms to operate quickly on the incoming data streams.

For concreteness, we will analyze the ATLAS tracker geometry in this section, but we expect similar qualitative conclusions for CMS. In Fig. 5.7 we show the fraction of the dark pions that decay in a given detector subsystem as a function of lifetime, and we see that for all lifetimes, the largest fraction is in the inner tracker. Therefore, we focus only on that system in this work, though we note that there could be

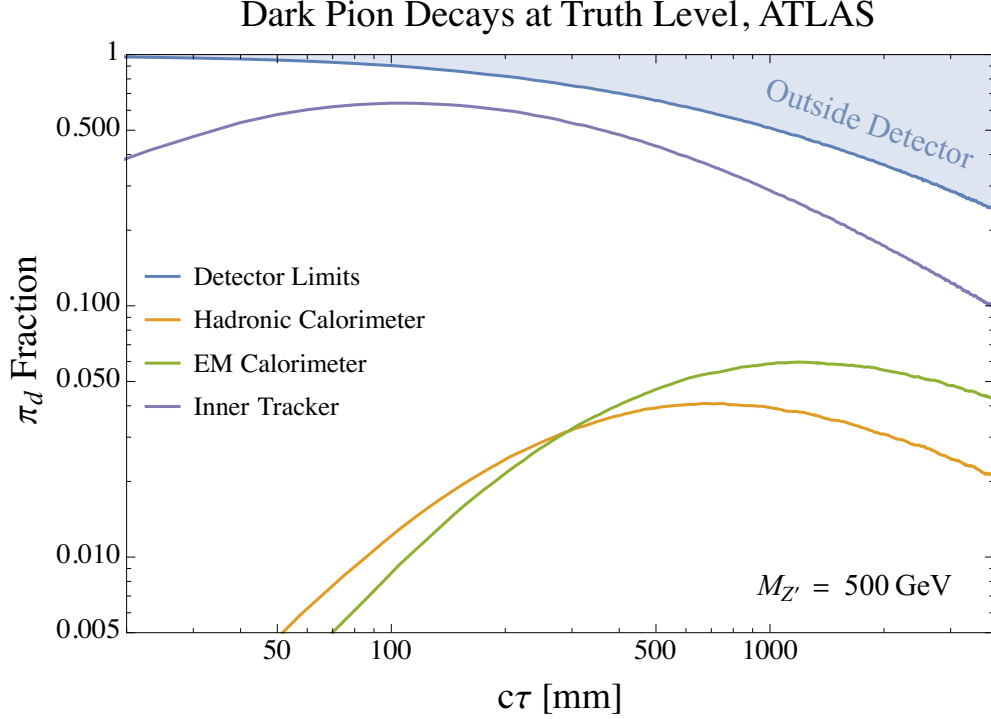


Figure 5.7: The fraction of dark pions that decay into visible sector particles within the primary ATLAS detectors. The green line represents the decay fraction within the electromagnetic calorimeter, the orange for the hadronic calorimeter, and the blue for the inner trackers. The blue line is the fiducial boundary of the muon spectrometer which we take to be the boundary of the ATLAS detector. We do not show that fraction that decay before the first tracker layer, and this fraction is significant at short lifetime. These fractions are computed from simulation with $M_{Z'} = 500$ GeV.

interesting improvements by including the calorimeters and muon system.

The ATLAS inner tracker comprises of, in increasing order of distance from the beam pipe: the Inner Bi-layer (IBL), the Pixel Detectors, the silicon detectors, and the Transition Radiation Tracker (TRT). Table 5.3 shows the number of layers and radial distances from the interaction point as well as whether the tracker has additional endcaps. The primary purpose of the inner trackers is track reconstruction and particle identification. Tracks are reconstructed at the HLT level where calorimeter information has been seeded from L1. Although useful, track reconstruction is a very computationally expensive operation as all possible track trajectories are back prop-

Tracker	Layer	Radius (mm)	Geometry
IBL		33.25	Barrel
	First	50.5	
Pixel	Second	88.5	Barrel + Endcap
	Third	122.5	
	First	299	
SCT	Second	371	Barrel + Endcap
	Third	443	
	Fourth	514	
TRT	Start	554	Barrel + Endcap

Table 5.3: ATLAS inner tracker specifications taken from [210, 211]. The barrel layers of each tracker section are shown with their radial distance from the beam pipe/interaction point. Since the TRT is a more complex tracking package, we only consider the hits on the initial layer of the TRT. Endcaps also accompany most of the trackers but aren't considered in this analysis.

agated towards the interaction point. We propose using machine learning methods trained on the hit patterns of the inner tracker's layers while bypassing full track reconstruction.

As noted in Section 5.3, in our simulations we take the dark hadronization to be dominated by dark pions. The proper lifetime of the dark pions depend strongly on the Z' mass as shown in Eq. (5.3), with lower mediator masses corresponding to shorter lifetimes. We assume a common lifetime for the dark pions, but for a study of hierarchical lifetimes see [153], and we take the lifetime to be a free parameter that we vary.

As the emerging jets traverse the inner tracker, the invisible dark pions decay into visible quarks which hadronize into SM jets with high particle multiplicity creating a complex bundle of displaced tracks as they decay throughout the detector volume. Ideally, without pileup and other secondary detector effects, the number of hits registered on the tracker layers should increase with radial distance.

Signal and background events are simulated and explained in Section 5.3. Hadronized

events are passed to a highly simplified detector simulation used for [52] that attempts to model the ATLAS inner tracker. The simulation accounts for updated particle trajectories from the bending of the ATLAS toroidal magnetic field, $B \approx 2\text{T}$, as well as energy loss from interactions with the material (assuming a thin layer approximation). The simulation does not account for the production of secondary particles from interactions with the layer materials. These secondaries are a possible source of error as they could fake a displaced vertex around each tracker. We are forced to use a custom simulation package because standard detector simulations used in phenomenological studies such as DELPHES do not track displaced vertices. For our analysis, we take combinations of the concentric tracker volumes utilizing the IBL_i , Pixel_i , SCT_i and TRT_i detectors where the subscript denotes the i^{th} layer. Results are represented as hit patterns in the form of heat maps in the (ϕ, η) plane for each layer of the trackers.

A simple strategy that ultimately does not work is to train a classifier using only the total number of hits recorded on each layer. This strategy reduces the 2D map in (ϕ, η) space to a single variable $N_{h,i}$ representing the number of hits on the i^{th} layer. The primary reason this strategy does not work is because of pileup. Each LHC event contains pileup from multiple proton collisions in each event. While there is only one hard collision responsible for the emerging jet production, the remaining collisions produce a large number of soft particles distributed approximately isotropically through the detector. This will typically wash out large differences in hits on consecutive layers $N_{h,i} - N_{h,i+1} \approx 0$. As discussed in Section 5.3, we simulate pileup by adding an average of 50 minimum bias collisions to both signal and $b\bar{b}$ background events. Since pileup is relatively soft, the toroid magnet will deflect charged particles with a radius of curvature inversely proportional to the particles momentum

$R_c \propto p^{-1}$. Pileup, in the form of minimum bias events, has characteristically low momentum spectrum, so layers at larger radial distances are less sensitive to pileup effects.

We refine our strategy by using the methods similar to those defined in [185], originally proposed for “trackless” b -tagging. The authors refer to their strategy to as “multiplicity jump,” of using hit profiles on the tracking layers. They mitigate the issue of soft pileup contamination by selecting only the hits within a predefined jet cone axis. In their case, they applied a small jet cone radius of $\Delta R < 0.04$ for b -tagging purposes. This makes calorimeter data inaccessible as the cone size is too small for the detectors’ granularity.

We propose to generalize this to larger hadronic jets with $\Delta R < 0.4$. By doing so, we can take advantage of low level calorimeter information, at trigger level, to calculate the jet cone directions of the event’s hard objects. Subsequently, only hit multiplicities matching the the vicinity of these cones are considered hits. In detail, energy deposition in the calorimeter is used to reconstruct jets in terms of topo clusters at L1 and at HLT. With jet information at the trigger levels we use the truth level jet vectors \hat{v} as well as the jet cone acceptance $\mathcal{R} = 0.5$ to define N_{cor}^i ,

$$N_{cor}^i \equiv \sum_j N_{h,j}^i \left(\sqrt{(\Delta\eta)_j^2 + (\Delta\phi)_j^2} \leq \mathcal{R} \right). \quad (5.10)$$

The sum runs through all grid points j of the layer i . $(\Delta\eta)_j = \eta_j - \eta_{\hat{v}}$, where η_j are pseudorapidities at grid point j and $\eta_{\hat{v}}$ is the pseudorapidity of leading jet direction \hat{v} . Similarly, $(\Delta\phi)_j = \phi_j - \phi_{\hat{v}}$. The radius of each layer R_i values can be found in Table 5.3. This approach allows us to build a classifier that is sensitive to a conical subset of hit patterns in the direction of an L1 topocluster jets. This substantially reduces the 4π reach of pileup.

We use the TMVA toolkit [212] to train and test an ML discriminator. Multiple ML methods were tested, BDT, NN, and support vector machines (SVM), and all methods investigated gave similar outputs for the level of this analysis. For that reason, we choose to an SVM as our benchmark method, as it is the simplest method. The SVM was trained on events containing signal and $b\bar{b}$ background events.

For this analysis, we fix $M_{Z'} = 500$ GeV. Models **A**, **C**, **D** and **E** (described in Table 5.1) are used as signal benchmarks. They vary in only the lifetimes while keeping all other dark sector parameters equal. We also included Model **F**, which has the lifetime of Model **D** but varies in the dark sector parameters. The TMVA support vector machine was trained and tested using Eq. (5.10) as the input variables. Testing and training sets were created and randomly separated from the simulation results. The left panel of Fig. 5.8 shows the resulting SVM signal and background discrimination. We see that there is excellent separation between signal background, and that the trained and tested distributions look very similar. Only four layers of the trackers were used, IBL, Pixel₂, SCT₂, TRT₁, sampled from each of the four inner tracker packages. This arrangement of layers allows the ML to train on snapshots of the emerging jets evolution at substantially separated intervals, but using only four layers reduces the required size of the training sample. A proper study could simulate a much larger and realistic sample size while incorporating additional layers.

Assuming that the event rate is background dominated, meaning very few new physics events occur, implemented triggers must reach background rates that do not exceed the allocated bandwidth. Unlike in Section 5.4 where we investigated pre-existing triggers, the background rates of our proposed novel triggers are unknown and must be estimated. The high level trigger rate usually allocated for new triggers

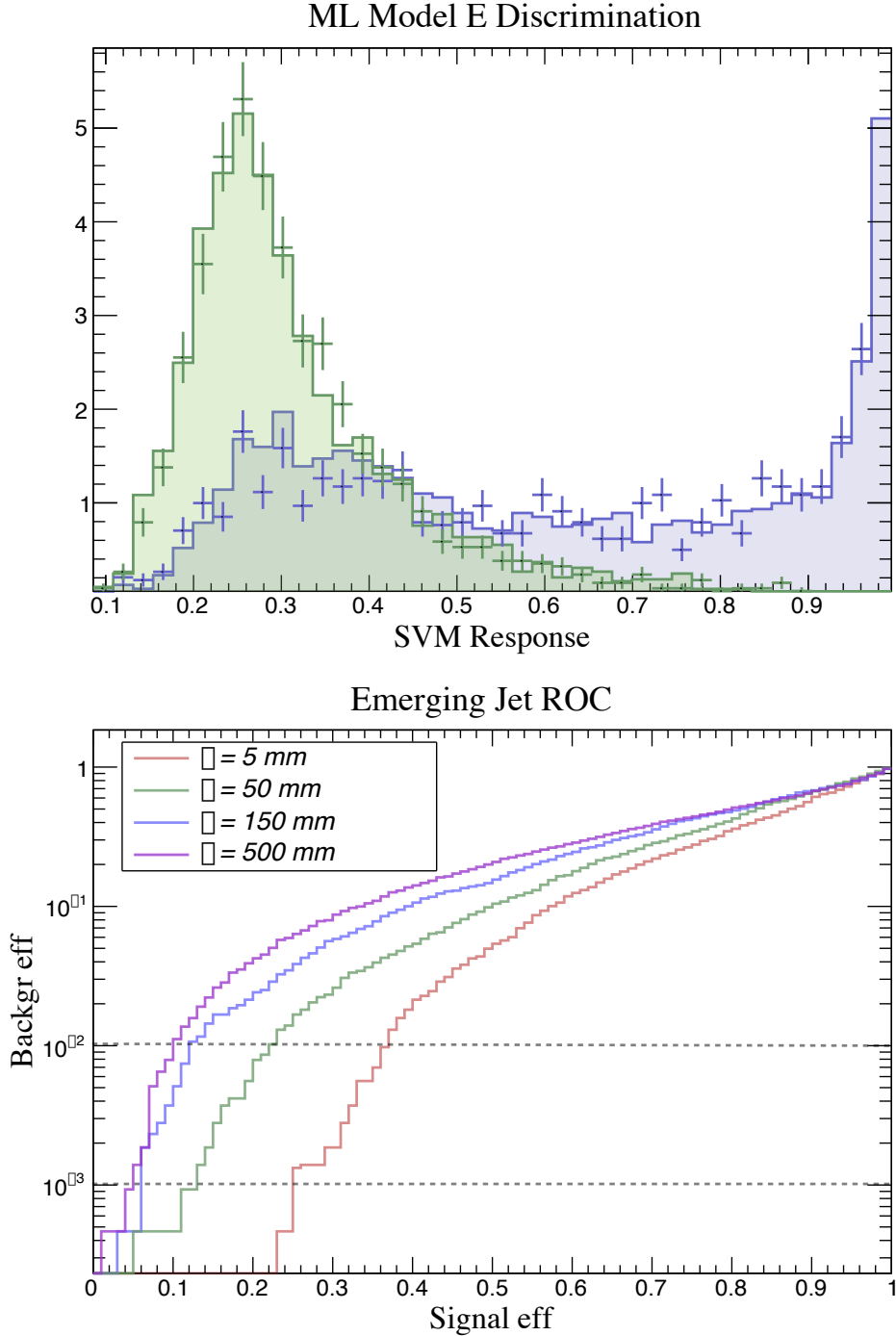


Figure 5.8: On the left, Model E (blue) discrimination from $b\bar{b}$ background (green) using a support vector machine. The SVM was trained using four layers IBL, Pixel₂, SCT₂, TRT₁. An average pileup of $\mu = 50$ was added to both signal and background. The flat bars (points) correspond to the training (test) set. On the right, Receiver Operation Characteristic ROC for Models **A**, **C**, **D**, and **E** using the TMVA support vector machine. The SVM was trained and tested using four layers: IBL, Pixel₂, SCT₂, TRT₁, with the input variable defined in Eq. (5.10). At a given background efficiency the expected signal efficiencies increase as the dark pion lifetimes lower. The required background rejection is estimated to lie between the horizontal dotted lines.

is of $R \sim 1$ Hz [213]. The required background rejection is given by,

$$\epsilon_{\text{bkg}} = \frac{R}{\sigma_{\text{bkg}} \mathcal{L}} \sim 10^{-3} - 10^{-2} \quad (5.11)$$

for a peak instantaneous luminosity of $\mathcal{L} = 21 \times 10^{33} \text{ cm}^{-2}\text{s}^{-1}$. The background rates were estimated assuming high p_T $b\bar{b}$ production, which primarily mimic the signal events. Additional backgrounds were considered, such as inclusive hard QCD backgrounds, generated through `Pythia8`. Since these additional background sources had substantially smaller efficiencies than pure heavy flavour $b\bar{b}$, we take them to be negligible to the total background rates. Inclusive background cross sections were taken from the `Pythia8` hard event generation as explained in Section 5.3, but these background cross sections are leading order and thus only order of magnitude estimates.

The new trigger background rejection rate will set an upper bound on the signal efficiency for each value of the ML response. The Receiver Operator Characteristic curve (ROC) gives a visualization of this efficiency space. The ROC curve is shown in Fig. 5.8 as the background vs. signal efficiency for each SVM response value. The value of the signal efficiency ϵ can be read off for each model at the highest allowable ATLAS trigger background efficiency. In Table 5.4, we see the range of ϵ for various lifetimes ranging from 5 mm to 500 mm. Shorter lifetimes seem to outperform longer lifetimes. In Model **E** ($c\tau_d = 5$ mm) there are distinct hit patterns all within the IBL and the beginning of the TRT. These dark pions are boosted such that their respective emerging jets must go through majority of its evolution between these inner tracker slices. Whereas for the higher lifetime models, their evolution from invisible to visible is either skewed towards the later layers or even clipped beyond the tracker limits. Efficiencies of $\mathcal{O}(0.1-0.3)$ can be found for a comparable resonance mass of $M_{Z'} = 500$ GeV for the simple s -channel process with no additional hard ISR. Comparing these

$c\tau_d$	ϵ (Bkg rej 10^{-2})	ϵ (Bkg rej 10^{-3})
5 mm	0.370	0.250
50 mm	0.230	0.125
150 mm	0.122	0.060
500 mm	0.100	0.050

Table 5.4: Signal efficiencies for expected allowable background rates for new ATLAS triggers for $M_{Z'} = 500$ GeV. The lifetimes represent Models **A**, **C**, **D**, and **E**. Each value in the last two columns are extracted from Fig. 5.8 for a bkg efficiency calculated using Eq. (5.11) assuming the events are fully saturated by background.

to the signal efficiencies found in Section 5.4 (see Fig. 5.4) we see that for similar topologies, training on detector hits can be advantageous as current triggers have less reach in the low mass regime.

So far we have discussed training and testing on the same model parameters. Implementing an ML trigger would require training on some expected signal model prior to integration on the trigger stream. As mentioned earlier, emerging jets and other models of dark showers have a large available lifetime parameter space. Training an ML trigger on a single model parameter point could bias the trigger towards classifying only a small portion of this parameter space. The overall classification power is related to the area under the ROC curve (AUC). As a test of the universality of this method, we take an unknown sample set from each of the five models and apply each of the trained SVMs on them as was done in [214]. The results are seen in where the diagonal corresponds to the AUC of Fig. 5.9. Each row is of an SVM trained on a single lifetime and then applied to an unknown signal set of differing or same lifetime (columns). The deviations from each unknown lifetime set is of order a few percent. This reinforces the insensitivity of the trigger to the parameters it was trained on. Each rows' average AUC value does not have a substantial change. Model **F** was included to see how sensitive this analysis is on the parameters of the hidden sector,

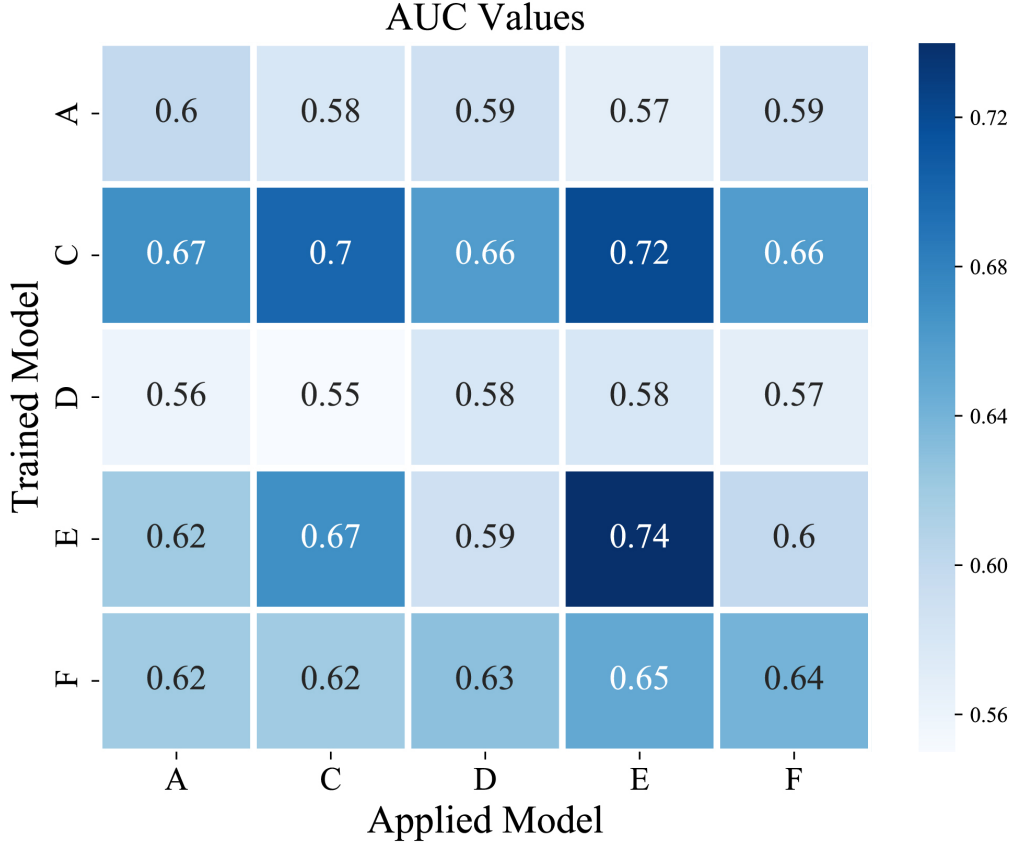


Figure 5.9: Area Under the Curve (AUC) of the ROC curves. The SVM was trained on specific models (vertical axis) and tested/applied on a unknown data set (horizontal axis) of the same/alternative model. The diagonals are the AUC values corresponding for training and testing on the same models i.e. the ROC curves of Fig. 5.8. Trained models show little separation in classification power when applied to a range of lifetimes and hidden sector parameters.

such as the hadronization scale Λ_d , and the dark meson masses (π_d, ρ_d). The first thing to notice is that when trained on Model **F** there is almost no change in the AUC when applied to the range of lifetime models, much like Model **D** which shares the same lifetime. Secondly, when the various trained models are applied to both Model **F** and Model **D**, the AUC values are almost identical. This similarity gives us more confidence in the universality of the trigger, such that it is mostly sensitive to pion lifetimes while being largely insensitive to other deviations in the hidden sector.

5.6 Summary and conclusions

In this work we explore ways to trigger on new physics models with a high multiplicity of displaced vertex of the type explored in [29]. If the mediator is uncharged under the SM gauge groups, then it can be relatively light and associated SM radiation is not guaranteed, so triggering on these events at the LHC is not straightforward. If events are not triggered on, they are forever lost, so maximizing trigger efficiency is a necessary step for maximizing discovery potential.

We have first explored how both efficiency and event rate can be increased using current triggers with the addition of initial state radiation. Our main results are given in Figs. 5.4 and 5.6. Both QCD and electroweak radiation increase the total energy of the event and thus increases the efficiency of H_T triggers. The effects are the largest for relatively light mediators, but they can also be relevant for heavy mediators. Other triggers, such as those searching for missing energy, leptons, and photons can also have higher efficiency with certain radiation. Processes with radiation have lower cross sections than the leading order process, but we have shown that even taking this into account, there are significant increases in event rate, especially at low mass. This ISR process is guaranteed by gauge invariance to exist, and we encourage experimentalists to simulate these processes in future studies.

We have also explored possible new triggers using modern machine learning methods that use simple counts of hits in the tracker as input variables. The new physics models considered here leave an increasing number of hits on each tracker layer as the dark mesons decay in flight to visible SM states. Counting hits in the tracker is significantly faster than performing track reconstruction, making it an ideal technique for a trigger. The use of ML techniques allows for a more sophisticated separation of signal and background based on these hit counts, and the effectiveness of our proposed

method is shown in Fig. 5.8. Using ML for triggering can significantly reduce one of the primary problems of ML techniques in particle physics that it is difficult to determine which features the algorithms are training on, and thus difficult to estimate systematic errors. For a trigger, one wants to maximize the events recorded, and then a full study of systematics can be done at the analysis stage.

Finally, we have explored the sensitivity of our ML techniques across different model parameters as summarized in Fig. 5.9. Of course, the underlying model parameters of the new physics are unknown, and the ideal trigger would be sensitive to as much of the parameter space as possible and also to new physics models not captured by the simulation framework used in this work. We see that varying the particle physics parameters of the dark sector does significantly affect the efficiency, so a realistic trigger can be trained on one model parameter and still be sensitive to a broad class of new physics models.

Chapter 6

Conclusion

In the last few chapters, we have explored a multitude of different physical phenomena—from the small scales of particle physics, to the large scales of gravitational wave astronomy. In an attempt to look beyond the conventional Standard Models of both particle physics and cosmology, novel signature spaces were discovered. These signature spaces stemming from new particles, forces, and sectors. The question of whether these extensions to the conventional model exists can only be answered by experimentation and data. It is our job as scientists to try to be impartial viewers of the Universe. Understanding the biased lens we wear when looking at the data is just as important as the data itself. This is the prime motive for the studies contained in this thesis.

In the study of GW from multiple sectors, we demonstrated that a cosmologically consistent model with one or more hidden sectors produces novel gravitational wave power spectra. In the toy model case of N naturalness, the gravitational wave spectrum was not in the discoverability limits of near future experiments. Instead more generalized scenarios with multiple hidden sectors are in a region accessible to next-generation experiments. Not only are they detectable, but their spectra show

unique characteristics such as peak broadening, and in the extreme cases, multiple peaks. Any interferometer data fitting these template spectra would be a smoking gun for extensions with multiple hidden sectors.

In the study of emerging jets from a single hidden sector at the colliding experiments, new triggering strategies were proposed in an attempt to reduce the selection process. Using the dedicated triggers with additional sources of radiation lead to an increase in the overall efficiencies of the triggers. With the particle experiments adopting new online analysis strategies, a machine learning trigger was proposed. This new algorithm was trained on low dimensional preprocessed variables in the form of tracker hits. The method was shown to not only increase the overall selection efficiency, but was also independent of the parameters of the model.

Appendix A

Runaway Phase Transitions

If the phase transition occurs in the non-runaway regime ($\alpha_\infty > \alpha$), the dominant contributions to the GW energy densities are given by the sound wave $h^2\Omega_v$ and MHD $h^2\Omega_{turb}$ components [94],

$$h^2\Omega_{\text{GW}} \approx h^2\Omega_v + h^2\Omega_{turb}. \quad (\text{A.1})$$

The new contributions to the GW energy density take on a different form from Eq. (4.41) [80],

$$\begin{aligned} h^2\Omega_v^* &= 1.6 \times 10^{-1} v \left(\frac{\kappa_v \alpha}{1 + \alpha} \right)^2 \left(\frac{H}{\beta} \right)^1 S_v(f), \\ h^2\Omega_{turb}^* &= 2.01 \times 10^1 v \left(\frac{\kappa_{turb} \alpha}{1 + \alpha} \right)^{3/2} \left(\frac{H}{\beta} \right)^1 S_{turb}(f). \end{aligned} \quad (\text{A.2})$$

Unlike the runaway case, we do not assume $v = 1$ due to the bubbles reaching a terminal velocity. The MHD efficiency factor is a fraction of the sound waves, $\kappa_{turb} = \epsilon \kappa_v$. Current simulations have motivated a range of $\epsilon \sim 0.05 - 0.10$ [80], where we take the optimistic case of $\epsilon = 0.10$. Both contributions have unique

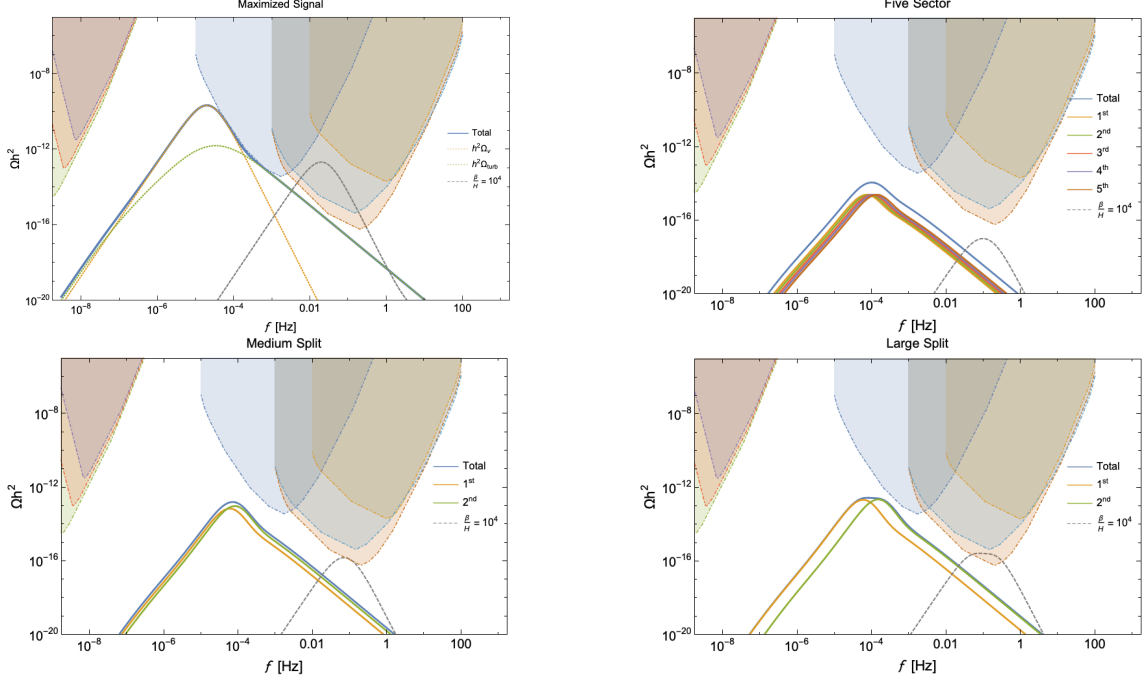


Figure A.1: Gravitational wave spectral energy density for the various scenarios found in Tab. (4.1). All contributions are assumed to be from a non-runaway phase transition with terminal velocity $v = 0.95$. The coloured solid lines use $\beta/H = 10$ where as the dashed grey line is the total contribution of all sectors for $\beta/H = 10^4$. The top left figure shows the individual sound wave and MHD contributions. The shaded curves are the same as Fig. 4.1. In contrast to the runaway case, most scenarios evade the projected sensitivities.

spectral shapes, given to be [94],

$$\begin{aligned}
 S_v(f) &= (f/f_{p,v})^3 \left(\frac{7}{4 + 3(f/f_{p,v})^2} \right)^{7/2}, \\
 S_{turb}(f) &= \frac{(f/f_{p,turb})^3}{(1 + f/f_{p,turb})^{11/3} (1 + 8\pi(f/H))}.
 \end{aligned}
 \tag{A.3}$$

The MHD energy density has a spectral shape dependent on the Hubble rate at the time of nucleation, H . Similar to the scalar spectral shape in Eq. (4.42), the frequencies are scaled by their respective temperature dependent peak frequency,

$$\begin{aligned}
f_{p,v} &= 1.9 \times 10^{-5} \text{ Hz} \frac{1}{v} \left(\frac{\beta}{H} \right) \left(\frac{T_\gamma}{100 \text{ GeV}} \right) \left(\frac{g_*}{100} \right)^{\frac{1}{6}}, \\
f_{p,turb} &= 2.7 \times 10^{-5} \text{ Hz} \frac{1}{v} \left(\frac{\beta}{H} \right) \left(\frac{T_\gamma}{100 \text{ GeV}} \right) \left(\frac{g_*}{100} \right)^{\frac{1}{6}}.
\end{aligned}
\tag{A.4}$$

We evolve the frequencies and energy densities with the same redshift factors, Eq. (4.44) from Sec 4.6. Fig. A.1 shows the sum of the GW energy density for the scenarios in Table 4.1, but instead for the non-runaway case, with a terminal velocity of $v = 0.95$. For this case we see that the spectra tend to be shifted to lower frequencies and are more likely to fall in the gap between the interferometers and the pulsar based detectors. On the other hand, larger values of β/H increase the typical frequency, so this case becomes more sensitive in some scenarios to values of β/H on the larger end of the considered range.

In the sound wave case, these parametrizations are extracted from simulations with $\beta/H < 100$ corresponding to a long lasting sound wave component. For high β/H the transition timescale from sound wave to MHD turbulence is much shorter than the Hubble time. When estimating the model expectations for $\beta/H = 10^4$, we enter a regime at which Eq. (A.2) may be overestimating the sound wave contribution. Investigations of this regime have been done in [215–217]. This effect, however, only affects the amplitude of the signal, and our work focuses on the unique spectral shapes that are formed in these models. Therefore we project our results for high β/H in Fig. A.1 to motivate the novel spectral profiles.

Finally, we note that because the sound wave and MHD contributions have different spectral shapes, the overall spectrum has a kink at a frequency above the peak. In the top left panel of Fig. A.1, we show the two contributions separately in

addition to their sum to highlight this effect.

Appendix B

Dark Showering Models

Hidden valley models [26] with QCD-like hidden sectors allow for interesting collider signatures. Thus we consider a confined dark gauge group $SU(N_d)$, where $N_d \geq 2$, with confinement scale Λ_d which sets the mass of the dark hadrons. There are also n_f flavors of dark quarks whose bare masses are lighter than Λ_d . The hidden valley comes equipped with a portal that couples the dark sector to the SM, and the mass is usually taken to be $M \gg \Lambda_d$. The portal can be an s -channel vector mediator, Z_d which couples to SM quarks and dark quarks:

$$\mathcal{L} \supset -Z_{d,\mu} \sum_{i,a} (g_q \bar{q}_i \gamma^\mu q_i + g_{q_d} \bar{q}_{d,a} \gamma^\mu q_{d,a}), \quad (\text{B.1})$$

where g_{q/q_d} are coupling constants and i, a are flavor indices. One can also have a t channel scalar bifundamental mediator, X , which carries color and dark color and can decay to a quark and a dark quark. In the case of the scalar mediator, the only allowable coupling is of the form

$$\mathcal{L} \supset \kappa_{ij} \bar{q}_i q_{d,j} X + \text{h.c.}, \quad (\text{B.2})$$

where, κ_{ij} is a $3 \times n_f$ matrix of Yukawa couplings. One could also add multiple flavors of X mediators, something that has also been implemented.

When dark quarks are produced, they shower and hadronize and we can use the same tools that are familiar for QCD to simulate these processes. Because of the large gap between the mediator mass and the confining scale, there will be large particle multiplicity and the dark hadrons will typically form into jet-like structures. In the large N_d limit, the fraction of dark baryons produced is suppressed, and in the case of QCD this fraction is $\mathcal{O}(0.1)$. Therefore the simulations typically have the dark mesons to dominate hadronization. The lightest hadronic states are the dark pions π_d , acting as goldstone bosons of the $U(n_f) \times U(n_f)$ dark flavor symmetry. When a heavier mesonic state is produced it will promptly decay into dark pions if kinematically allowed, making the dark pions the dominant component of the dark showering process.

We can simulate these events with the Hidden Valley [47] version of `Pythia8` [46]. `Pythia8` hosts a hidden valley class which incorporates the $SU(N_d)$ model, allowing the user to vary the masses of the spectrum (π_d, ρ_d, etc), number of flavors n_f , and parameters of the running coupling (Version ≥ 8.226). Pair production of X and resonant production of Z_d are implemented at tree level, and there is also decay of dark mesons to SM states.

In both [10, 137], production of the heavy mediators with ISR/FSR was considered. This was done by interfacing with `Madgraph5_aMC@NLO` [195] using a modified version of the spin-1 `DMsimp` model¹ implemented through `FeynRules` [193]. The models are located in the repository² folder `DMsimp_s_spin1`. The generation files for the t-channel exchange of the scalar X are located in the folder `DMsimp_tchannel`.

¹<http://feynrules.irmp.ucl.ac.be/wiki/DMsimp>

²<https://github.com/smsharma/SemivisibleJets>

The bi-fundamentals are denoted with `su11`, `su12`, `su21`, `su22`..., where `u` explicitly specifies the QCD flavor index and the numbers are the explicit dark non-Abelian group indices. Similarly, the dark quarks are labeled as `qv11`, `qv12`, `qv21`, `qv22`. A `FeynRules` model file (`DMsimp_tchannel.fr`) as well as the Mathematica notebook (`DMsimp_tchannel.nb`) used to generate the UFO output are also provided. The showering and hadronization in the dark sector can still be performed in `Pythia8`.

B.1 Semi-visible Jets

Generically, some of the dark pions could decay promptly and some could be long-lived or even collider stable, analogous to the neutral vs. charged pions in the SM. If both stable and unstable hadrons are produced in a collision, the missing energy could be aligned along one of the jets, resulting in low acceptance for traditional monojet-style searches. This is the semi-visible jets scenario, and Refs. [135, 137] introduce a Simplified Model-like parameterization to map the complicated dynamics of the underlying dark sector onto a limited number of physically-motivated variables—in particular, the fraction of stable vs decaying pions, the characteristic mass scale of dark pions and the dark coupling strength. The Monte Carlo production described here along with the `Pythia8` Hidden Valley module allows the user to vary these parameters for the s - and t -channel UV completions. See Refs. [135, 137] for further details.

B.2 Emerging Jets

One can also take all the pions to have detector scale lifetimes, this is the emerging jets scenario [29]. One can quantify the expected lifetime of the dark pions using Eq. B.2. Under the assumption of universal couplings $\kappa_{ij} = \kappa$ and $m_q > \Lambda_d$, we can

calculate the proper lifetime of the dark pions:

$$c\tau_0 \approx 80\text{mm} \times \frac{1}{\kappa} \times \left(\frac{2 \text{ GeV}}{f_{\pi_d}}\right)^2 \left(\frac{100 \text{ MeV}}{m_q}\right) \left(\frac{2 \text{ GeV}}{m_{\pi_d}}\right) \left(\frac{M_X}{1 \text{ TeV}}\right)^4, \quad (\text{B.3})$$

where, f_{π_d} is the dark pion decay constant, and m_q is the mass of the SM quark in the final state. A similar formula comes out for the Z_d mediator. Therefore a jet of dark hadrons will be created as dominantly invisible particles, but at long distance, the dark pions will decay back to Standard Model particles and appear like an ordinary jet. The jet emerges as it travels through the detectors.

In the case of purely t -channel interactions, having a non-trivial κ_{ij} in Eq. (B.1) will break the $U(n_f) \times U(n_f)$ dark flavor symmetry. With an appropriate n_f the dark quark flavors can be exactly aligned with the SM down quark flavors. It is immediately clear that such alignment leads to dark pions with lifetimes that differ significantly from one another. In return, the flavor composition of the emerging jets will vary throughout the detector volume. This differs from the s -channel interaction, in which, no breaking occurs and n_f -stable vs. $n_f(n_f - 1)$ -unstable dark pions exist

References

- [1] M. Peskin and D. Schroeder, *An Introduction To Quantum Field Theory*. Frontiers in Physics. Avalon Publishing, 1995.
- [2] M. Schwartz, *Quantum Field Theory and the Standard Model*. Quantum Field Theory and the Standard Model. Cambridge University Press, 2014.
- [3] E. Kolb and M. Turner, *The Early Universe*. Frontiers in physics. Addison-Wesley, 1990.
- [4] J. Hartle, *Gravity: An Introduction to Einstein's General Relativity*. Addison-Wesley, 2003.
- [5] M. Perelstein, *Introduction to Collider Physics*, in *Theoretical Advanced Study Institute in Elementary Particle Physics: Physics of the Large and the Small*, pp. 421–486, 2011. [arXiv:1002.0274](#).
- [6] J. Campbell, J. Huston, and F. Krauss, *The Black Book of Quantum Chromodynamics: A Primer for the LHC Era*. Oxford University Press, 2018.
- [7] G. Cowan, *Statistical Data Analysis*. Oxford science publications. Clarendon Press, 1998.
- [8] P. Archer-Smith, D. Linthorne, and D. Stolarski, *Gravitational Wave Signals from Multiple Hidden Sectors*, *Phys. Rev. D* **101** (2020), no. 9 095016, [[arXiv:1910.02083](#)].
- [9] J. Alimena et al., *Searching for long-lived particles beyond the Standard Model at the Large Hadron Collider*, *J. Phys. G* **47** (2020), no. 9 090501, [[arXiv:1903.04497](#)].
- [10] D. Linthorne and D. Stolarski, *Triggering on emerging jets*, *Phys. Rev. D* **104** (2021), no. 3 035019, [[arXiv:2103.08620](#)].
- [11] P. W. Higgs, *Spontaneous symmetry breakdown without massless bosons*, *Phys. Rev.* **145** (May, 1966) 1156–1163.

- [12] S. L. Glashow, *Partial-symmetries of weak interactions*, *Nuclear Physics* **22** (1961), no. 4 579–588.
- [13] S. Weinberg, *A model of leptons*, *Phys. Rev. Lett.* **19** (Nov, 1967) 1264–1266.
- [14] A. Freitas, *Precision Tests of the Standard Model*, *PoS TASI2020* (2021) 005, [[arXiv:2012.11642](https://arxiv.org/abs/2012.11642)].
- [15] H. Goldstein, C. Poole, and J. Safko, *Classical Mechanics*. Addison Wesley, 2002.
- [16] E. Noether, *Invariante variationsprobleme*, *Nachrichten von der Gesellschaft der Wissenschaften zu Gttingen, Mathematisch-Physikalische Klasse* **1918** (1918) 235–257.
- [17] **ATLAS**, G. Aad et al., *Observation of a new particle in the search for the Standard Model Higgs boson with the ATLAS detector at the LHC*, *Phys. Lett. B* **716** (2012) 1–29, [[arXiv:1207.7214](https://arxiv.org/abs/1207.7214)].
- [18] **CMS**, S. Chatrchyan et al., *Observation of a New Boson at a Mass of 125 GeV with the CMS Experiment at the LHC*, *Phys. Lett. B* **716** (2012) 30–61, [[arXiv:1207.7235](https://arxiv.org/abs/1207.7235)].
- [19] C. Csáki and P. Tanedo, *Beyond the Standard Model*, in *2013 European School of High-Energy Physics*, pp. 169–268, 2015. [arXiv:1602.04228](https://arxiv.org/abs/1602.04228).
- [20] P. D. Group, *Review of Particle Physics, Progress of Theoretical and Experimental Physics* **2020** (08, 2020). 083C01.
- [21] F. Zwicky, *On the Masses of Nebulae and of Clusters of Nebulae*, *Astrophys. J* **86** (Oct., 1937) 217.
- [22] V. C. Rubin and W. Kent, *Rotation of the Andromeda Nebula from a Spectroscopic Survey of Emission Regions*, *Astrophys. J* **159** (1970) 379–403.
- [23] **SDSS**, J. K. Adelman-McCarthy et al., *The Fourth Data Release of the Sloan Digital Sky Survey*, *Astrophys. J. Suppl.* **162** (2006) 38–48, [[astro-ph/0507711](https://arxiv.org/abs/astro-ph/0507711)].
- [24] M. Markevitch, A. H. Gonzalez, D. Clowe, A. Vikhlinin, L. David, W. Forman, C. Jones, S. Murray, and W. Tucker, *Direct constraints on the dark matter self-interaction cross-section from the merging galaxy cluster 1E0657-56*, *Astrophys. J.* **606** (2004) 819–824, [[astro-ph/0309303](https://arxiv.org/abs/astro-ph/0309303)].

- [25] C. L. Bennett, M. Halpern, G. Hinshaw, N. Jarosik, A. Kogut, M. Limon, S. S. Meyer, L. Page, D. N. Spergel, G. S. Tucker, E. Wollack, E. L. Wright, C. Barnes, M. R. Greason, R. S. Hill, E. Komatsu, M. R. Nolta, N. Odegard, H. V. Peiris, L. Verde, and J. L. Weiland.
- [26] M. J. Strassler and K. M. Zurek, *Echoes of a hidden valley at hadron colliders*, *Phys. Lett. B* **651** (2007) 374–379, [[hep-ph/0604261](#)].
- [27] M. J. Strassler and K. M. Zurek, *Echoes of a hidden valley at hadron colliders*, *Phys. Lett. B* **651** (2007) 374–379, [[hep-ph/0604261](#)].
- [28] Y. Bai and P. Schwaller, *Scale of dark QCD*, *Phys. Rev. D* **89** (2014), no. 6 063522, [[arXiv:1306.4676](#)].
- [29] P. Schwaller, D. Stolarski, and A. Weiler, *Emerging Jets*, *JHEP* **05** (2015) 059, [[arXiv:1502.05409](#)].
- [30] G. Hinshaw, D. Larson, E. Komatsu, D. N. Spergel, C. Bennett, J. Dunkley, M. Nolta, M. Halpern, R. Hill, N. Odegard, et al., *Nine-year wilkinson microwave anisotropy probe (wmap) observations: cosmological parameter results*, *The Astrophysical Journal Supplement Series* **208** (2013), no. 2 19.
- [31] J. M. Cline, *TASI Lectures on Early Universe Cosmology: Inflation, Baryogenesis and Dark Matter*, *PoS TASI2018* (2019) 001, [[arXiv:1807.08749](#)].
- [32] P. Schneider, *Extragalactic Astronomy and Cosmology*. 2006.
- [33] L. Husdal, *On Effective Degrees of Freedom in the Early Universe*, *Galaxies* **4** (2016), no. 4 78, [[arXiv:1609.04979](#)].
- [34] **Planck**, N. Aghanim et al., *Planck 2018 results. VI. Cosmological parameters*, *Astron. Astrophys.* **641** (2020) A6, [[arXiv:1807.06209](#)]. [Erratum: *Astron.Astrophys.* 652, C4 (2021)].
- [35] G. Mangano, G. Miele, S. Pastor, T. Pinto, O. Pisanti, and P. D. Serpico, *Relic neutrino decoupling including flavor oscillations*, *Nucl. Phys.* **B729** (2005) 221–234, [[hep-ph/0506164](#)].
- [36] **Planck**, N. Aghanim et al., *Planck 2018 results. VI. Cosmological parameters*, [[arXiv:1807.06209](#)].
- [37] *Planck early results. i. the planck mission*, *A&A* **536** (2011) A1.
- [38] C. Bonati, P. de Forcrand, M. D’Elia, O. Philipsen, and F. Sanfilippo, *Constraints on the two-flavor QCD phase diagram from imaginary chemical potential*, *PoS LATTICE2011* (2011) 189, [[arXiv:1201.2769](#)].

- [39] P. Schwaller, *Gravitational Waves from a Dark Phase Transition*, *Phys. Rev. Lett.* **115** (2015), no. 18 181101, [[arXiv:1504.07263](#)].
- [40] Y. Bai, A. J. Long, and S. Lu, *Dark Quark Nuggets*, *Phys. Rev.* **D99** (2019), no. 5 055047, [[arXiv:1810.04360](#)].
- [41] N. Arkani-Hamed, T. Cohen, R. T. D’Agnolo, A. Hook, H. D. Kim, and D. Pinner, *Solving the Hierarchy Problem at Reheating with a Large Number of Degrees of Freedom*, *Phys. Rev. Lett.* **117** (2016), no. 25 251801, [[arXiv:1607.06821](#)].
- [42] **LIGO Scientific Collaboration and Virgo Collaboration**, B. P. Abbott, *Observation of gravitational waves from a binary black hole merger*, *Phys. Rev. Lett.* **116** (Feb, 2016) 061102.
- [43] **ATLAS**, F. Pastore, *ATLAS Run-2 status and performance*, *Nucl. Part. Phys. Proc.* **270-272** (2016) 3–7.
- [44] **ATLAS**, G. Aad et al., *The ATLAS Experiment at the CERN Large Hadron Collider*, *JINST* **3** (2008) S08003.
- [45] J. Campbell, J. Huston, and F. Krauss, *The black book of quantum chromodynamics: A primer for the LHC Era*. 03, 2018.
- [46] T. Sjöstrand, S. Ask, J. R. Christiansen, R. Corke, N. Desai, P. Ilten, S. Mrenna, S. Prestel, C. O. Rasmussen, and P. Z. Skands, *An Introduction to PYTHIA 8.2*, *Comput. Phys. Commun.* **191** (2015) 159–177, [[arXiv:1410.3012](#)].
- [47] L. Carloni and T. Sjöstrand, *Visible Effects of Invisible Hidden Valley Radiation*, *JHEP* **09** (2010) 105, [[arXiv:1006.2911](#)].
- [48] G. C. Fox and S. Wolfram, *A Model for Parton Showers in QCD*, *Nucl. Phys. B* **168** (1980) 285–295.
- [49] B. Andersson, G. Gustafson, G. Ingelman, and T. Sjöstrand, *Parton fragmentation and string dynamics*, *Physics Reports* **97** (1983), no. 2 31–145.
- [50] T. Sjöstrand, *Jet fragmentation of multiparton configurations in a string framework*, *Nuclear Physics B* **248** (1984), no. 2 469–502.
- [51] G. S. Bali and K. Schilling, *Static quark-antiquark potential: Scaling behavior and finite-size effects in $su(3)$ lattice gauge theory*, *Phys. Rev. D* **46** (Sep, 1992) 2636–2646.
- [52] S. Knapen, S. Pagan Griso, M. Papucci, and D. J. Robinson, *Triggering Soft Bombs at the LHC*, *JHEP* **08** (2017) 076, [[arXiv:1612.00850](#)].

- [53] S. Knapen, J. Shelton, and D. Xu, *Perturbative benchmark models for a dark shower search program*, *Phys. Rev. D* **103** (2021), no. 11 115013, [[arXiv:2103.01238](#)].
- [54] G. P. Salam and G. Soyez, *A Practical Seedless Infrared-Safe Cone jet algorithm*, *JHEP* **05** (2007) 086, [[arXiv:0704.0292](#)].
- [55] S. Catani, Y. Dokshitzer, M. Olsson, G. Turnock, and B. Webber, *New clustering algorithm for multijet cross sections in $e+e$ annihilation*, *Physics Letters B* **269** (1991), no. 3 432–438.
- [56] S. Catani, Y. Dokshitzer, M. H. Seymour, and B. Webber, *Longitudinally-invariant k -clustering algorithms for hadron-hadron collisions*, *Nuclear Physics* **406** (1993) 187–224.
- [57] M. H. Seymour, *Searches for new particles using cone and cluster jet algorithms: a comparative study*, *Zeitschrift für Physik C Particles and Fields* **62** (1994), no. 1 127–138.
- [58] B. Efron and T. Hastie, *Computer Age Statistical Inference: Algorithms, Evidence, and Data Science*. Institute of Mathematical Statistics Monographs. Cambridge University Press, 2016.
- [59] M. Thoma, *Receiver operating characteristic (roc) curve with false positive rate and true positive rate*, 2018. [Online; accessed Oct 27, 2021].
- [60] J. Neyman and E. S. Pearson, *On the Problem of the Most Efficient Tests of Statistical Hypotheses*, *Philosophical Transactions of the Royal Society of London Series A* **231** (Jan., 1933) 289–337.
- [61] D. R. Cox, *The regression analysis of binary sequences*, *Journal of the Royal Statistical Society: Series B (Methodological)* **20** (1958), no. 2 215–232.
- [62] J. Hopfield, *Neural networks and physical systems with emergent collective computational abilities*, *Proceedings of the National Academy of Sciences of the United States of America* **79** (05, 1982) 2554–8.
- [63] K. Hornik, M. Stinchcombe, and H. White, *Multilayer feedforward networks are universal approximators*, *Neural Networks* **2** (1989), no. 5 359–366.
- [64] H. M. C. Cheng, *The discussion of the xor problem*, *JOURNAL OF HEBEI UNIVERSITY (NATURAL SCIENCE EDITION)* (1999) 01.
- [65] **LIGO Scientific, Virgo**, B. P. Abbott et al., *Observation of Gravitational Waves from a Binary Black Hole Merger*, *Phys. Rev. Lett.* **116** (2016), no. 6 061102, [[arXiv:1602.03837](#)].

- [66] K. Danzmann, *LISA: Laser interferometer space antenna for gravitational wave measurements*, in *Relativistic astrophysics and cosmology. Proceedings, 17th Symposium, Munich, Germany, December 11-17, 1997*, pp. 481–484, 1994.
- [67] N. Seto, S. Kawamura, and T. Nakamura, *Possibility of direct measurement of the acceleration of the universe using 0.1-Hz band laser interferometer gravitational wave antenna in space*, *Phys. Rev. Lett.* **87** (2001) 221103, [[astro-ph/0108011](#)].
- [68] J. Crowder and N. J. Cornish, *Beyond LISA: Exploring future gravitational wave missions*, *Phys. Rev.* **D72** (2005) 083005, [[gr-qc/0506015](#)].
- [69] J. Crowder and N. J. Cornish, *Beyond lisa: Exploring future gravitational wave missions*, *Phys. Rev. D* **72** (Oct, 2005) 083005.
- [70] G. M. Harry, P. Fritschel, D. A. Shaddock, W. Folkner, and E. S. Phinney, *Laser interferometry for the big bang observer*, *Class. Quant. Grav.* **23** (2006) 4887–4894. [Erratum: *Class. Quant. Grav.*23,7361(2006)].
- [71] G. Janssen et al., *Gravitational wave astronomy with the SKA*, *PoS AASKA14* (2015) 037, [[arXiv:1501.00127](#)].
- [72] **LISA**, H. Audley et al., *Laser Interferometer Space Antenna*, [arXiv:1702.00786](#).
- [73] P. Amaro-Seoane et al., *Laser Interferometer Space Antenna*, *arXiv e-prints* (Feb, 2017) arXiv:1702.00786, [[arXiv:1702.00786](#)].
- [74] S. S. et al, *The status of DECIGO*, *Journal of Physics: Conference Series* **840** (may, 2017) 012010.
- [75] S. Isoyama, H. Nakano, and T. Nakamura, *Multiband gravitational-wave astronomy: Observing binary inspirals with a decihertz detector*, *B-DECIGO, Progress of Theoretical and Experimental Physics* **2018** (07, 2018).
- [76] E. Witten, *Cosmic Separation of Phases*, *Phys. Rev.* **D30** (1984) 272–285.
- [77] C. J. Hogan, *NUCLEATION OF COSMOLOGICAL PHASE TRANSITIONS*, *Phys. Lett.* **133B** (1983) 172–176.
- [78] C. J. Hogan, *Gravitational radiation from cosmological phase transitions*, *Mon. Not. Roy. Astron. Soc.* **218** (1986) 629–636.
- [79] M. S. Turner and F. Wilczek, *Relic gravitational waves and extended inflation*, *Phys. Rev. Lett.* **65** (Dec, 1990) 3080–3083.

- [80] C. Caprini et al., *Science with the space-based interferometer eLISA. II: Gravitational waves from cosmological phase transitions*, *JCAP* **1604** (2016), no. 04 001, [[arXiv:1512.06239](#)].
- [81] A. Mazumdar and G. White, *Review of cosmic phase transitions: their significance and experimental signatures*, *Rept. Prog. Phys.* **82** (2019), no. 7 076901, [[arXiv:1811.01948](#)].
- [82] J. Jaeckel, V. V. Khoze, and M. Spannowsky, *Hearing the signal of dark sectors with gravitational wave detectors*, *Phys. Rev.* **D94** (2016), no. 10 103519, [[arXiv:1602.03901](#)].
- [83] A. Addazi, *Limiting First Order Phase Transitions in Dark Gauge Sectors from Gravitational Waves experiments*, *Mod. Phys. Lett.* **A32** (2017), no. 08 1750049, [[arXiv:1607.08057](#)].
- [84] E. Hardy, *Miniclusters in the Axiverse*, *JHEP* **02** (2017) 046, [[arXiv:1609.00208](#)].
- [85] K. R. Dienes, F. Huang, S. Su, and B. Thomas, *Dynamical Dark Matter from Strongly-Coupled Dark Sectors*, *Phys. Rev.* **D95** (2017), no. 4 043526, [[arXiv:1610.04112](#)].
- [86] K. Tsumura, M. Yamada, and Y. Yamaguchi, *Gravitational wave from dark sector with dark pion*, *JCAP* **1707** (2017), no. 07 044, [[arXiv:1704.00219](#)].
- [87] B. S. Acharya, M. Fairbairn, and E. Hardy, *Glueball dark matter in non-standard cosmologies*, *JHEP* **07** (2017) 100, [[arXiv:1704.01804](#)].
- [88] N. Bernal, M. Heikinheimo, T. Tenkanen, K. Tuominen, and V. Vaskonen, *The Dawn of FIMP Dark Matter: A Review of Models and Constraints*, *Int. J. Mod. Phys.* **A32** (2017), no. 27 1730023, [[arXiv:1706.07442](#)].
- [89] M. Aoki, H. Goto, and J. Kubo, *Gravitational Waves from Hidden QCD Phase Transition*, *Phys. Rev.* **D96** (2017), no. 7 075045, [[arXiv:1709.07572](#)].
- [90] M. Heikinheimo, K. Tuominen, and K. Langble, *Hidden strongly interacting massive particles*, *Phys. Rev.* **D97** (2018), no. 9 095040, [[arXiv:1803.07518](#)].
- [91] M. Geller, A. Hook, R. Sundrum, and Y. Tsai, *Primordial Anisotropies in the Gravitational Wave Background from Cosmological Phase Transitions*, *Phys. Rev. Lett.* **121** (2018), no. 20 201303, [[arXiv:1803.10780](#)].
- [92] D. Croon, V. Sanz, and G. White, *Model Discrimination in Gravitational Wave spectra from Dark Phase Transitions*, *JHEP* **08** (2018) 203, [[arXiv:1806.02332](#)].

- [93] I. Baldes and C. Garcia-Cely, *Strong gravitational radiation from a simple dark matter model*, *JHEP* **05** (2019) 190, [[arXiv:1809.01198](#)].
- [94] M. Breitbach, J. Kopp, E. Madge, T. Opferkuch, and P. Schwaller, *Dark, Cold, and Noisy: Constraining Secluded Hidden Sectors with Gravitational Waves*, [arXiv:1811.11175](#).
- [95] M. Fairbairn, E. Hardy, and A. Wickens, *Hearing without seeing: gravitational waves from hot and cold hidden sectors*, *JHEP* **07** (2019) 044, [[arXiv:1901.11038](#)].
- [96] A. J. Helmboldt, J. Kubo, and S. van der Woude, *Observational prospects for gravitational waves from hidden or dark chiral phase transitions*, [arXiv:1904.07891](#).
- [97] A. Caputo and M. Reig, *Cosmic implications of a low-scale solution to the axion domain wall problem*, [arXiv:1905.13116](#).
- [98] G. Bertone et al., *Gravitational wave probes of dark matter: challenges and opportunities*, [arXiv:1907.10610](#).
- [99] G. Dvali and M. Redi, *Phenomenology of Dark Sectors*, *Phys. Rev.* **D80** (2009) 055001, [[arXiv:0905.1709](#)].
- [100] N. Craig, S. Knapen, and P. Longhi, *Neutral Naturalness from Orbifold Higgs Models*, *Phys. Rev. Lett.* **114** (2015), no. 6 061803, [[arXiv:1410.6808](#)].
- [101] N. Craig, S. Knapen, and P. Longhi, *The Orbifold Higgs*, *JHEP* **03** (2015) 106, [[arXiv:1411.7393](#)].
- [102] D. Chialva, P. S. B. Dev, and A. Mazumdar, *Multiple dark matter scenarios from ubiquitous stringy throats*, *Physical Review D* **87** (Mar, 2013).
- [103] K. R. Dienes and B. Thomas, *Dynamical Dark Matter: I. Theoretical Overview*, *Phys. Rev.* **D85** (2012) 083523, [[arXiv:1106.4546](#)].
- [104] K. R. Dienes and B. Thomas, *Dynamical Dark Matter: II. An Explicit Model*, *Phys. Rev.* **D85** (2012) 083524, [[arXiv:1107.0721](#)].
- [105] L. Susskind, *Dynamics of Spontaneous Symmetry Breaking in the Weinberg-Salam Theory*, *Phys. Rev.* **D20** (1979) 2619–2625.
- [106] D. J. Marsh, *Axion cosmology*, *Physics Reports* **643** (2016) 1 – 79. Axion cosmology.
- [107] M. Geller, A. Hook, R. Sundrum, and Y. Tsai, *Primordial anisotropies in the gravitational wave background from cosmological phase transitions*, *Phys. Rev. Lett.* **121** (Nov, 2018) 201303.

- [108] Y. Aoki, G. Endrodi, Z. Fodor, S. D. Katz, and K. K. Szabo, *The Order of the quantum chromodynamics transition predicted by the standard model of particle physics*, *Nature* **443** (2006) 675–678, [[hep-lat/0611014](#)].
- [109] T. Bhattacharya et al., *QCD Phase Transition with Chiral Quarks and Physical Quark Masses*, *Phys. Rev. Lett.* **113** (2014), no. 8 082001, [[arXiv:1402.5175](#)].
- [110] B. Svetitsky and L. G. Yaffe, *Critical behavior at finite-temperature confinement transitions*, *Nuclear Physics B* **210** (1982), no. 4 423 – 447.
- [111] R. D. Pisarski and F. Wilczek, *Remarks on the Chiral Phase Transition in Chromodynamics*, *Phys. Rev.* **D29** (1984) 338–341.
- [112] M. Panero, *Thermodynamics of the QCD plasma and the large- N limit*, *Phys. Rev. Lett.* **103** (2009) 232001, [[arXiv:0907.3719](#)].
- [113] J.-W. Cui, H.-J. He, L.-C. Lu, and F.-R. Yin, *Spontaneous Mirror Parity Violation, Common Origin of Matter and Dark Matter, and the LHC Signatures*, *Phys. Rev.* **D85** (2012) 096003, [[arXiv:1110.6893](#)].
- [114] **Particle Data Group**, M. Tanabashi et al., *Review of particle physics*, *Phys. Rev. D* **98** (Aug, 2018) 030001.
- [115] M. Gell-Mann, R. J. Oakes, and B. Renner, *Behavior of current divergences under $su_3 \times su_3$* , *Phys. Rev.* **175** (Nov, 1968) 2195–2199.
- [116] M. D. Schwartz, *Quantum Field Theory and the Standard Model*. Cambridge University Press, 2014.
- [117] **CMB-S4**, K. N. Abazajian et al., *CMB-S4 Science Book, First Edition*, [[arXiv:1610.02743](#)].
- [118] M. Trodden and S. M. Carroll, *TASI lectures: Introduction to cosmology*, in *Progress in string theory. Proceedings, Summer School, TASI 2003, Boulder, USA, June 2-27, 2003*, pp. 703–793, 2004. [[astro-ph/0401547](#)]. [,703(2004)].
- [119] Z. Fodor and S. D. Katz, *Lattice determination of the critical point of QCD at finite T and μ* , *JHEP* **03** (2002) 014, [[hep-lat/0106002](#)].
- [120] A. D. Linde, *Decay of the False Vacuum at Finite Temperature*, *Nucl. Phys.* **B216** (1983) 421. [Erratum: *Nucl. Phys.*B223,544(1983)].
- [121] J. R. Espinosa, T. Konstandin, J. M. No, and G. Servant, *Energy Budget of Cosmological First-order Phase Transitions*, *JCAP* **1006** (2010) 028, [[arXiv:1004.4187](#)].

- [122] C. Grojean and G. Servant, *Gravitational waves from phase transitions at the electroweak scale and beyond*, *Phys. Rev. D* **75** (Feb, 2007) 043507.
- [123] A. Kosowsky, M. S. Turner, and R. Watkins, *Gravitational radiation from colliding vacuum bubbles*, *Phys. Rev. D* **45** (Jun, 1992) 4514–4535.
- [124] S. J. Huber and T. Konstandin, *Gravitational wave production by collisions: more bubbles*, *Journal of Cosmology and Astroparticle Physics* **2008** (sep, 2008) 022.
- [125] M. Hindmarsh, S. J. Huber, K. Rummukainen, and D. J. Weir, *Gravitational waves from the sound of a first order phase transition*, *Phys. Rev. Lett.* **112** (Jan, 2014) 041301.
- [126] C. Caprini and R. Durrer, *Gravitational waves from stochastic relativistic sources: Primordial turbulence and magnetic fields*, *Phys. Rev. D* **74** (Sep, 2006) 063521.
- [127] D. Bdeker and G. D. Moore, *Electroweak bubble wall speed limit*, *Journal of Cosmology and Astroparticle Physics* **2017** (May, 2017) 025025.
- [128] M. Kamionkowski, A. Kosowsky, and M. S. Turner, *Gravitational radiation from first-order phase transitions*, *Phys. Rev. D* **49** (Mar, 1994) 2837–2851.
- [129] E. Thrane and J. D. Romano, *Sensitivity curves for searches for gravitational-wave backgrounds*, *Phys. Rev. D* **88** (Dec, 2013) 124032.
- [130] B. Allen and J. D. Romano, *Detecting a stochastic background of gravitational radiation: Signal processing strategies and sensitivities*, *Phys. Rev. D* **59** (Mar, 1999) 102001.
- [131] T. Robson, N. J. Cornish, and C. Liu, *The construction and use of LISA sensitivity curves*, *Classical and Quantum Gravity* **36** (apr, 2019) 105011.
- [132] K. Yagi, N. Tanahashi, and T. Tanaka, *Probing the size of extra dimensions with gravitational wave astronomy*, *Phys. Rev. D* **83** (Apr, 2011) 084036.
- [133] K. YAGI, *Scientific potential of decigo pathfinder and testing gr with space-borne gravitational wave interferometers*, *International Journal of Modern Physics D* **22** (2013), no. 01 1341013.
- [134] T. Alanne, T. Hügler, M. Platscher, and K. Schmitz, *A fresh look at the gravitational-wave signal from cosmological phase transitions*, 2019.
- [135] T. Cohen, M. Lisanti, and H. K. Lou, *Semivisible Jets: Dark Matter Undercover at the LHC*, *Phys. Rev. Lett.* **115** (2015), no. 17 171804, [[arXiv:1503.00009](https://arxiv.org/abs/1503.00009)].

- [136] C. Csaki, E. Kuflik, S. Lombardo, and O. Slone, *Searching for displaced Higgs boson decays*, *Phys. Rev. D* **92** (2015), no. 7 073008, [[arXiv:1508.01522](#)].
- [137] T. Cohen, M. Lisanti, H. K. Lou, and S. Mishra-Sharma, *LHC Searches for Dark Sector Showers*, *JHEP* **11** (2017) 196, [[arXiv:1707.05326](#)].
- [138] A. Pierce, B. Shakya, Y. Tsai, and Y. Zhao, *Searching for confining hidden valleys at LHCb, ATLAS, and CMS*, *Phys. Rev. D* **97** (2018), no. 9 095033, [[arXiv:1708.05389](#)].
- [139] G. Burdman and G. Lichtenstein, *Displaced Vertices from Hidden Glue*, *JHEP* **08** (2018) 146, [[arXiv:1807.03801](#)].
- [140] H.-C. Cheng, L. Li, E. Salvioni, and C. B. Verhaaren, *Light Hidden Mesons through the Z Portal*, *JHEP* **11** (2019) 031, [[arXiv:1906.02198](#)].
- [141] J. Alimena et al., *Searching for long-lived particles beyond the Standard Model at the Large Hadron Collider*, *J. Phys. G* **47** (2020), no. 9 090501, [[arXiv:1903.04497](#)].
- [142] M. J. Strassler and K. M. Zurek, *Discovering the Higgs through highly-displaced vertices*, *Phys. Lett. B* **661** (2008) 263–267, [[hep-ph/0605193](#)].
- [143] T. Han, Z. Si, K. M. Zurek, and M. J. Strassler, *Phenomenology of hidden valleys at hadron colliders*, *JHEP* **07** (2008) 008, [[arXiv:0712.2041](#)].
- [144] S. J. Lonsdale, M. Schroor, and R. R. Volkas, *Asymmetric Dark Matter and the hadronic spectra of hidden QCD*, *Phys. Rev. D* **96** (2017), no. 5 055027, [[arXiv:1704.05213](#)].
- [145] S. J. Lonsdale and R. R. Volkas, *Comprehensive asymmetric dark matter model*, *Phys. Rev. D* **97** (2018), no. 10 103510, [[arXiv:1801.05561](#)].
- [146] N. Craig, A. Katz, M. Strassler, and R. Sundrum, *Naturalness in the Dark at the LHC*, *JHEP* **07** (2015) 105, [[arXiv:1501.05310](#)].
- [147] D. Curtin and C. B. Verhaaren, *Discovering Uncolored Naturalness in Exotic Higgs Decays*, *JHEP* **12** (2015) 072, [[arXiv:1506.06141](#)].
- [148] H.-C. Cheng, E. Salvioni, and Y. Tsai, *Exotic electroweak signals in the twin Higgs model*, *Phys. Rev. D* **95** (2017), no. 11 115035, [[arXiv:1612.03176](#)].
- [149] C. Kilic, S. Najjari, and C. B. Verhaaren, *Discovering the Twin Higgs Boson with Displaced Decays*, *Phys. Rev. D* **99** (2019), no. 7 075029, [[arXiv:1812.08173](#)].

- [150] M. Park and M. Zhang, *Tagging a jet from a dark sector with Jet-substructures at colliders*, *Phys. Rev. D* **100** (2019), no. 11 115009, [[arXiv:1712.09279](#)].
- [151] T. Cohen, J. Doss, and M. Freytsis, *Jet Substructure from Dark Sector Showers*, *JHEP* **09** (2020) 118, [[arXiv:2004.00631](#)].
- [152] H. Mies, C. Scherb, and P. Schwaller, *Collider constraints on dark mediators*, [arXiv:2011.13990](#).
- [153] S. Renner and P. Schwaller, *A flavoured dark sector*, *JHEP* **08** (2018) 052, [[arXiv:1803.08080](#)].
- [154] S. Alekhin et al., *A facility to Search for Hidden Particles at the CERN SPS: the SHiP physics case*, *Rept. Prog. Phys.* **79** (2016), no. 12 124201, [[arXiv:1504.04855](#)].
- [155] D. Curtin et al., *Long-Lived Particles at the Energy Frontier: The MATHUSLA Physics Case*, *Rept. Prog. Phys.* **82** (2019), no. 11 116201, [[arXiv:1806.07396](#)].
- [156] **CMS**, A. M. Sirunyan et al., *Search for new particles decaying to a jet and an emerging jet*, *JHEP* **02** (2019) 179, [[arXiv:1810.10069](#)].
- [157] L. J. Hall and J. Polchinski, *Implications of Supersymmetric Origins for Monojets*, *Phys. Lett. B* **152** (1985) 335–339.
- [158] O. Nachtmann, A. Reiter, and M. Wirbel, *Single jet and single photon production in proton-antiproton collisions and e^+e^- annihilation in a supersymmetric model*, *Zeitschrift für Physik C Particles and Fields* **27** (1985), no. 4 577–586.
- [159] D. A. Dicus, S. Nandi, and J. Woodside, *Collider Signals of a Superlight Gravitino*, *Phys. Rev. D* **41** (1990) 2347.
- [160] A. Brignole, F. Feruglio, M. L. Mangano, and F. Zwirner, *Signals of a superlight gravitino at hadron colliders when the other superparticles are heavy*, *Nucl. Phys. B* **526** (1998) 136–152, [[hep-ph/9801329](#)]. [Erratum: *Nucl.Phys.B* 582, 759–761 (2000)].
- [161] Y. Gershtein, F. Petriello, S. Quackenbush, and K. M. Zurek, *Discovering hidden sectors with mono-photon Z' searches*, *Phys. Rev. D* **78** (2008) 095002, [[arXiv:0809.2849](#)].
- [162] Y. Bai, P. J. Fox, and R. Harnik, *The Tevatron at the Frontier of Dark Matter Direct Detection*, *JHEP* **12** (2010) 048, [[arXiv:1005.3797](#)].

- [163] J. Goodman, M. Ibe, A. Rajaraman, W. Shepherd, T. M. P. Tait, and H.-B. Yu, *Constraints on Dark Matter from Colliders*, *Phys. Rev. D* **82** (2010) 116010, [[arXiv:1008.1783](#)].
- [164] CMS, V. Khachatryan et al., *Search for dark matter, extra dimensions, and unparticles in monojet events in proton–proton collisions at $\sqrt{s} = 8$ TeV*, *Eur. Phys. J. C* **75** (2015), no. 5 235, [[arXiv:1408.3583](#)].
- [165] ATLAS, G. Aad et al., *Search for dark matter in events with a hadronically decaying W or Z boson and missing transverse momentum in pp collisions at $\sqrt{s} = 8$ TeV with the ATLAS detector*, *Phys. Rev. Lett.* **112** (2014), no. 4 041802, [[arXiv:1309.4017](#)].
- [166] ATLAS, G. Aad et al., *Search for new phenomena in events with an energetic jet and missing transverse momentum in pp collisions at $\sqrt{s} = 13$ TeV with the ATLAS detector*, [[arXiv:2102.10874](#)].
- [167] CMS, A. M. Sirunyan et al., *Search for new physics in the monophoton final state in proton-proton collisions at $\sqrt{s} = 13$ TeV*, *JHEP* **10** (2017) 073, [[arXiv:1706.03794](#)].
- [168] CMS, A. M. Sirunyan et al., *Search for dark matter produced with an energetic jet or a hadronically decaying W or Z boson at $\sqrt{s} = 13$ TeV*, *JHEP* **07** (2017) 014, [[arXiv:1703.01651](#)].
- [169] A. J. Larkoski, I. Moult, and B. Nachman, *Jet Substructure at the Large Hadron Collider: A Review of Recent Advances in Theory and Machine Learning*, *Phys. Rept.* **841** (2020) 1–63, [[arXiv:1709.04464](#)].
- [170] E. M. Metodiev, B. Nachman, and J. Thaler, *Classification without labels: Learning from mixed samples in high energy physics*, *JHEP* **10** (2017) 174, [[arXiv:1708.02949](#)].
- [171] E. M. Metodiev and J. Thaler, *Jet Topics: Disentangling Quarks and Gluons at Colliders*, *Phys. Rev. Lett.* **120** (2018), no. 24 241602, [[arXiv:1802.00008](#)].
- [172] F. A. Di Bello, S. Ganguly, E. Gross, M. Kado, M. Pitt, L. Santi, and J. Shlomi, *Towards a Computer Vision Particle Flow*, *Eur. Phys. J. C* **81** (2021), no. 2 107, [[arXiv:2003.08863](#)].
- [173] D. Guest, K. Cranmer, and D. Whiteson, *Deep Learning and its Application to LHC Physics*, *Ann. Rev. Nucl. Part. Sci.* **68** (2018) 161–181, [[arXiv:1806.11484](#)].
- [174] A. Radovic, M. Williams, D. Rousseau, M. Kagan, D. Bonacorsi, A. Himmel, A. Aurisano, K. Terao, and T. Wongjirad, *Machine learning at the energy and intensity frontiers of particle physics*, *Nature* **560** (2018), no. 7716 41–48.

- [175] J. Alimena, Y. Iiyama, and J. Kieseler, *Fast convolutional neural networks for identifying long-lived particles in a high-granularity calorimeter*, *JINST* **15** (2020), no. 12 12, [[arXiv:2004.10744](#)].
- [176] Y. Gershtein, S. Knapen, and D. Redigolo, *Probing naturally light singlets with a displaced vertex trigger*, [arXiv:2012.07864](#).
- [177] **CMS**, S. Mukherjee, *Data Scouting and Data Parking with the CMS High level Trigger*, *PoS EPS-HEP2019* (2020) 139.
- [178] **CMS**, D. Anderson, *Data Scouting in CMS*, *PoS ICHEP2016* (2016) 190.
- [179] **ATLAS Collaboration**, *Trigger-object Level Analysis with the ATLAS detector at the Large Hadron Collider: summary and perspectives*, ATL-DAQ-PUB-2017-003, CERN, Geneva, Dec, 2017.
- [180] S. Chang, T. Cohen, and B. Ostdiek, *What is the Machine Learning?*, *Phys. Rev. D* **97** (2018), no. 5 056009, [[arXiv:1709.10106](#)].
- [181] R. Shwartz-Ziv and N. Tishby, *Opening the black box of deep neural networks via information*, 2017.
- [182] T. Faucett, J. Thaler, and D. Whiteson, *Mapping Machine-Learned Physics into a Human-Readable Space*, [arXiv:2010.11998](#).
- [183] **ATLAS Collaboration**, R. E. Owen, *The ATLAS Trigger System*, .
- [184] V. Khachatryan, A. Sirunyan, A. Tumasyan, W. Adam, E. Asilar, T. Bergauer, J. Brandstetter, E. Brondolin, M. Dragicevic, J. Er, and et al., *The cms trigger system*, *Journal of Instrumentation* **12** (Jan, 2017) P01020P01020.
- [185] B. T. Huffman, C. Jackson, and J. Tseng, *Tagging b quarks at extreme energies without tracks*, *J. Phys. G* **43** (2016), no. 8 085001, [[arXiv:1604.05036](#)].
- [186] **Particle Data Group**, P. A. Zyla et al., *Review of Particle Physics*, *PTEP* **2020** (2020), no. 8 083C01.
- [187] E. Witten, *Baryons in the 1/n Expansion*, *Nucl. Phys. B* **160** (1979) 57–115.
- [188] **ATLAS Collaboration** *Phys. Rev. D* **96** (Sep, 2017) 052004.
- [189] **ATLAS**, M. Aaboud et al., *Search for light resonances decaying to boosted quark pairs and produced in association with a photon or a jet in proton-proton collisions at $\sqrt{s} = 13$ TeV with the ATLAS detector*, *Phys. Lett. B* **788** (2019) 316–335, [[arXiv:1801.08769](#)].

- [190] **CMS**, A. M. Sirunyan et al., *Search for Low Mass Vector Resonances Decaying to Quark-Antiquark Pairs in Proton-Proton Collisions at $\sqrt{s} = 13$ TeV*, *Phys. Rev. Lett.* **119** (2017), no. 11 111802, [[arXiv:1705.10532](#)].
- [191] **CMS**, A. M. Sirunyan et al., *Search for dijet resonances in proton-proton collisions at $\sqrt{s} = 13$ TeV and constraints on dark matter and other models*, *Phys. Lett. B* **769** (2017) 520–542, [[arXiv:1611.03568](#)]. [Erratum: *Phys.Lett.B* 772, 882–883 (2017)].
- [192] **ATLAS Collaboration** *Phys. Rev. Lett.* **121** (Aug, 2018) 081801.
- [193] A. Alloul, N. D. Christensen, C. Degrande, C. Duhr, and B. Fuks, *FeynRules 2.0 - A complete toolbox for tree-level phenomenology*, *Comput. Phys. Commun.* **185** (2014) 2250–2300, [[arXiv:1310.1921](#)].
- [194] C. Degrande, C. Duhr, B. Fuks, D. Grellscheid, O. Mattelaer, and T. Reiter, *UFO - The Universal FeynRules Output*, *Comput. Phys. Commun.* **183** (2012) 1201–1214, [[arXiv:1108.2040](#)].
- [195] J. Alwall, R. Frederix, S. Frixione, V. Hirschi, F. Maltoni, O. Mattelaer, H. S. Shao, T. Stelzer, P. Torrielli, and M. Zaro, *The automated computation of tree-level and next-to-leading order differential cross sections, and their matching to parton shower simulations*, *JHEP* **07** (2014) 079, [[arXiv:1405.0301](#)].
- [196] L. Carloni and T. Sjostrand, *Visible Effects of Invisible Hidden Valley Radiation*, *JHEP* **09** (2010) 105, [[arXiv:1006.2911](#)].
- [197] M. Cacciari, G. P. Salam, and G. Soyez, *The anti- k_t jet clustering algorithm*, *JHEP* **04** (2008) 063, [[arXiv:0802.1189](#)].
- [198] M. Cacciari, G. P. Salam, and G. Soyez, *FastJet User Manual*, *Eur. Phys. J.* **C72** (2012) 1896, [[arXiv:1111.6097](#)].
- [199] M. L. Mangano, M. Moretti, F. Piccinini, and M. Treccani, *Matching matrix elements and shower evolution for top-quark production in hadronic collisions*, *JHEP* **01** (2007) 013, [[hep-ph/0611129](#)].
- [200] **ATLAS Collaboration**, V. Izzo, *ATLAS Upgrades*, , CERN, Geneva, Sep, 2020.
- [201] **ATLAS Collaboration**, *Technical Design Report for the Phase-I Upgrade of the ATLAS TDAQ System*, , Sep, 2013. Final version presented to December 2013 LHCC.

- [202] **ATLAS Collaboration**, *Trigger Menu in 2017*, ATL-DAQ-PUB-2018-002, CERN, Geneva, Jun, 2018.
- [203] G. Aad, B. Abbott, D. C. Abbott, A. A. Abud, K. Abeling, D. K. Abhayasinghe, S. H. Abidi, O. S. AbouZeid, N. L. Abraham, and et al., *Performance of electron and photon triggers in atlas during lhc run 2*, *The European Physical Journal C* **80** (Jan, 2020).
- [204] **ATLAS**, M. Aaboud et al., *Measurement of the photon identification efficiencies with the ATLAS detector using LHC Run 2 data collected in 2015 and 2016*, *Eur. Phys. J. C* **79** (2019), no. 3 205, [[arXiv:1810.05087](#)].
- [205] **ATLAS**, M. Aaboud et al., *Performance of top-quark and W-boson tagging with ATLAS in Run 2 of the LHC*, *Eur. Phys. J. C* **79** (2019), no. 5 375, [[arXiv:1808.07858](#)].
- [206] **ATLAS Collaboration**, *Identification of Hadronically-Decaying W Bosons and Top Quarks Using High-Level Features as Input to Boosted Decision Trees and Deep Neural Networks in ATLAS at $\sqrt{s} = 13$ TeV*, , CERN, Geneva, Apr, 2017.
- [207] **ATLAS Collaboration**, *Performance of mass-decorrelated jet substructure observables for hadronic two-body decay tagging in ATLAS*, , CERN, Geneva, Jul, 2018.
- [208] **ATLAS Collaboration**, *Deep generative models for fast shower simulation in ATLAS*, , CERN, Geneva, Jul, 2018.
- [209] V. V. Gligorov and M. Williams, *Efficient, reliable and fast high-level triggering using a bonsai boosted decision tree*, *JINST* **8** (2013) P02013, [[arXiv:1210.6861](#)].
- [210] **ATLAS Collaboration**, *ATLAS detector and physics performance: Technical Design Report, 1*. Technical design report. ATLAS. CERN, Geneva, 1999.
- [211] **ATLAS Collaboration**, M. Capeans, G. Darbo, K. Einsweiler, M. Elsing, T. Flick, M. Garcia-Sciveres, C. Gemme, H. Pernegger, O. Rohne, and R. Vuillermet, *ATLAS Insertable B-Layer Technical Design Report*, CERN-LHCC-2010-013. ATLAS-TDR-19, Sep, 2010.
- [212] A. Hoecker, P. Speckmayer, J. Stelzer, J. Therhaag, E. von Toerne, and H. Voss, *TMVA: Toolkit for Multivariate Data Analysis*, *PoS ACAT* (2007) 040, [[physics/0703039](#)].

- [213] **ATLAS**, G. Aad et al., *Triggers for displaced decays of long-lived neutral particles in the ATLAS detector*, *JINST* **8** (2013) P07015, [[arXiv:1305.2284](#)].
- [214] C. Cesarotti and J. Thaler, *A Robust Measure of Event Isotropy at Colliders*, *JHEP* **08** (2020) 084, [[arXiv:2004.06125](#)].
- [215] M. Hindmarsh, S. J. Huber, K. Rummukainen, and D. J. Weir, *Shape of the acoustic gravitational wave power spectrum from a first order phase transition*, *Phys. Rev.* **D96** (2017), no. 10 103520, [[arXiv:1704.05871](#)].
- [216] J. Ellis, M. Lewicki, and J. M. No, *On the Maximal Strength of a First-Order Electroweak Phase Transition and its Gravitational Wave Signal*, [arXiv:1809.08242](#). [JCAP1904,003(2019)].
- [217] J. Ellis, M. Lewicki, J. M. No, and V. Vaskonen, *Gravitational wave energy budget in strongly supercooled phase transitions*, *Journal of Cosmology and Astroparticle Physics* **2019** (jun, 2019) 024–024.